UNIVERSITÉ DU LUXEMBOURG

PhD-FSTM-2024-108
The Faculty of Science, Technology and Medicine

DISSERTATION

Defense held on 18/12/2024 in Esch-sur-Alzette
to obtain the degree of

DOCTEUR DE L'UNIVERSITÉ DU LUXEMBOURG
EN PHYSIQUE

by

Kilian Huber

Development of a Compact Multiple-Reflection Time-of-Flight Mass Spectrometer for Nano-Analytics and Space Applications

Dissertation defense committee

Dr. Tom Wirtz, Dissertation supervisor
Luxembourg Institute of Science and Technology

Prof. Dr. Alex Redinger, Chairman
Université du Luxembourg

Dr. Hung Quang Hoang
Luxembourg Institute of Science and Technology

Prof. Dr. ir. Pieter Kruit
TU Delft

Prof. Dr. Anjam Khursheed
Politecnico di Milano

Advanced Instrumentation for Nano-Analytics Group
Scientific Instrumentation and Process Technology Unit
Luxembourg Institute of Science and Technology, Belvaux, Luxembourg

Summary

This thesis presents the development of a new compact, high-performance, and flexible-operation multiple-reflection time-of-flight mass spectrometer. The primary application areas are nano-analytics and space exploration. The main components of the developed mass spectrometer are a pulsed electron impact ion source and a multiple-reflection mass analyzer. The design and optimization of these components were supported by computer-aided methods developed as part of this work.

A novel optimization framework for versatile use in optimization applications within the design of charged particle optics components has been developed. It combines a multi-objective optimization algorithm based on genetic algorithms with workflows for design modeling in the simulation environment SIMION. The automated interaction between these modules is facilitated by a dedicated communication interface. These modules enable the simultaneous and independent Pareto optimization of many parameters of different types for two individual objective functions. The optimization and modeling are complemented by methods for post-optimization data analysis, which allow for a gradual reduction of the possible Pareto solution space to ultimately identify the most suitable solution. This includes a sensitivity analysis, which provides insight into the effects of parameter changes on the system output. High-performance designs with robustness against parameter deviations were achieved.

To achieve a compact instrument design with high mass resolving power, a configuration was chosen for the mass analyzer consisting of two identical, rotationally symmetrical ion mirrors, each with seven electrodes, aligned axially against each other. This arrangement allows mutual reflection of the ions, creating a closed path for ion trajectories within the multiple-reflection cell. During operation, the performance in terms of mass resolving power can be flexibly adjusted by controlling the number of full-turns performed. The design of the ion mirrors was initially derived analytically but did not meet the required mass resolving power. Using the developed optimization framework, the mass analyzer's design was significantly improved with respect to the applied potential distributions. Additionally, a new approach for the spatial focusing of the ion beam improved transmission characteristics. The operating

modes of the mass analyzer are: (i) injection, in which particles are introduced into the multiple-reflection cell from the source; (ii) multiple-reflection operation, where particles oscillate back and forth between the ion mirrors and are separated by mass; and (iii) ejection, where particles are ejected from the multiple-reflection cell toward the detector.

The pulsed ion source of the mass spectrometer allows ions to be introduced into the mass analyzer at a defined start time. To achieve this, the design of a continuously emitting electron impact ion source was modified to divide operation into a trapping phase and a pulsed extraction phase. The accumulation of particles during the trapping phase allows measurements with significantly enhanced sensitivity. A new extraction method has been developed that significantly reduces background noise in the spectrum by synchronizing the electron beam for ionization with the ion extraction. This results in measurements with a higher signal-to-noise ratio.

Simulations of the complete mass spectrometer system yielded a mass resolving power of $M/\Delta M$ (full-width at half maximum) greater than 20,000 for m/z at 40 amu/e, with 400 full-turns and a total flight time of 1.5 ms at the detector plane. The clear separation of two closely spaced isotope peaks, ^{18}O at 17.9992 amu/e and H_2O at 18.0106 amu/e, was demonstrated in operation with at least 100 full-turns, highlighting the instrument's suitability for high-precision analyses. The simulation design has been transferred to a prototype, which will undergo experimental testing in a follow-up project. The prototype has a total length of less than 50 cm and weighs 2.5 kg. However, this prototype, intended for proof-of-concept testing, is based on a modified, existing bulky ion source. The eventual use of a miniaturized, custom-designed ion source is intended to achieve a more compact design. The mass analyzer prototype has a total length of 20 cm, an axial drift length of 7.5 cm, a maximum diameter of 5.5 cm, and weighs less than 1 kg. The developed mass spectrometer meets the requirements for compactness and performance necessary for applications in nano-analytics and space exploration.

Contents

1 Introduction

1.1 Compact and high-performance mass spectrometers

Mass spectrometry is a pivotal analytical technique widely utilized for chemical analysis, enabling the assessment of atomic and molecular samples to determine their composition and relative abundance [1]. This capability is crucial for elucidating the structure of various substances and determining isotope compositions, which has broad implications across multiple fields including nano-analytics, space exploration, analytical chemistry, materials science, life sciences, and environmental science, as well as security and forensics applications [2].

The development of a compact yet powerful mass spectrometer is particularly relevant for applications in nano-analytics [3–5] and space [6–9]. In both areas, compact dimensions are essential for the efficient integration of the mass spectrometer, either as an add-on attachment for nano-analytic platforms or as a scientific payload onboard space missions. Despite the compactness of the mass spectrometer, it is crucial that high performance is also provided in order to be able to carry out sophisticated chemical analyses. In nano-analytics as well as in space applications, mass spectrometer instruments with a certain degree of compactness have been applied, however, these instruments show a clear lack in performance to serve the enhanced requirements of recent and upcoming applications in these fields. A novel compact and high-performance mass spectrometer providing enough flexibility in its design and operation could effectively be applied for both use cases.

In the realm of nano-analytics, the integration of mass spectrometers as add-on instruments with advanced microscopy techniques has significantly advanced the field. In secondary ion mass spectrometry (SIMS) [10], ion bombardment of a sample surface by high-energetic primary ions creates secondary ions originating from the sample which are extracted and analyzed by the mass spectrometer to obtain high-sensitivity and high-resolution chemical information. Correlation of this data with the microscopy imaging data ultimately allows to combine morphological, structural and chemical information, which is highly valuable in numerous research domains. In semiconductor research, SIMS allows for precise depth profiling and analysis of doping elements [11]. It is also used to study battery materials [12] by mapping elemental distributions at high spatial resolution, aiding in understanding degradation mechanisms, and in life sciences for visualizing biomolecules within tissues [13], contributing to advances in drug delivery and cellular processes. In this context, highest resolution high-sensitivity chemical imaging is achieved through SIMS when coupling a double-focusing magnetic sector mass spectrometer with focused ion beam (FIB) platforms, such as a helium ion microscope (HIM) [4, 14, 15], Cs^+ Low Temperature Ion Source FIB [16], Liquid Metal Alloy Ion Source (LMAIS) FIB [17] or dual-beam FIB-scanning electron microscope (SEM) [5], achieving sub-10 nm lateral resolution, which highlights the potential of this integration for high-resolution high-sensitivity chemical analysis. Further extending these capabilities, a multimodal instrument [3] facilitating in situ correlative analysis of nanoparticles by combining magnetic sector SIMS with complementary techniques such as FIB microscopy and a scanning transmission ion microscope (STIM), thereby enabling comprehensive characterization at the nanoscale. The magnetic sector mass spectrometers in these setups provide a high mass range $1 - 400$ and a mass resolving power ($M/\Delta M$) above 400. However, these instruments are still relatively heavy and bulky due to the electromagnet, which limits the integrability. Besides magnetic sector analyzers, also time-of-flight (TOF) mass spectrometers, primarily reflectron TOF, are applied in SIMS instrumentation [18]. The secondary ion beam is thereby injected into the mass analyzer in a pulsed way, most commonly by orthogonal extraction [19]. In SIMS, TOF analyzers are especially applied in combination with FIB [20], for which a mass resolving power of 500-4000 was reported for mass 28 amu together with an ion transmission of less than 0.1 % for heavy ions and a weight of the spectrometer of 15 kg [18]. A mass resolving power of 800 was reached with a commercially available orthogonal extraction reflectron TOF [20] with an overall drift length of 0.5 m attached to a FIB-SEM [21]. These examples demonstrate, that higher performance is still needed to reach the level of

conventional SIMS for mass resolving power of several thousand and for sensitvity below 1 ppm [22, 23]. Especially, for life science applications, such as the study of cancer cells, high mass resolving power of several thousand is essential to examine subcellular structures such as mitochondria, the nucleus and the cytoplasm [24–26]. Further, higher compactness is required for more flexible integration in nano-analytic platforms.

In numerous scientific space missions, mass spectrometers have been the primary or secondary instrument payload. Lightweight and compact dimensions are key in this domain, as launch costs heavily depend on the spacecraft mass and size. The application scenarios and their complexity have steadily expanded from the investigation of the Earth's upper atmosphere, through sample analysis in planetary sciences, to investigations in comet missions [6, 27]. A prominent example of mass spectrometers used in space applications includes the two spectrometers from the Cassini-Huygens mission, both based on a quadrupole mass analyzer, the Ion and Neutral Mass Spectrometer (INMS) for studying the upper atmosphere of Saturn's moon Titan [9], and the Gas Chromatograph and Mass Spectrometer (GCMS), which analyzed Titan's lower atmosphere [28]. Additionally, the Rosetta Orbiter Spectrometer for Ion and Neutral Analysis (ROSINA) experiment of the Rosetta mission is noteworthy, as it was used for in-situ analysis of volatile components of the comet 67P/Churyumov-Gerasimenko [8]. This experiment covers the Double Focusing Mass Spectrometer (DFMS), a magnetic sector mass spectrometer with a mass resolving power of 3000, a mass range 15-150 amu/e and a weight of 16.2 kg for a size of $63 \times 63 \times 23$ cm. The Cometary Sampling and Composition (COSAC) instrument [7] onboard of Rosetta's Philae lander, given by a multiturn TOF instrument based on electric sectors, provided very compact dimensions of approximately 40×50 cm in combination with high achievable mass resolving power of 2000 for the full width at half maximum (FWHM). Even smaller dimensions are applied in CubeSatTOF [29], a miniaturized single-reflection TOF mass spectrometer integrated into a one-unit cube sat with 10 cm edge length for analysis of planetary atmospheres, demonstrating a mass resolving power of 176 for mass 4 amu. All applications of mass spectrometry in space have in common, that the instruments must provide highest stability and autonomous and maintenance-free operation. Due to the increasing interest in lunar resource prospecting in both scientific and commercial space missions, new use cases emerge for compact mass spectrometers. Water, which is confirmed to be present on the Moon [30–32], is of special interest, as it is the most important resource for future habitation of the Moon. Utilization of water thereby covers drinking water,

the delivery of breathable oxygen, and hydrogen to be used as rocket fuel [33]. This requires investigations into the geographical distribution of water, the form in which water is present and the types and quantities of volatile substances. Oxygen and hydrogen isotope signatures are a preferred method for exploring key questions about the origin, size and distribution of water resources. In terrestrial studies, stable isotopes of oxygen and hydrogen are frequently utilized to examine phase transitions, the mixing of waters from different ages or sources, and interactions between vapor, liquid, and ice [34]. Similarly, on the Moon, stable isotopes of hydrogen and oxygen can help trace the sources and history of lunar water, offering valuable insights into lunar water resources [35, 36]. Apart from oxygen and hydrogen, isotopic measurements of several other elements (C, N, Ar, P, He, Kr, etc.) are of the highest scientific interest in space exploration, such as in understanding the origin and evolution of the solar system [37], the origin of life on Earth [38], and the search for past and present life [39]. Measuring these isotopic ratios requires a high mass resolving power of several thousand.

The state of the art for applications of compact mass spectrometers in these domains unveils that there is always a trade-off between the dimensions and the weight, and the performance of the instrument. Hence, the main motivation of this thesis is to overcome the current limitations by developing a compact, high performance and flexible mass spectrometer for use in multiple application areas including nano-analytics and space. Three basic types of mass spectrometers are suitable for compact and high-performance instruments, which differ in their function and design, miniaturization and performance characteristics.

Magnetic sector mass spectrometers employ a magnetic field perpendicular to the ion motion vector to separate ions based on their mass-to-charge ratio (m/z) [1]. The Mattauch-Herzog geometry [40], combining a double focusing electrostatic analyzer for energy and directional correction with a magnetic analyzer for ion separation, is commonly used. Double-focusing magnetic sector instruments were considered the state of the art in mass spectrometry, offering unparalleled performance across most analytical parameters, especially mass resolving power and mass accuracy [2]. However, they have now been surpassed in many applications by newer technologies such as Orbitrap and TOF analyzers. Magnetic sector analyzers are typically bulky, heavy, and power-intensive, limiting portability and integrability to the primary instrument [41]. For spectrum acquisition, a scanning mode can be applied using a

single slit and variable magnetic field [42], or parallel acquisition can be employed with multiple slits or a continuous imaging detector [43]. Compact magnetic sector instruments face challenges such as reduced mass range due to the limited lateral dimensions of the detector and lower resolution [44]. Even in recent development for compact design in nano-analytics and in several space missions, magnetic sector instruments still reflect limitations in dimension versus performance.

Orbitrap mass spectrometers apply electrostatic ion trapping around a spindle-shaped electrode, where m/z ratios are determined by measuring ion oscillation frequencies [45]. Ions are injected tangentially into the trap and oscillate both radially around the central electrode and axially along its length. These oscillations induce an image current on the outer electrodes, which is detected and converted into a mass spectrum using a Fourier transform. Its compact design allows for integration into various laboratory settings, making it accessible for diverse applications, particularly in proteomics and metabolomics [46]. A FWHM mass resolving power up to 240 000 at $m/z = 200$ amu/e and mass accuracy within 1 ppm was reported [47]. Applications range from proteomics to small molecule analysis, benefiting from high mass resolving power and mass accuracy. However, limitations exist, including potentially lower scan speeds compared to some TOF instruments [48]. Orbitraps have a finite ion capacity. When analyzing complex mixtures with wide concentration ranges, this can lead to space charge effects, potentially impacting mass accuracy and resolution for very abundant ions [49].

TOF mass spectrometers measure the m/z of ions based on the required flight time to travel a certain path through the analyzer. Different types of TOF spectrometers exist, differing in the achievable performance and the complexity of the setup. Linear TOF instruments [50, 51] involve pulsed ion ejection by the ion source or injection optics and ion flight over a linear course of fixed length until recording at the detector. The flight time of the ions is then given by the temporal difference of the pulsing trigger signal and the ion recording at the detector. Linear setups provide full-spectrum acquisition without the need for scanning and are thus very fast. The mass resolving power for this basic setup is usually given by up to 500 with an ion drift distance below 50 cm [52]. Higher mass resolving power can be obtained with reflectron instruments [53], which apply a single ion mirror to fold and extend the flight path by reflecting the ions. The majority of today's TOF mass spectrometers is based on this type. A mass resolving power of more than 20 000

can be reached with such a configuration [54]. Further enhancement of the mass resolving power is reached with the multiple-reflection time-of-flight (MRTOF) by implementing multiple reflections of the ions with at least two ion mirrors [55]. The mass resolving power thereby becomes dependent on the number of reflections and the total duration of the ion flight. In closed-path configurations, a theoretically unlimited number of ion reflections can be performed, which allowed measurements with mass resolving power exceeding several 100 000 [56]. Recently, even a mass resolving power above 1 000 000 was reported for a MRTOF instrument [57] with a total flight time of 12.5 ms and a length of the mass analyzer of 1 m. Very high performance can thus also be combined with compact dimensions of the device. However, due to the potentially long flight paths in MRTOF, transmission losses caused by particle collisions with other particles or electrodes are inevitable. Furthermore, operating in closed-path configurations with an increasing number of reflections reduces the unambiguous mass range, requiring careful optimization of ion mirrors to minimize aberrational time spread.

Discussing these types of mass spectrometers, magnetic sector analyzers are unsuitable for the intended development of an extremely compact, high-performance mass spectrometer, as a relatively large and heavy magnetic sector is always required and, due to the technology, large compromises must always be made in terms of performance when miniaturizing. Also Orbitrap mass analyzers are not suitable for this purpose. Due to the magnitudes greater free path length of the particles compared to TOF, the vacuum requirements are even stricter [49]. The detection of only very few particles is difficult with Orbitrap, as a certain number of ions must be present to allow detection via the induced current such that sensitivity is limited. The MRTOF principle with closed-path configuration offers great potential for applications in nano-analytics and space, as the mass resolving power and mass range can be set very precisely by adjusting the path time in the mass analyzer. In addition, a very high mass resolving power can be achieved despite the very compact dimensions. This flexibility of design and operation facilitates the adjustment of the instrument for the respective application scenario.

1.2 Optimization in charged particle optics

The field of charged particle optics (CPO) focuses on the behavior of charged particles, such as ions and electrons, in electromagnetic fields and involves the development of sophisticated instruments that enable high-resolution imaging and analysis at the atomic and molecular levels. CPO is fundamental in the design and operation of instruments such as mass spectrometers, FIB instruments, SEM, and transmission electron microscopes (TEM).

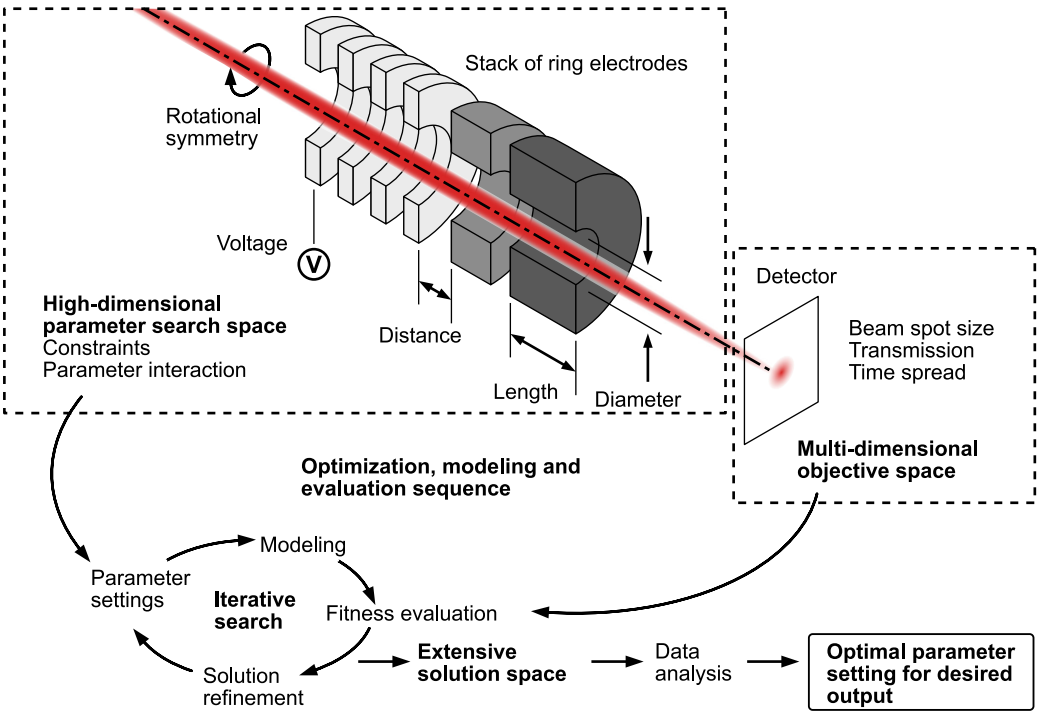

Figure 1.1: The high complexity of CPO systems with many tunable parameters with specific constraints and eventually high interaction and most often multiple output objectives makes analytical parameter search challenging or infeasible. Computational optimization involving iterative parameter search with system modeling and fitness evaluation as well as post-optimization data analysis allows to identify the optimal parameter setting to achieve a certain system output characteristic.

To approach new designs, further enhance the performance and capabilities of CPO instrumentation and ultimately open up new areas of application, it becomes evident that traditional analytical approaches and calculations, which require a high level of expertise, will soon reach their limits. Given the high complexity of modern

instruments, as indicated in Figure 1.1, with numerous cross-dependent parameters of different type and range and the intricate nature of charged particle interactions with electromagnetic fields, advanced computational methods are required to model the system and identify the most suitable parameter values for achieving specific instrument characteristics. In this domain, optimizing for multiple objectives is essential to balance various performance criteria and trade-offs. Computational optimization, involving iterative search routines combined with precise modeling of the underlying physical principles, can therefore achieve high-performance CPO instruments. However, the extensive solution space obtained by the optimization often requires advanced evaluation concepts to finally identify the optimal parameter setting for the desired system output characteristic.

Due to the compactness of the MRTOF mass spectrometer to be developed, the optimal design parameters must be applied in order not to compromise on performance. To address this key requirement, an advanced computer-aided modeling and optimization methodology is required. This should meet the special needs of CPO and significantly support the development process and produce a mass spectrometer that exceeds the capabilities of existing instruments.

Modeling and simulation in CPO is done with a variety of different programs. Several commercially available software packages exist. COMSOL Multiphysics (COMSOL AB, Stockholm, Sweden) [58] is a widely applied finite element method (FEM) multiphysics simulation tool, that provides not only capabilities for electromagnetic field calculation and particle ray tracing, but also offers simulation for other domains. LORENTZ (Integrated Engineering Software, Winnipeg, Canada) [59] is a simulation tool specifically for CPO, applying either the boundary element method (BEM) or FEM. It provides solvers for electrostatic and magnetic fields and handles both two-dimensional (2D) rotational symmetric and three-dimensional (3D) configurations. SIMION (Scientific Instrument Services/ Adaptas Solutions, Palmer, USA) [60], which is applied in this thesis, works with the finite difference method (FDM) and combines the calculation of electric fields and particle tracing. An advanced application programming interface (API) allows high flexibility in simulation design and control. Besides the primarily commercial software, custom CPO modeling programs originating from academia and research institutes such as Electron Optical Design (EOD) [61], Poisson Superfish [62] and Warp [63] exist. These programs are mainly tailored to the needs of the corresponding user group. All of these programs cater to

different aspects of modeling and simulating electromagnetic fields and the behavior of charged particles within them. They vary in their simulation methodologies, accuracy, speed, and flexibility. While some programs are designed for specific applications, others provide a broader range of functionalities. The choice of the appropriate tool depends on the specific requirements of the project, whether it be in terms of precision, computational power, or adaptability.

Computational optimization of CPO-specific challenges was reported for several methods. The most widely used is the Nelder-Mead method, commonly known as downhill-simplex algorithm [64]. SIMION natively provides an integration of this algorithm in its API, making it an accessible entry point for non-linear CPO optimization. The technique has been utilized to concurrently fine-tune several variables, including a set of six distinct electrode potentials [65]. The simplex algorithm excels in rapidly performing local optimization on a small set of parameters for a single objective. However, it is not well-suited for identifying global optima or for handling problems with numerous parameters or multiple independent objectives [66]. A recently introduced method for refining CPO configurations is the adjoint variable technique [67], which stands out for its ability to handle complex systems, as its computational efficiency remains constant even when dealing with numerous parameters. The technique also facilitates the examination of variable interdependencies through sensitivity analysis, though it is limited to optimizing one objective at a time [68].
A powerful and increasingly popular optimization method are genetic algorithms (GAs), which are rooted in evolutionary computing. GAs draw inspiration from evolutionary biology, translating these concepts into computational processes that generate improved solutions to given problems. The primary benefits of GAs include their ability to sustain a high level of diversity within the solution space, which can lead to the identification of global optima. Additionally, they offer the flexibility to adjust numerous input parameters and have the capacity to optimize multiple objectives at the same time [69–71]. These features underscore their suitability for optimization within CPO. GAs have already been explored in various approaches for CPO optimization. For example, a standalone GA was integrated with SIMION for simulation purposes [72]. A method for distributing simulations was proposed, which was used to fine-tune four voltage values with respect to a single output objective. Another study employed a custom GA in combination with SIMION simulation to refine six electrode potentials for a single objective [73]. Additionally, the application of GAs in high-dimensional search spaces was demonstrated in the optimization

of a lens with six electrodes, targeting one objective [74]. This problem involved 23 free parameters, including electrode voltage values and geometric parameters such as longitudinal and radial dimensions of the ring electrodes and the spacing between adjacent electrodes. Custom methodologies were used for field and potential calculations to enhance computational efficiency in this context.
CPO optimization problems often involve multiple conflicting objectives, such as maximizing mass resolving power while increasing particle transmission in a MRTOF mass spectrometer [75]. To address these multiple objectives, the weighted aggregation method is frequently used, which combines several objectives into a single objective by assigning weights based on their relative importance. However, the results are highly sensitive to the predefined weights [76]. Pareto techniques, such as multi-objective genetic algorithms (MOGAs), ultimately deliver a 2D front of Pareto-optimal solutions to the optimization problem, representing a set of optimal trade-off solutions. MOGAs are powerful optimization techniques that extend traditional GAs to solve problems with multiple objectives [77]. In CPO, MOGA was applied for optimizing an electrostatic lens design with two competing objectives [78].

Optimization data evaluation methods are essential to identify the most suitable solution, especially when considering trade-offs. Optimization algorithms, particularly those dealing with high-dimensional parameters and multiple objectives, ultimately produce complicated datasets, which make it challenging to select the most appropriate solution. Additional information is often required to support the selection process, which may include domain-specific knowledge, practical constraints, or secondary optimization criteria [76].

The existing solutions for optimization and modeling in CPO are either limited in terms of their capabilities to handle also complex designs and optimization tasks or in their applicability across many different use cases. Further, there is a clear lack for broadly applicable workflows to evaluate the large amounts of complicated optimization data and to involve higher-level information for the solution selection. Hence, a new computational methodology combining modules for optimization, modeling and data evaluation, tailored to the specific requirements in CPO could advance the development of the MRTOF mass spectrometer as well as other future instruments.

1.3 Scope of this thesis

Mass spectrometers delivering both high compactness and performance are essential to further extend the range of applications, especially in the domains of nano-analytics and space exploration. A novel mass spectrometer fulfilling these requirements as well as offering high flexibility in its operation to be applied for both mentioned application fields has to be developed. The realization of a compact MRTOF mass spectrometer could overcome the limitations of currently existing instruments, which are characterized either by a lack of compactness, performance or both. Further, this technique of mass separation and analysis is promising in terms of fulfilling different performance requirements by flexibly adjusting the mode of operation, which can allow versatile usage of the instrument across different application domains and scenarios. As a technology demonstrator, the to be developed instrument is intended to be the basis for future research and development work, design adjustment and optimization to address more specific applications.

Due to the complexity of such an instrument, purely heuristic approaches are not sufficient. Advanced computer-aided methods for optimization, modeling and data evaluation in the context of CPO instrumentation have to be developed to assist the design of the MRTOF instrument reaching superior performance.

1.3.1 Objectives

The primary objective of this work is the development of a compact, powerful, and flexible MRTOF mass spectrometer for a wide range of applications including nano-analytics and space exploration. This development encompasses the complete lifecycle, including the conceptualization, computer-aided design, manufacturing, and assembly of a prototype. Central to this effort is the design and optimization of the pulsed ion source and the mass analyzer, which are the critical components of the system.

A key aspect of this project is to establish a robust foundation for future advancements in TOF mass spectrometry within the Advanced Instrumentation for Nano-Analytics (AINA) research group. To achieve this, the development process must address several technical challenges, such as enhancing the sensitivity and ion transmission and improving mass resolution. The project also seeks to push the boundaries of miniaturization without compromising the performance, making the device suitable

for a wider range of applications, including utilization as an add-on instrument for nano-analytics and in space applications.

Given the inherent complexity of the system, the project requires the integration of advanced computer-aided methods to support the development process. These methods, which are to be developed as part of the project, include sophisticated modeling techniques, optimization algorithms, and data evaluation tools tailored specifically for CPO instrumentation. These tools must be adaptable to different design tasks, allowing for iterative improvements and modifications.

In addition to the technical objectives, this work also aims to contribute to the broader scientific community by developing tools and methodologies that can be utilized in related fields of research. The outcomes of this project are expected to pave the way for future innovations in mass spectrometry, providing a platform for ongoing research and development within the group and potentially influencing the design of next-generation analytical instruments.

1.3.2 Structure

The theoretical foundations of computer-aided optimization and the instrumentation of TOF mass spectrometer instrumentation are presented in Chapter 2. The development of a new optimization framework for complex design tasks in CPO is described in Chapter 3. The optimization and evaluation process is demonstrated and validated using a test case. Chapter 4 describes the development of a new MRTOF mass spectrometer using simulation and optimization. First, the mass analyzer, the ion source and the injection system are examined individually. This is subsequently complemented by an assessment of the overall system with the interaction of all components. Chapter 5 explains how the developed mass spectrometer was converted into a prototype. The design of the electrical and electronic components, the control software and the transfer of the optical design from the simulation into a computer-aided design (CAD) model of the mechanical components and their assembly are explained. Finally, the results and findings of this work are summarized and discussed in Chapter 6. An outlook on future developments concludes this work.

2 Fundamentals

This chapter introduces the fundamentals and theoretical principles on which the research in this work is based. First, the basic concepts and background related to the instrumentation of TOF mass spectrometers, with a particular focus on MRTOF mass spectrometers, are explained. Additionally, computer-aided methods for the development, modeling, and optimization of instruments within CPO are discussed.

2.1 Time-of-flight mass spectrometer instrumentation

2.1.1 Foundations of mass spectrometry

The fundamental working principle of any mass spectrometer is schematically depicted in Figure 2.1. By measuring the ratio of atomic mass to charge, the components of the sample can be accurately identified [1]. After ionization, the analyte's charged particles are accelerated by an electric field, separated by mass within the analyzer, and then detected.

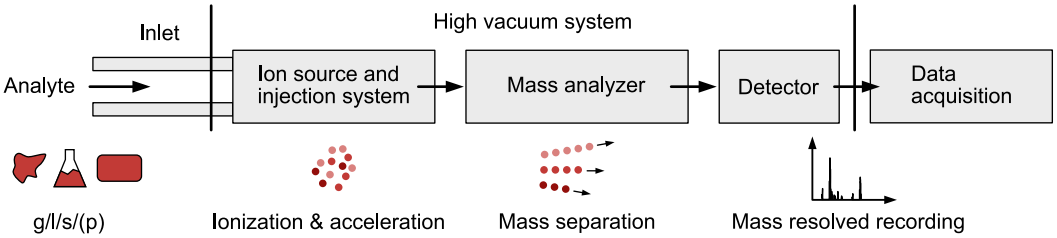

Figure 2.1: Basic setup and function of any mass spectrometer. In principle, analytes of different state of matter (gas/liquid/solid/plasma) can be analyzed, however different sample preparation, insertion and ionization procedures might be required.

Mass spectrum

All types of mass spectrometers have in common, that they ultimately deliver a mass spectrum, which contains all the qualitative and quantitative information about the sample composition, as schematically shown in Figure 2.2. A mass spectrum displays for a certain mass range the detected intensity I for each mass-to-charge (m/z) ratio. The spectrum can then be correlated with known sample spectra from data bases to deliver information about the sample composition.

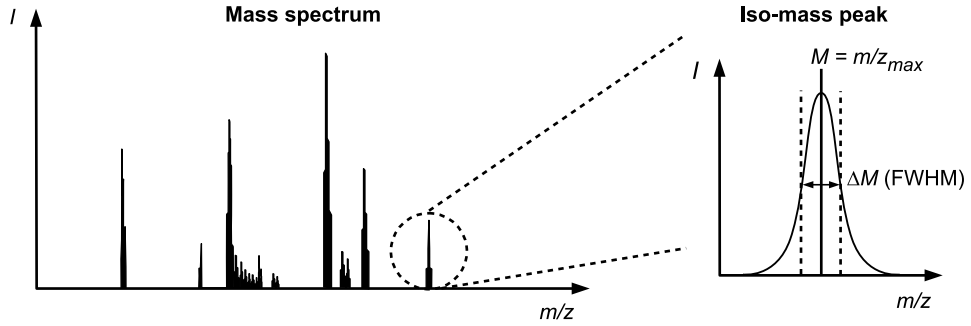

Figure 2.2: Schematic representation of a mass spectrum and an iso-mass peak. In mass spectrometry, the mass resolving power $M/\Delta M$ for the iso-mass peak is commonly derived by the FWHM definition.

Mass resolving power

An important performance metric in mass spectrometry is the mass resolving power, which indicates how well a peak for a given mass m in the mass spectrum can be resolved as an individual signal [79]. The mass resolving power is given by

$$R_{\mathrm{M}} = \frac{M}{\Delta M} \tag{2.1}$$

where $M = m/z$ denotes the ratio of the observed ion mass m and the charge number z, being an integer multiple of the elementary charge. Throughout this thesis, the calculation of R_{M} is based on the observation of a discrete iso-mass peak such that ΔM defines the smallest resolvable peak width. Most commonly, ΔM is given by the FWHM under the assumption of a Gaussian peak profile. However, also the full width for 50 % (FW50) of the contained particles can be applied for the peak width. The definition of mass resolving power should always be indicated with the result.

Sensitivity

The sensitivity of an analytical instrument is given by the ratio of the output response to a change in the sample concentration [1]. In mass spectrometry, the sensitivity for gaseous analytes is defined by the detected current of a certain ion species per available partial pressure of the respective analyte and the unit A/Pa is applied. The sensitivity is influenced by several factors in the instrumentation. On the one hand, the ionization and extraction efficiency contribute to the sensitivity. On the other hand, the transmission in the mass analyzer is decisive [1].

Dynamic range

In mass spectrometry, the dynamic range refers to the range of ion intensities that the detector can accurately measure, from the lowest detectable signal to the point where the detector becomes saturated. A high dynamic range allows the instrument to detect both very low-abundance ions and very high-abundance ions in the same sample.

Mass accuracy

The mass accuracy, also referred to as the mass measurement error, can either be given in absolute values in units of amu by

$$\Delta m = m_i - m_a \tag{2.2}$$

with m_i being the measured single mass and m_a being the actual mass, or as a relative value by

$$\Delta m/m = \frac{m_i - m_a}{m_a} \tag{2.3}$$

in units of ppm [1, 80]. The mass accuracy thus indicates in both cases how strong a measured mass deviates from the expected result.

Mass range

The mass range refers to the range of mass-to-charge ratios that a mass spectrometer can analyze simultaneously within a single measurement and is either given by the absolute range of the lowest and highest contained M ($M_{\text{min}} - M_{\text{max}}$) or the ratio of the two of them ($M_{\text{max}}/M_{\text{min}}$). Scanning-type mass spectrometers such as quadrupole or sequentially measuring magnetic sector instruments provide a low mass range

covering only a single or a narrow set of m/z values within one measurement, while open-path TOF mass spectrometers can acquire the full mass range at once.

Duty cycle

The duty cycle represents the proportion of a given measurement period during which the mass spectrometer records data [1]. Mass spectrometers with scanning operation naturally exhibit a low duty cycle, as only ions within the currently measured narrow mass range are recorded. In contrast, spectrometers capable of analyzing a large or even full mass range achieve higher duty cycles. For TOF mass spectrometers, two distinct duty cycles must be considered. The sampling duty cycle refers to the proportion of time used to introduce the continuously available ions into the mass analyzer. In the commonly used orthogonal extraction TOF method, ions with different m/z ratios traverse the extraction volume at different times. This significantly reduces the sampling duty cycle due to the varying probabilities of ions being extracted during a pulse. For storage ion sources, the sampling duty cycle can ideally reach up to 100 %; however, non-ideal trapping efficiency, limited trapping duration, and extraction efficiency constrain this value. The acquisition duty cycle is determined by the duration of the measurement and the recovery time required between successive measurements. Longer recovery times lead to a lower measurement frequency and, consequently, a lower duty cycle.

2.1.2 Time-of-flight mass spectrometry

The separation and measurement of masses based on the dispersion in time was first proposed in 1946 [50] and demonstrated in practice shortly afterwards [51]. In the simplest case of a linear TOF mass spectrometer, which is shown in Figure 2.3, the charged particles of different m/z are first accelerated to a uniform kinetic energy of a few keV in an electric field. Subsequently, the particles enter a field-free drift tube with this energy, through which they pass unaccelerated. The dependence of the particle drift velocity v_D on m/z causes a temporal separation of the particles within the drift tube. By placing a detector at the end of the drift tube, for a given uniform start time for the particle movement, the m/z can be temporally resolved. Thereby, particles with low mass reach the detector earlier than particles with high mass.

First, magnetic sector and quadrupole mass spectrometers were dominant over TOF mass spectrometry due to their higher sensitivity and mass resolving power [81].

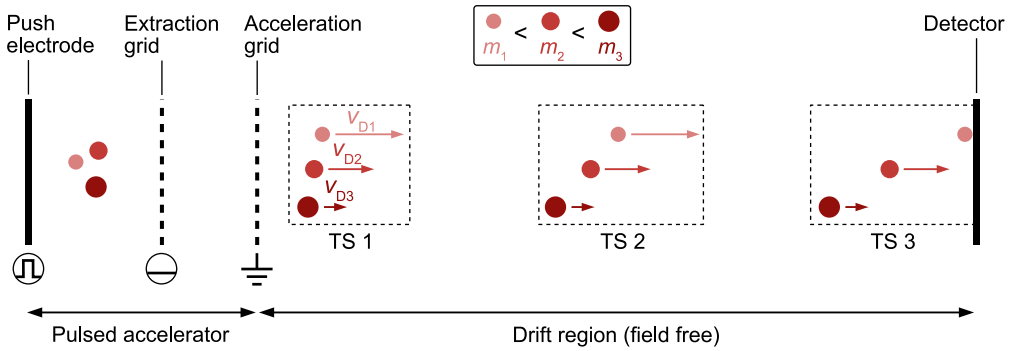

Figure 2.3: The linear TOF represents the simplest setup for a TOF mass spectrometer. Particles of different mass-to-charge ratio are accelerated to a uniform kinetic energy and are temporally separated in a drift tube due to their mass and charge dependent drift velocity v_D as indicated by the increasing spatial distribution of particles for the time steps TS1 to TS3.

With the technological progress in fast electronics and ion detection, as well as with the development of new pulsed beam formation techniques, the concept of TOF was again of special interest and is now dominating the methods of magnetic sector and quadrupole [82]. A huge advantage of TOF mass spectrometers over magnetic sector and quadrupole instruments is the ability to acquire a full mass spectrum in only a few µs with in principle unlimited mass range [52, 83]. The following sections explain the physical background and the concepts, technological approaches and challenges for TOF mass spectrometers.

Basic working principle

In TOF mass spectrometry, the mass separation is based on the dependency of the drift velocity on the mass-to-charge ratio. Thus, for a defined drift distance between the accelerator and the detector, the recorded flight times reflect particles of different mass and charge. When a charged particle of charge q is accelerated in a homogeneous electric field of strength E over a distance Δx, the particle has an initial potential energy of

$$W_{\text{pot}} = E \cdot \Delta x \cdot q = \Delta U \cdot e \cdot z \tag{2.4}$$

where ΔU is the resulting total voltage gradient, e is the elementary charge and z is the integer charge number of the particle. It is thereby assumed that the potential

energy of the particle is completely converted into kinetic energy W_{kin} when passing through the accelerating field, given by

$$W_{\mathrm{pot}} = \Delta U \cdot e \cdot z = W_{\mathrm{kin}} = \frac{1}{2} \cdot m \cdot v_{\mathrm{D}}^2 \tag{2.5}$$

where m denotes the particle mass and v_{D} the particle drift velocity. Since there is no accelerating or decelerating electric field in the drift region, the drift velocity of a particle, given by

$$v_{\mathrm{D}} = \sqrt{\frac{2 \cdot \Delta U \cdot e \cdot z}{m}} \tag{2.6}$$

is constant. Hence, for a drift distance x_{D} between the accelerator and the detector the drift flight time t_{D}, given by

$$t_{\mathrm{D}} = \sqrt{\frac{1}{2 \cdot \Delta U \cdot e} \cdot \frac{m}{z}} \cdot x_{\mathrm{D}} \tag{2.7}$$

is proportional to the square root of the mass-to-charge ratio. This dependence is the basis for any TOF measurement. The total measured flight time t_{measured} aggregates besides t_{D} other time components, such as the ion acceleration time and a delay time t_{delay} for the control lines and signal acquisition. Ultimately [84], this leads to

$$\frac{m}{z} = c \cdot (t_{\mathrm{measured}} - t_{\mathrm{delay}})^2 \tag{2.8}$$

where c represents a calibration constant. The ions are finally recorded at the detector, which delivers a spectrum indicating the recorded intensities over the flight time. This time-resolved spectrum is transferred to the mass spectrum by determination of the calibration constant with a calibrant gas.

The mass resolving power of a TOF mass spectrometer for the FWHM definition is given by

$$R_{\mathrm{M,\ FWHM}} = \frac{M}{\Delta M} = \frac{t_{\mathrm{total}}}{2\Delta t_{\mathrm{total}}} \tag{2.9}$$

with t_{total} being the mean total flight time for an iso-mass peak and $\Delta t_{\mathrm{total}}$ being the FWHM time spread. An increased R_{M} can thus be reached by prolongation of t_{total} of the ion bunch and by decreasing $\Delta t_{\mathrm{total}}$. Ideally, particles of the same m/z have identical TOF, which would produce sharp distinct peaks in the recorded TOF spectrum. However, different effects contribute to the total measured flight time incertitude $\Delta t_{\mathrm{total}}$ in the TOF spectrum. Consequently, this leads to peak

broadening, which limits the achievable mass resolving power. First, different effects of the ion source and the injection optics lead to significant Δt. This involves effects, which directly cause a constant $\Delta t_{\mathrm{source}}$, and effects with indirect impact on the final recorded time spread by creating particles with deviation from the ideal initial properties. Further, any additional optical element causes some aberration-induced Δt by non-ideal optical properties. Finally, some flight time incertitude is introduced by the detector and data acquisition and signal processing.

Primary time focus by the acceleration system

The effects of the ion acceleration and injection optics on the flight time incertitude can be best understood for the simple case of a linear TOF setup with a pulsed single-stage ion accelerator under the assumption of ions of equal m/z as shown in Figure 2.4.

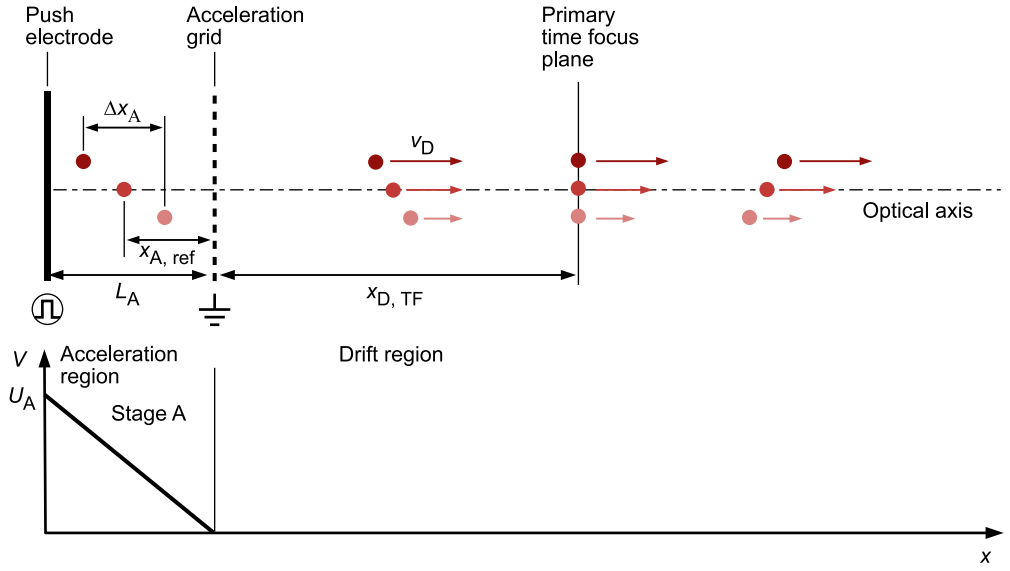

Figure 2.4: Primary time focus created by the pulsed single-stage accelerator. The initial spatial distribution of the ions Δx_{A} leads to a spread of energy and thus drift velocity v_{D}, finally causing some time spread Δt at the detector. The primary time focus plane provides the lowest Δt.

Initially, the created ions are spatially distributed within the acceleration stage. This leads to a distribution of the initial ion starting position Δx_{A} along the optical axis. For simplicity, this explanation assumes that the ions have an initial velocity of zero. When extracting these ions, a pulsed accelerating electric field E_{A} is set by applying a voltage gradient U_{A} between the push electrode and the acceleration grid, separated

by the distance L_A. The initial potential energy of the stationary ions in this electric field is according to Equation 2.4 given by

$$W_\mathrm{pot} = E_\mathrm{A} \cdot x_\mathrm{A} \cdot q = \frac{U_\mathrm{A}}{L_\mathrm{A}} \cdot x_\mathrm{A} \cdot q \tag{2.10}$$

where x_A is the ion's flight path length along the optical axis, measured from its initial starting position to the acceleration grid. The potential energy is thus dependent on the starting position of the ions. As the potential energy is assumed to be fully converted into kinetic energy, the initial spatial distribution introduces a certain energy distribution to the accelerated ions, which finally unfolds in different ion drift velocities, as given by

$$v_\mathrm{D} = \sqrt{\frac{2 \cdot E_\mathrm{A} \cdot x_\mathrm{A} \cdot e \cdot z}{m}} \tag{2.11}$$

Particles with higher x_A will thus end up with higher kinetic energies and shorter flight times to reach a point in the field-free drift region. However, particles with higher x_A also have longer acceleration times in the homogeneous electric field, given by

$$t_\mathrm{A} = \sqrt{\frac{2 \cdot m \cdot x_\mathrm{A}}{q \cdot E_\mathrm{A}}} \tag{2.12}$$

The total time to reach a point in the field-free drift region is thus given by the sum of t_A and t_D. For a certain position in the drift region [85], which is rather a very narrow space, the prolonged $t_{\mathrm{accel,\ A}}$ compensates the low t_D of higher energetic particles, such that

$$\frac{dt}{dx_\mathrm{A}} = \frac{dt_\mathrm{A} + dt_\mathrm{D}}{dx_\mathrm{A}} = \frac{t_\mathrm{A}}{2 \cdot x_\mathrm{A}} - \frac{t_\mathrm{D}}{2 \cdot x_\mathrm{A}} = 0 \tag{2.13}$$

is given. This position is referred to as the primary time focus plane. The total flight time of the particles of equal m/z there becomes independent of the energy, which describes the energy-isochronous condition. For a particle bunch with uniform spatial distribution around a reference particle (ref) with an acceleration length $x_{\mathrm{A,\ ref}}$, the position $x_{\mathrm{D,\ TF}}$ of the primary time focus in the drift region for the single-stage accelerator is given by

$$x_{\mathrm{D,\ TF}} = 2 \cdot x_{\mathrm{A,\ ref}} \tag{2.14}$$

At this position, the first-order aberration coefficient $(T|K)$ equals zero, where T is the ion total flight time difference with the reference $(t - t_{\mathrm{ref}})$ and K is the difference in kinetic energy with the reference ion $(W_{\mathrm{kin}} - W_{\mathrm{kin,\,ref}})$. Positioning of the detector in this plane provides the lowest measured time spread and consequently delivers the highest achievable mass resolving power for energy distributed particles [86]. As it can be seen in Equation 2.14, the position of the first-order time focus with the single-stage accelerator is fixed and solely depends on the initial spatial particle distribution. In practice, this poses a challenge because, for the linear TOF mass analyzer, the achievable optimal drift distance is very short. However, longer drift distances would enable better temporal separation of different m/z values, resulting in higher mass resolving power. To overcome this, Wiley et al. [52] proposed in 1955 the use of a two-stage ion accelerator with different electric field strength in the acceleration stages, as shown in Figure 2.5.

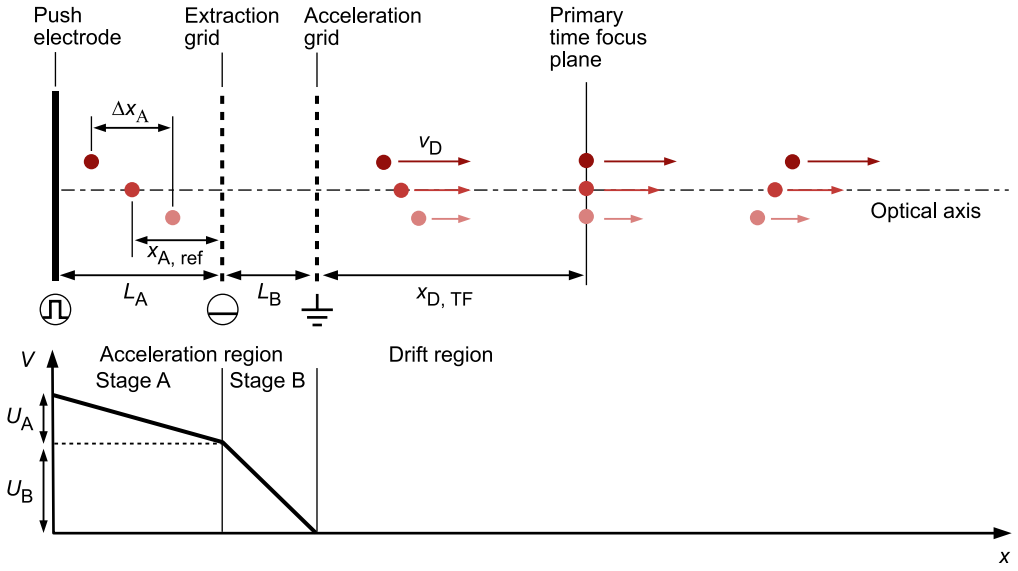

Figure 2.5: Primary time focus created by the pulsed two-stage accelerator. The integration of a second acceleration stage allows to adjust the postion of the primary time focus or to have a higher-order time focus with stronger temporal compression of the ion bunch.

The initially stationary particles are first accelerated in a pulsed electric field E_{A} (stage A) and then in a static electric field E_{B} (stage B) [87]. For a fixed geometry of this setup, another degree of freedom is introduced with U_{B}. This allows to control the position of the first-order time focus. However, increasing $x_{\mathrm{D,\,TF}}$ leads to a weaker temporal compression of the ion cloud [85]. A fixed second-order time-focus

$(T|KK) = 0$ [52, 82, 85] can be reached instead in the case of $W_{\text{kin, 1}}/W_{\text{kin, ref}} < 1/3$ and thus a weak electric field in the first acceleration stage. The second-order time focus provides better temporal compression than the first-order time focus positioned at low $x_{\text{D, TF}}$. In general, higher order focusing allows to compensate the flight time incertitude for a larger range of the input deviation. The position of the second-order time focus [86, 88] is then given by

$$x_{\text{D, TF}} = 2L_{\text{A}} \left(\frac{W_{\text{kin, ref}}}{W_{\text{kin, 1}}} \right)^{(3/2)} - 2L_{\text{B}} \sqrt{\frac{W_{\text{kin, ref}}}{W_{\text{kin, 1}}}} \cdot \frac{1}{1 + \sqrt{W_{\text{kin, 1}}/W_{\text{kin, ref}}}} \tag{2.15}$$

where $W_{\text{kin, 1}}$ is the mean kinetic energy of the particle bunch at the grid separating stage A and stage B and $W_{\text{kin, ref}}$ is the absolute kinetic energy of the reference particle in the field-free drift region.

In reality, the particles always show an initial velocity distribution, mainly given by their thermal movement. Thereby, velocity components along the optical axis represent another origin of flight-time incertitude. Ions originating at the same position but moving into the extraction direction with different velocity will directly cause a time spread. Time-lag focusing [52] was proposed as a compensation method in the two-stage accelerator. Thereby, a time delay is applied between the ion formation and the pulsed extraction, which allows to convert the initial velocity distribution into different starting positions. Particles with higher initial velocity in the extraction direction will thus have lower $x_{\text{accel, A}}$ and subsequently lower energy and drift velocity. However, the main drawback of this approach is, that the propagation of the particles before the extraction is dependent on m/z and thus is only applicable in a certain mass range [83, 85]. Ions moving into the opposite direction of the extraction first have to reverse their velocity vector, which introduces additional flight time referred to as the turn-around time Δt_{TA}. To keep Δt_{TA} low [86], either the initial velocity is effectively reduced by ion cooling, or the extraction field in the ion storage volume is increased. The two-stage ion accelerator, which forms a second-order time focus by a weak electric field in the first stage, is thus more sensitive to initial velocity distributions [85, 89]. A strong extraction field however increases the absolute energy spread, which finally increases the energy-induced flight time error. Hence, linear TOF instruments are limited in their performance and do not allow higher mass resolving power than a few hundred, which is mainly due to the omnipresent spread in ion energy and the distribution of initial ion velocities [83].

Time focusing with ion mirrors

A milestone in TOF mass spectrometry was reached by the invention of the single-reflection TOF. Other than in previous approaches, the flight time incertitude caused by the ion energy spread is compensated outside the source by an ion mirror [83]. This approach was first proposed theoretically in 1957 with a single-stage ion mirror [90]. The idea was further developed and demonstrated experimentally in 1973 for a two-stage ion mirror [53] providing a second-order time-focus. Finally, the so-called reflectron TOF allowed to overcome the limitations in mass resolving power of linear TOF setups. The setup of a two-stage reflectron, is shown in Figure 2.6.

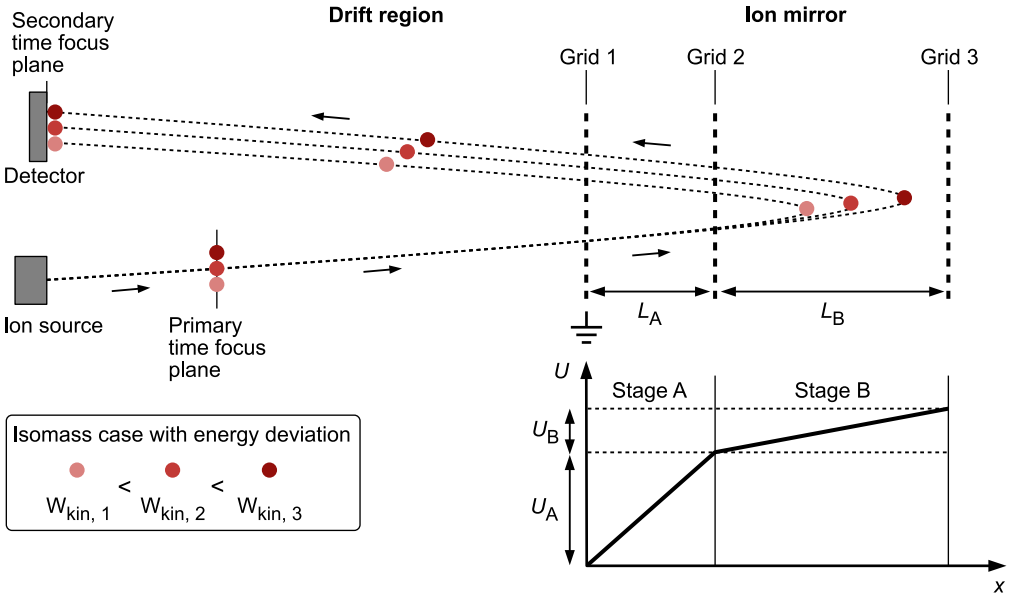

Figure 2.6: Time focusing with a two-stage ion mirror with grids in a reflectron TOF setup. The flight time incertitude due to different ion kinetic energies is compensated by different penetration depths in the mirror field at the secondary time focus plane.

The ion mirror provides two homogeneous electric fields between grids. Ions entering the ion mirror are first decelerated by an electric field until their velocity component in the optical axis becomes zero. The potential $U(x) = a \cdot x$ in the ion mirror with homogeneous field is increasing linearly with the penetration depth x. The electric field then accelerates the ions into the reverse direction until they leave the mirror and enter the field-free drift region, where they will have again the same kinetic energy as before entering the ion mirror. Ions with higher kinetic energy penetrate deeper into the retarding field of the mirror and thus have a longer flight path than particles with

lower kinetic energy. With this, it is possible to create another time-focus with the ion mirror, where the energy-isochronous condition is fulfilled. Hence, the reflectron setup allows to operate the acceleration system with a strong extraction field to reduce Δt_{TA} while the time spread induced by the energy distribution is compensated by the ion mirror at the second time-focus plane. The ion mirror shifts the final time-focus plane and effectively extends the flight path and total flight time, such that the mass resolving power is enhanced by increasing t_{total} and reducing $\Delta t_{\mathrm{total}}$ at the same time.

2.1.3 Multiple-reflection time-of-flight mass spectrometry

The reflectron TOF demonstrates significant performance improvements compared to the linear TOF. However, the mass resolving power is still limited by the achievable total flight time of the ions. The obvious option to extend the total flight time by decreasing the ions kinetic energy is not effective, as this implies also larger relative energy spread [86]. Consequently, the flight path must be extended. The geometrical instrument dimensions as well as the limited focusing capabilities of the ion mirror thereby define the restrictions for reflectron setups. The principle behind the reflectron is to achieve time focusing through an additional aberration-correcting optical element, ensuring the instrument remains energy-isochronous at the detection plane while simultaneously extending the total flight path. By adding another ion mirror, which takes the secondary time focus created by the first ion mirror as the object plane, a tertiary time-focus is reached. This shows that the flight path can be further extended for the energy-isochronous TOF instrument by adding another time-focusing optical element. Hence, MRTOF mass spectrometers utilize this principle by incorporating multiple reflections of ions along their flight path. This folding of the flight path allows the instrument to remain compact and energy-isochronous, even for long total trajectories. A mirror-type MRTOF mass spectrometer was first proposed in 1957 [90].

Types of multiple-reflection time-of-flight mass analyzers

Basically, there exist two different configurations for MRTOF setups, to fold the flight path [91], as shown in Figure 2.7. In the open-path configuration, the ion trajectory shifts spatially with each reflection, whereby an exact trajectory must be defined from the acceleration system to the detector. The number of reflections and the distance that can be travelled is therefore typically fixed.

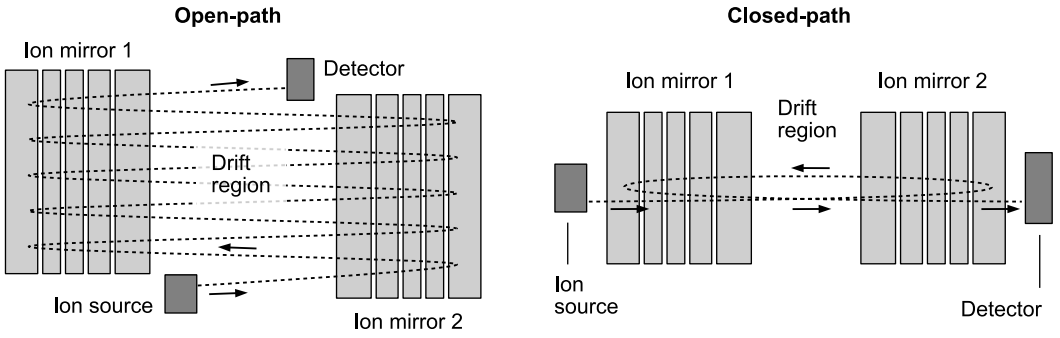

Figure 2.7: Configurations for MRTOF setups involving ion mirrors. In the open-path configuration, the trajectories of the ions are folded in a defined pattern to reach a certain path length. In the closed-path configuration, the ion trajectories are specified for one full-turn such that ions will travel approximately the same course with each performed full-turn in the mass analyzer.

In the closed-path configuration, the ion trajectories are largely identical for each period. A multiple-reflection (MR) cell can therefore be constructed using two opposing ion mirrors. Due to this configuration, any number of reflections and thus very high flight distances can be achieved in principle. Since the mass analyzer here consists of only two ion mirrors, the number of electronic and mechanical components required is also limited and very compact dimensions of the MRTOF mass spectrometer can be achieved. To introduce ions from the acceleration system into the MR cell, the mirror's field must be time-dependently switched to a different potential for a very short duration, allowing the ions to transit through the mirror. The same principle applies when extracting particles from the mass analyzer to the detector. This increases the demands on the electronic components used. However, it enables flexible adjustment of the dwell time and the number of full-turns (N) performed in the mass analyzer, thereby determining the achievable mass resolving power. One can distinguish between cylindrical arrangements, where ion mirrors are formed by stacks of ring electrodes providing rotational symmetry, and planar arrangements, where mirrors are created using parallel electrode plates. Planar ion mirrors are particularly used in open-path configurations. In addition to ion mirrors, magnetic and electrostatic sectors can also be employed to create a folded flight path. Such configurations are referred to as multi-turn TOF mass spectrometers [92, 93]. In these systems, ions with higher energy travel longer distances through the sectors, enabling the realization of energy-isochronous setups. Both, open-path and closed-path configurations are possible, however ion injection and ejection are more complex

in closed-path configurations [87]. Furthermore, strong second-order aberrations in these devices reduce the mass resolving power, and they tend to have relatively large geometric dimension.

Characteristics

The performance characteristics of MRTOF instruments show some specialities, which are further discussed in the following.

The mass resolving power of a MRTOF mass spectrometer depends on the number of full-turns performed by the ions in the mass analyzer, as shown qualitatively in Figure 2.8 (a). The mass resolving power, expressed in terms of the FWHM, is given by

$$R_{\mathrm{M,\ FWHM}} = \frac{t_{\mathrm{total}}}{2\Delta t_{\mathrm{total}}} = \frac{t_{\mathrm{inject}} + N \cdot t_{\mathrm{FT}} + t_{\mathrm{eject}}}{2\sqrt{(\Delta t_{\mathrm{inject}})^2 + (N \cdot \Delta t_{\mathrm{FT}})^2 + (\Delta t_{\mathrm{eject}})^2}} \tag{2.16}$$

where t_{inject} and t_{eject} are the flight times of a reference particle with ideal properties and trajectory along the optical axis of the axially aligned closed-path mass analyzer for injection (acceleration system to center of mass analyzer) and ejection (center of mass analyzer to detector). The reference particle flight time for one full-turn in the mass analyzer is given by t_{FT}. The total time spread consists of several contributions. First, there is a contribution $\Delta t_{\mathrm{inject}}$, which is measured after the injection; a contribution Δt_{FT}, introduced with each full-turn in the mass analyzer due to time-defocusing aberrations of the ion mirrors; and the time spread $\Delta t_{\mathrm{eject}}$, created during the ejection towards the detector. The flight time uncertainty contribution $\Delta t_{\mathrm{inject}}$ arises from the ion source and acceleration system. If the primary time focus is placed at the center of the mass analyzer, this time spread results from aberrational time-defocusing caused by the acceleration system and, primarily, from the differing turn-around times of the ions. As described earlier, this flight time uncertainty is difficult to reduce and constitutes the major contribution to the total flight time error in this setup. However, by increasing the total flight time through a large number of full-turns (N) in the mass analyzer, as indicated by

$$\lim_{N\to\infty} \frac{M}{\Delta M} = \frac{t_{\mathrm{FT}}}{2\Delta t_{\mathrm{FT}}} \tag{2.17}$$

the mass resolving power becomes mainly dependent on the flight time spent for one full-turn and the introduced aberrational time spread for that, while the impact of the initial time spread Δt_0 is reduced [86]. As t_{FT} is defined by the applicable dimensions of the mass analyzer and the ion kinetic energy and thus provides only small room for adjustments, reducing Δt_{FT} is the most effective way to enhance R_{M}. Increasing the order of the time-focus, established after each full-turn, improves the temporal compression of the ion bunch by compensation for the ion energy spread.

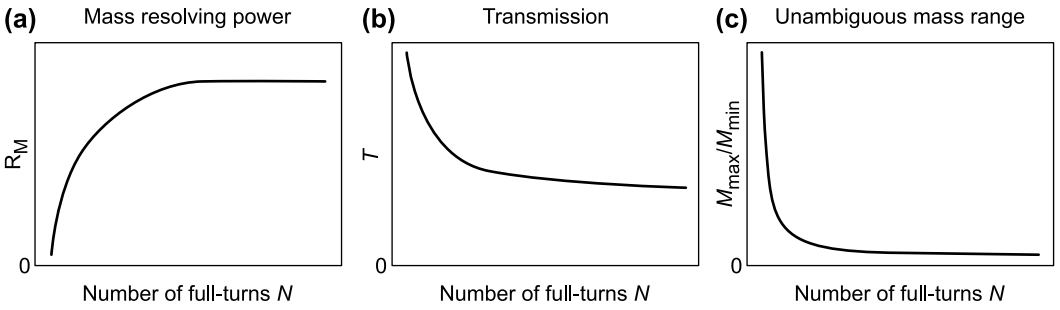

Figure 2.8: Typical curves for the performance characteristics of MRTOF instruments, given by (a) the mass resolving power R_{M}, (b) the particle transmission T and (c) the unambiguous mass range $M_{\mathrm{max}}/M_{\mathrm{min}}$.

High ion transmission through the entire MRTOF instrument must be ensured in order to enable measurements with high sensitivity. In particular, due to the very long distances traveled and the many reflections, even the smallest off-axis and angular trajectory deviations have a significant effect on the achievable total transmission. The typical curve of the total transmission over the number of full-turns performed in a MRTOF setup is shown qualitatively in Figure 2.8 (b). Particles with a strong deviation of their initial trajectory from the optical axis cannot be sufficiently focused and collide with electrodes after only a few reflections and are lost. The transmission behavior typically stabilizes after a few full-turns if particles with a smaller initial trajectory deviation can be spatially focused accordingly. Hence, it is required for any MRTOF mass spectrometer to minimize the initial trajectory deviation, which can be accomplished by carefully designing the ion source, accelerator, and injection system. Additionally, the ion beam must be stabilized within the mass analyzer through spatial focusing, typically achieved by incorporating additional lens elements.

Another performance characteristic applies to closed-path MRTOF configurations. The unambiguous mass range indicates the range of m/z in which the measurement

is unambiguous. If an ion bunch is introduced into the mass analyzer, where M_{min} represents the smallest and M_{max} the largest m/z ratio contained, the difference in the flight paths traveled by ions with M_{min} and M_{max} increases with each full-turn performed. This continues until the additional flight path of the ion with M_{min}, compared to that of the ion with M_{max}, exactly matches the distance required for one full-turn. Since the number of full-turns performed on the race-track cannot be recorded, a time-resolved measurement becomes ambiguous at this point, and the recorded spectrum is inaccurate [87, 94]. This leads to a maximum mass ratio for each number N of full-turns, given by

$$\frac{M_{\mathrm{max}}}{M_{\mathrm{min}}} < \left(\frac{N}{N-1}\right)^2 \tag{2.18}$$

This produces a curve representing the unambiguous mass range, as illustrated qualitatively in Figure 2.8 (c). For a small number of full-turns, the unambiguous mass range is large, but the mass resolving power is low. As the number of full-turns increases, the mass resolving power improves, while both transmission and the unambiguous mass range decrease. Larger dimensions of the mass analyzer, and thus a longer flight path per full-turn, enhance the full-turn-dependent behavior of the mass resolving power, enabling a reasonable resolution with a sufficiently wide mass range even with fewer full-turns. However, this approach is not applicable for compact instrument designs. This highlights the need for careful coordination between the dwell time in the mass analyzer and the required mass resolving power, transmission, and unambiguous mass range. A trade-off between these performance characteristics has to be made.

Gridless ion mirrors

To obtain high-resolution mass spectra, a large number of full-turns and a higher-order time focus by the ion mirrors are in indispensable. In addition, the trajectory of the ions must be kept stable in order to achieve a high transmission for the long flight distance. When using ion mirrors with grids and homogeneous fields, as applied in a reflectron TOF setup, this cannot be achieved, as the grids reduce the transmission by about 10 % each time the ions pass through and additional deviations from the ideal trajectory are induced by scattering at the grid. Further, the focusing capabilities of these mirror designs are quite limited. Especially for many full-turns, the transmission losses are an exclusion criterion for grid-based ion mirrors, such that mirror designs without grids are required. A major challenge in the development of gridless ion

mirrors for MRTOF is that the generated fields are very inhomogeneous and thus the flight time of the ions in the mirror is additionally dependent on their spatial distribution and the motion vectors when entering the mirror field [86]. This long prevented the realization of mirror-based MRTOF instruments. First designs aimed to mimic the grid-based mirrors with purely retarding fields [95]. However these designs had poor spatial focusing properties. A gridless axially-symmetric ion mirror was demonstrated for the use in a single-reflection TOF mass spectrometer by Kutscher et al., in 1991 [96], which provided focusing capabilities in the time and spatial domain by implementing a lens field in front of the decelerating mirror field with conically-shaped ring electrodes. Finally, it turned out, that integrating an accelerating lens field before the decelerating and reflecting field within the ion mirror device [97] has sufficient focusing capability in the spatial domain. This was done by applying a different voltage polarity to the corresponding ring electrodes for the lens and the mirror field. This is, to date, the most commonly applied approach for creating gridless ion mirrors. A MRTOF mass spectrometer based on gridless ion mirrors with an integrated accelerating lens was realized in 2001 [98]. An axially symmetric MRTOF instrument in a closed-path configuration was reported in 2003 [99], which showed a mass resolving power of more than 18000 for 101 full-turns and a final transmission of 40 %. In 2008, Plaß et al. demonstrated a MRTOF mass spectrometer with an ion mirror based on this concept showing a mass resolving power of 600 000 for 49 ms flight time [56].

2.1.4 Formation of pulsed ion bunches

Any TOF mass spectrometer setup requires the pulsed injection of tightly timed ion bunches by the ion source and injection optics. Further, pulsing allows a precisely defined start time for the TOF analysis. However, the mass resolving power of any TOF mass spectrometer is severely impacted by the pulsed injection process. First, the initial time spread Δt_0 of the formed ion bunch at the primary time focus plane represents a bias for the total flight time error $\Delta t_{\mathrm{total}}$ of the analysis. Additionally, the distribution of the particles in terms of energy, off-axis position and angular motion, as set by the ionization and injection process, has a strong influence on the achievable performance of the mass analyzer, not only for the mass resolving power but also for transmission and sensitivity. Thus, the initial particle properties affect each reflection in the ion mirrors. This becomes inherently important in MRTOF experiments with many performed full-turns, while the time spread of the initial ion bunch is the major constraint for linear and reflectron TOF. Hence, the injection method and optics

have to be properly selected and set to minimize these contributions and enhance the overall mass spectrometer performance.

To generate pulsed ion bunches, special instrumentation is required. In principle, ion sources generate continuous ion beams. The basic aim of injection optics is therefore to transmit the particles contained in the ion beam to the mass analyzer only for a very short time window. The main options for generating temporally narrow particle packets [86] are shown in Figure 2.9.

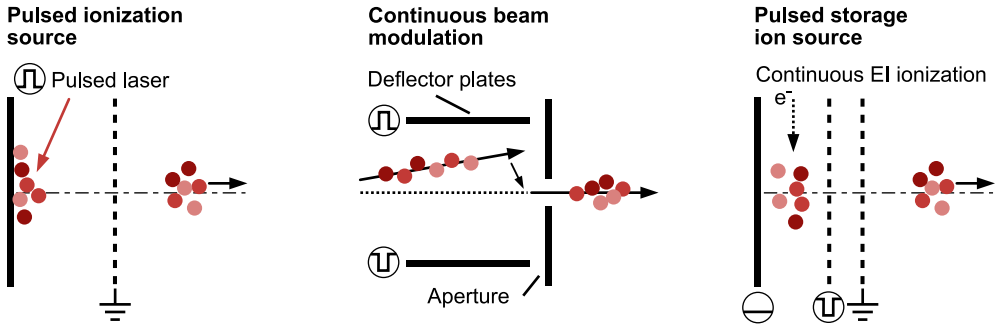

Figure 2.9: Methods for pulsed ion bunch formation. The pulsed ionization source, utilizing mainly laser ionization, creates short ion bunches already by the ionization. The temporal modulation of a continuous ion beam works with most ion sources, while the pulsed storage ion source accumulates ions before pulsing for enhanced sensitivity.

The pulsed ionization source is forming the ion bunches already within the ionization process. This method is limited to certain use cases and can only be applied by a suitable technology for the ion source, as almost all available ion sources only allow continuous ionization. The matrix-assisted laser desorption/ ionization (MALDI) technology [100] should be mentioned here, in which the sample particles are only ionized within a short time window by using a pulsed laser. However, this technique usually yields relatively high particle energy spread, which can be compensated for to a certain extent by combining it with a time-shifted pulsed extraction of the particles, known as delayed extraction.

The temporal modulation of a continuous ion beam can also create short ion bunches. Thereby, in principle almost any ion source technology can be applied delivering continuous ion beams. For the modulation of the beam, different approaches exist. Mechanical shutters [101] can effectively block the ion beam and only allow

it to pass through at the desired time. The particle and beam characteristics are usually not affected. The disadvantage is that mechanical shutter systems such as rotatable apertures only allow relatively large windows for beam transmission and the use of moving parts can limit the range of applications of the spectrometer [86]. A pneumatically actuated mechanical shutter was reported to form ion pulses with a FWHM of 1.5 ms and with a rise and decay time of 1 ms [101], which is magnitudes to high for application in TOF. The continuous ion beam can also be modulated electrically via a dynamically switched deflector [102] or a Bradburry-Nielssen gate. Ion pulses with a length in the range of several ns are thereby possible [103]. However, the ion beam and the particle properties are influenced by the modulation element. Deflectors thus lead to an axial deflection of the injected ion beam. A Bradburry-Nielssen gate typically leads to a strong energy spread of the injected particles [86].

The orthogonal extraction of ions from a continuous narrow ion beam is a special case of modulating a continuous ion beam and represents the most common technique for the formation of pulsed ion bunches [19, 104]. The ion extraction perpendicular to their original direction of movement is usually done by using two pulsed electrodes, which push or pull the particles out of the beam by applying corresponding voltages. This method also allows the utilization of different types of ion sources. The main idea behind the orthogonal extraction is to have a low initial distribution for the particle velocity and position in the extraction axis. Hence, the turnaround time and energy distribution, which are the most prominent contributions to the initial time spread, can be reduced to allow very short ion bunches. Further, the initial velocity distribution can be reduced and the sensitivity can be enhanced by implementing an ion cooling trap [105].

The pulsed storage ion source applies an electron impact (EI) ion source which continuously ionizes particles from a gaseous analyte [106]. The ions are thereby retained and accumulated in the ionization chamber for a certain time by having a relatively flat potential distribution until the extraction pulse is applied. Thereby, similarly to the orthogonal extraction, a push or pull electrode is pulsed to generate an extracting electric field within the ionization and storage chamber. Subsequently, the ions are accelerated by an arrangement of electrodes. This method allows the accumulation of the continuously generated ions to have a high overall ion count and thus improves sensitivity.

2.1.5 Ion detection and signal acquisition

In the instrumental setup of a mass spectrometer, the ions separated by the mass analyzer according to m/z must ultimately be detected and an evaluable digital signal extracted. For particle detection and signal processing in TOF experiments, highest speed and sensitivity are decisive.

Microchannel plate detectors

For these reasons, microchannel plate (MCP) detectors are the method of choice in TOF mass spectrometry. They detect and amplify charged particles, particularly electrons and ions, with high sensitivity and time resolution [107, 108]. As shown in Figure 2.10, a MCP consists of a dense array of microscopic channels with a few µm diameter each, typically made of glass, fused together to form a thin plate. Each channel operates as an independent electron multiplier. When a charged particle strikes the inner wall of a channel, secondary electrons are emitted due to the impact. These secondary electrons are accelerated by an electric field applied across the MCP, causing them to strike the channel walls further down, generating more secondary electrons in a cascading effect. This electron avalanche results in a substantial amplification of the initial signal. Most MCP detectors involve a stack of at least two MCP plates. A chevron arrangement, as indicated in Figure 2.10, includes two plates where the tilted angles show reverse orientation. This allows to further increase the gain, as the electron avalanche exiting the first layer initiates the amplification process in the second layer. Gain levels of up to 10^6 are achievable with such chevron stacks [109], making MCPs extremely sensitive to low-intensity signals. With response times in the ns range, MCPs are suitable for applications requiring high temporal resolution. To finally detect the signal, either a metal anode plate is mounted to the rear of the MCP for fast measurement of the produced electron current or a phosphor screen is placed there instead to spatially resolve the signal. However, prolonged use can lead to degradation of channel surfaces, reducing efficiency and lifespan. MCPs are very sensitive to humidity, as they can absorb water, which leads to cracks and damage of the device. Further, thermal emission of electrons can produce background noise, affecting the signal-to-noise ratio (SNR) in low-signal conditions.

Signal acquisition and fast electronics readout

Finally, the performance of TOF mass spectrometers heavily relies on fast recording technologies, particularly high-speed analog-to-digital converters (ADCs), as ions

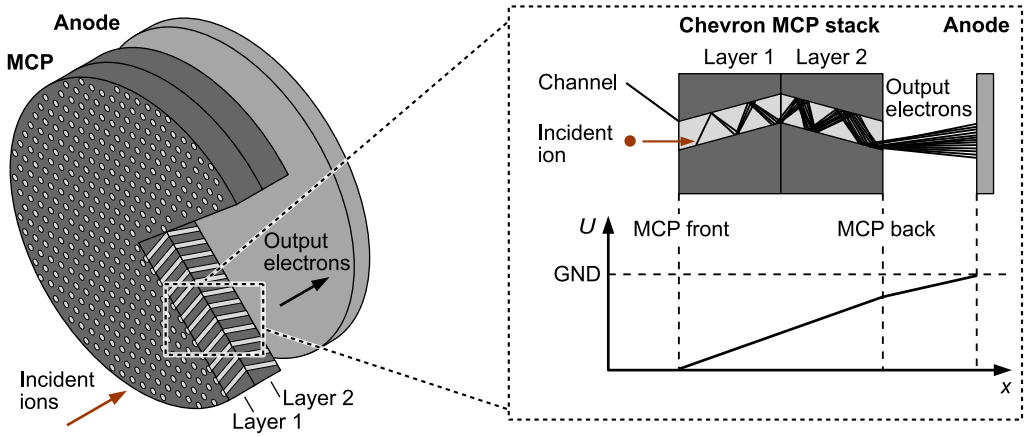

Figure 2.10: Setup and operation principle of a MCP detector with two layers in chevron arrangement. Incident ions cause emission of secondary electrons in the small channels, which again generate even more electrons with each collision with the channel walls. This ultimately creates an output electron current with high gain towards the anode plate. A voltage gradient is applied across the MCP and to the anode to accelerate the secondary electrons.

of the same m/z hit the detector within extremely short time windows [1]. With the technological progress of fast electronics, today's ADCs systems are superior to time-to-digital converters (TDCs). ADCs can detect multiple events simultaneously, acquire an entire pulse waveform including the peak shape and amplitude and allow very long acquisition times, while the more cost-effective TDCs provide only timing information without the acquisition of pulse width and amplitude [110]. To convert with an ADC the ion signal to a digital signal with accurate peak shape, the speed and sampling rate of the ADC, commonly in the range of 1 up to 10 GS/s, is decisive. A high resolution of the ADC is essential to cover a broad ion signal intensity range. Modern ADCs feature more than 8-bit resolution.

2.2 Optimization and charged particle optics simulation

2.2.1 Computational optimization

Computer-aided methods and algorithms for optimizing systems and parameters have found their way into numerous fields, from mathematics and computer science to engineering, finance, architecture and art. In particular, the high complexity of optimization problems often does not allow for an analytical or numerical solution. Optimization is a search process for identifying the solutions to a given problem that best solve it according to given criteria. In the case of a mathematical function, optimization can therefore represent the search for the function values for a local or global extremum. Optimization algorithms can be categorized into several broad approaches, each suited to different types of problems and requirements.

Gradient-based methods are a class of optimization algorithms that utilize the gradients (derivatives) of the objective function to iteratively search for the optimal parameters. Thereby, the calculation of the gradient at a given point gives information in which direction the objective function increases or decreases. Parameters are then updated correspondingly to minimize or maximize the objective function. Techniques such as gradient descent, Newton's method, and quasi-Newton methods like the Broyden–Fletcher–Goldfarb–Shanno (BFGS) algorithm fall into this category [111]. These methods are particularly efficient for smooth, differentiable functions, however, they can become trapped in local optima, limiting their effectiveness in more complex optimization scenarios.

Direct search methods do not rely on derivatives and instead use only the values of the objective function itself. The simplex method and the Nelder-Mead algorithm are notable examples of this approach. The simplex algorithm [112], is widely used for linear programming problems. The algorithm moves from one possible solution to another along the boundaries of the feasible region until the optimal solution is reached. The Nelder-Mead method [64], also known as the downhill simplex method, is particularly effective for multidimensional unconstrained optimization, deforming a simplex in the parameter space to find the minimum. These direct search methods are more robust to noise and discontinuities in the objective function, making them suitable for a wider range of problems, although they may be less efficient than gradient-based methods in certain scenarios.

Stochastic methods and population-based approaches incorporate randomness into the optimization process to help escape local optima. Techniques such as simulated annealing [113] allow for the acceptance of worse solutions with a certain

probability, thereby facilitating exploration of the solution space. Evolutionary computing encompasses a variety of algorithms inspired by the principles of natural evolution, including GAs, and particle swarm optimization. Evolutionary computing approaches iteratively improve a population of candidate solutions using operators like selection, crossover and mutation, which mimic the principles of biological evolution [114]. These stochastic approaches are adept at finding global optima but can be computationally intensive, especially for complex problems [111].

Surrogate-based methods are employed when the evaluation of the objective function is computationally expensive [115]. In these cases, surrogate models approximate the objective function, allowing the optimization to be performed on the less costly surrogate. Techniques such as Kriging and radial basis functions are commonly used for surrogate modeling. The choice of the optimization method is based on several aspects, such as the size and complexity of the problem, the presence of constraints, the differentiability of the objective function, and the available computational resources. Often, a hybrid approach is adopted, where a global stochastic search identifies a promising region, followed by local refinement using gradient-based methods to achieve optimal solutions.

2.2.2 Genetic algorithms

GAs are a population-based optimization technique inspired by the evolutionary principles of natural selection and genetics [69]. The fundamental working principle of GAs is drawn in Figure 2.11. For each iteration of the evolutionary loop of the search routine, referred to as generation, first a population is set which comprises the candidate solutions to the optimization problem. The population is made up of several individuals, each given by a full set of parameter values, which describe the system and are subject to refinement throughout the optimization. Each tunable parameter is referred to as a gene. In CPO, the genes can for instance be given by real-value electrode voltages or geometrical parameters such as electrode length or the distance between them [116]. The variable information to describe the system is thus given by the individuals and each of them represents a possible solution of the optimization problem. Throughout the optimization process, the population with the individuals and their genes are varied to create new solution candidates by refining already well performing individuals. With this, a gradual approach to the best parameter configuration is possible [114].

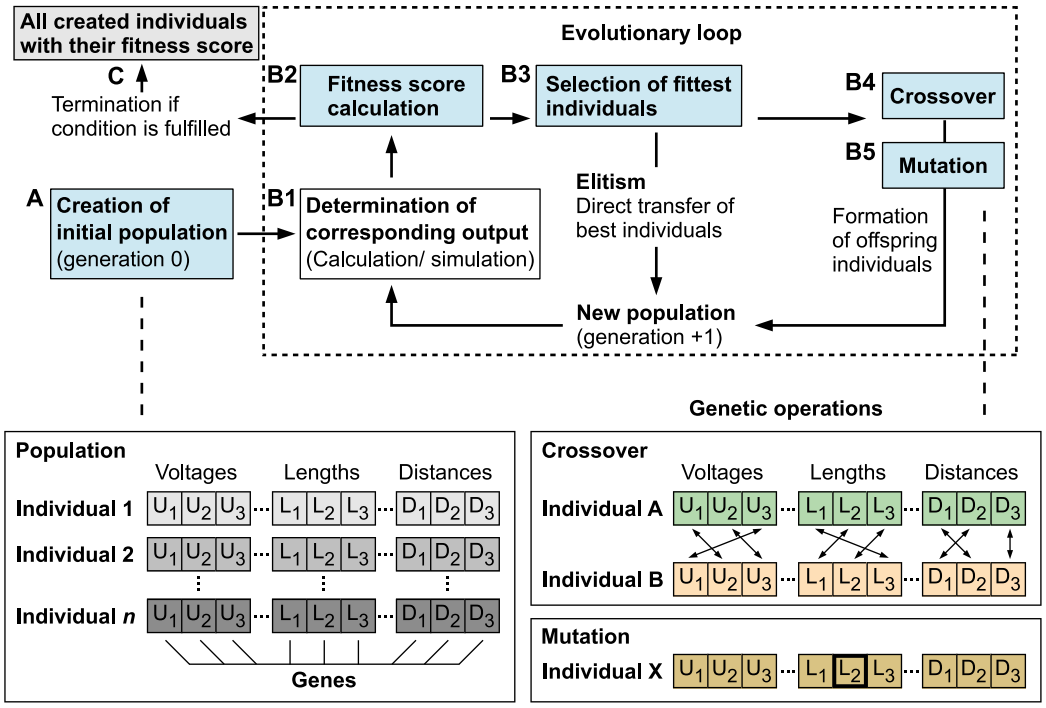

Figure 2.11: Fundamental working principle of GA optimization as an iterative search routine. Canditate solutions, comprised as individuals in the population of each generation, are subject of constant refinement in the course of the optimization by applying genetic operations, inspired by evolutionary processes.

Population creation and output determination

Each iteration of the optimization is initiated by the creation of the population. For the very first iteration (generation 0), an initial population is set up (step A) by randomly creating individuals and genes within predefined boundaries. The population size, meaning the number of contained individuals, is thereby an important setting for the optimization, as it influences the diversity of the solution space and impacts the probability for finding the global optimum. Higher population sizes usually yield in higher diversity, however, the computational effort is also increased. Once the population is defined, the corresponding output of each individual has to be determined (step B1). This can be done by different means, either by calculating a mathematical model with the given parameters or by modeling the system in a simulation, which is the method of choice in CPO [72, 116]. Even the acquisition of output data from a hardware experiment is possible, as GAs provide a certain resistance to output noise.

Fitness score calculation

This output data is typically opaque and needs to be interpreted by the optimization algorithm in order to rate the performance of the individual with respect to the optimization problem. In GAs, this is referred to as fitness score calculation (step B2). The fitness function thereby serves as the mechanism to evaluate the quality of potential solutions in the problem space by delivering a distinct score, which indicates how well the individual fulfills the optimization criterion. It is inherently case-specific, designed to accurately represent the optimization problem at hand and guide the evolutionary process towards optimal solutions [117]. Fitness functions often incorporate penalty strategies to handle constraints, penalizing solutions that violate problem-specific restrictions [114]. Normalization techniques are frequently employed to scale fitness values, ensuring fair comparisons between solutions and preventing premature convergence [118]. The efficiency of the fitness function is paramount, as it is called repeatedly during the algorithm's execution. In complex scenarios, approximation methods may be used to balance computational cost with evaluation accuracy [114]. Multi-objective problems may require specialized fitness functions that can adequately capture and balance multiple, often conflicting, optimization goals [118]. The design of an effective fitness function is critical to the success of GAs, as it directly influences the selection pressure and, consequently, the algorithm's ability to explore the solution space [117].

Genetic operations

Once, the fitness scores are assigned to all individuals of the current generation, the actual genetic operations are applied to finally create the population of the next generation with ideally better fitness scores than the previous generations [119].
For this, first the individuals with the best fitness scores are selected (step B3), which are then subject to further refinement, while individuals with poor fitness are sorted out. For the selection process, several different approaches exist [120]. In Roulette wheel selection individuals are selected with a probability proportional to their fitness. Tournament selection choses for a given number of tournaments randomly a number of solutions and the individual with the best fitness in each tournament is selected. In rank selection, individuals are first ranked based on fitness, and then selected with probability based on their rank. This prevents premature convergence by focusing on relative fitness rather than absolute values. Elitist approaches, such

as in non-dominated sorting genetic algorithms II (NSGA-II) [121] preserve the best individuals from one generation to the next, ensuring they are not lost due to genetic operations like crossover and mutation. Elitism can be combined with other selection methods to accelerate convergence while maintaining diversity.
After the selection of suitable individuals, these are modified to shape the population of the next generation. For this, first the crossover is applied (step B4), where the genes of two parent solutions are combined to form new offspring. Various methods exist to do so [119, 122]. The single-point crossover defines a crossover point in the chain of genes. All genes at the right side of this point are swapped gene-wise between the parents to form two new individuals as offspring. This method does not involve interaction between genes of different index. The n-point crossover is a more general implementation, where the chain of genes is divided into more segments. The simulated binary bounded crossover [123] is an operator specifically designed for real-valued individuals with floating-point values, which simulates the behavior of single-point crossover utilized for binary-coded genes while still ensuring that the offspring remains within specified bounds.
After performing the crossover, the mutation operator is applied (step B5) to maintain the diversity in the solution space and to prevent premature convergence. With a certain probability, randomness is thereby added to the genes of an individual. For real-coded GAs, the polynomial-bounded mutation [121] is commonly applied, which introduces small perturbations to the genes. The mutation is polynomially distributed, meaning that it applies smaller changes with higher probability and larger changes with lower probability, following a specific polynomial distribution.

After these genetic operations, the population of the next generation is formed by combining the new offspring with the elitist individuals and the evolutionary loop starts again. This cycle is repeated until a certain termination condition is fulfilled. This condition can be given by a certain fitness score or maximum number of performed iterations. Finally, the optimization algorithm returns all the individuals created across the generations of the search together with their assigned fitness scores (step C) and the best individual has to be selected.

Multiple-objective optimization with genetic algorithms

GAs allow the optimization of multiple objectives in addition to the possibility of tuning many parameters. For this purpose, a special implementation of GA optimization, MOGA [70], is used, to handle several even competing objectives. Multiple

objective optimization and MOGA generally assume two independent objectives, while the term many objectives optimization is usually used for even more. MOGA is a Pareto technique, which considers for each of the objectives its own fitness metric. A Pareto approach allows to perform the optimization independently for each of the objectives, while non-Pareto techniques such as the weighted aggregation method have a predefined weight for each objective. In MOGA it is thus possible to simultaneously optimize for both objectives and select the best solution afterwards. The outcome of the optimization is then given by a so-called Pareto diagram, as shown in Figure 2.12 (a).

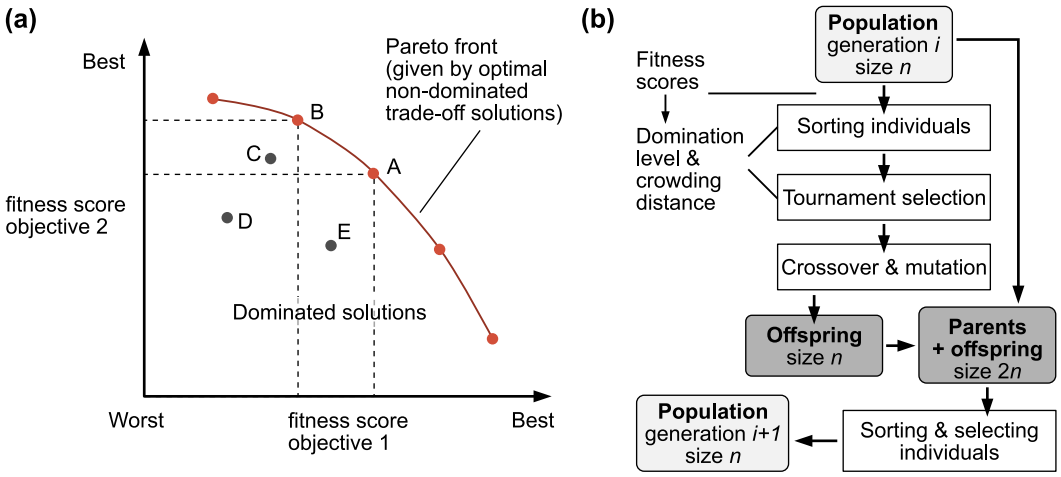

Figure 2.12: (a) Pareto diagram showing the fitness scores for both objectives. The Pareto front comprises the non-dominated individuals and represents an optimal trade-off region. (b) The NSGA-II allows a Pareto technique for the multiple-objective optimization in GAs.

Each individual is thereby assigned with two fitness scores. Individuals showing superior fitness for both objectives are referred to as dominant or non-dominated. For instance, in Figure 2.12 (b) the individual A is non-dominated while individuals D and E are dominated by individual A, and individuals C and D are dominated by individual B. However, there is a set of individuals, such as individuals A and B, which are not dominated by any other individuals. In the Pareto diagram, these manifest as the so-called Pareto front. Individuals along this front are referred to as the Pareto-optimal trade-off solutions, as when moving along this front, improvement of the fitness for one objective always leads to decline of the other objective fitness [76].

The implementation of this concept in GAs first of all foresees to have a fitness function delivering two fitness scores. Further, these multiple fitness scores per individual must be addressed in the genetic operations. NSGA-II [121], as shown in Figure 2.12 (b), is a modification of the conventional single-objective GA, which integrates an elitist approach and modified selection of individuals to address multiple-objective Pareto optimization. After the fitness calculation, all the parent individuals of the population of size n are sorted based on their non-domination level and their crowding distance. Subsequently, a tournament selection is applied, which considers the domination rank or alternatively the crowding distance [76, 121]. The crossover and mutation, which are not affected by the NSGA-II, deliver n offspring individuals. Finally, the offspring and the parent individuals are merged to form a population with $2n$ individuals. All individuals in this merged population are again sorted based on their domination and crowding distance and best half is finally selected to form the population of size n of the next generation. With this, multiple objectives can be handled in the GA optimization. For all Pareto-based optimization, the decision of the most-suitable solution requires a manual trade-off based on higher-level information.

2.2.3 SIMION simulation platform

In the thesis, the FDM simulation platform SIMION (Scientific Instrument Services/ Adaptas Solutions, Palmer, USA) [60, 124] was used in version 8.2.0.11 for CPO design and simulation. SIMION is a broadly applied simulation tool, dedicated for CPO and primarily aims for the calculation of electrostatic fields and the raytracing of charged particles in these fields.

Finite difference method

FDM is a numerical technique that approximates differential equations by discretizing the spatial domain into a grid and replacing continuous derivatives with finite differences. In SIMION, FDM is applied to solve the Laplace equation to determine electrostatic potentials. Thereby, the division of the simulation space into a mesh is done by using central difference schemes to approximate second-order derivatives, leading to a set of linear equations that can be solved iteratively [125]. The accuracy is thereby dependent on the grid resolution, such that a finer simulation mesh is beneficial for the precision. However, this implies also an increase in the computational effort. In CPO, the accuracy of FDM can be reasonable, however FEM and BEM provide higher flexibility for complex geometries and boundary conditions. FDM

is thus a good option for simpler geometries, providing reasonable computational efficiency and accuracy [125].

Field calculation and particle ray tracing

In SIMION, simulations are conducted within an ion optics workbench (IOB), that contains one or more potential arrays (PAs). Using multiple PAs is advantageous for modeling a complex system, as it allows the system to be divided into separate subsystems with less required computational power. Each PA has its own simulation mesh, with an independently defined grid size. The electrostatic field calculation in SIMION is referred to as refining, whereby the required calculation time depends on factors such as the grid size, the PA dimensions, the geometry type and symmetry of the to be simulated optical system, the number of electrodes, and the convergence objective voltage for the electrodes. Highest simulation speed is achieved with rotationally symmetric systems. Three-dimensional systems with planar symmetry or even no applicable symmetry however are computationally much more demanding. Further, increasing the simulation mesh density and the PA dimensions, as well as the number of electrodes, or lowering the convergence objective voltage further extends the field calculation time. The simulation of a modified system usually requires a recalculation of the electrostatic fields before the particle ray tracing. However, SIMION provides fast-adjustable PAs, which allow to modify the electrode voltages without the need for a complete recalculation of the Laplace equation and allows to model time-dependent voltages. Modifications of geometrical parameters instead always necessitate a full refine-process.

In addition to the calculation of electrostatic fields, SIMION also allows particle ray tracing. Particles can be generated with the desired parameters and within freely definable distributions and fly through these fields either individually in a sequential order or in groups. The sequential particle flight is significantly faster than the grouped flight, but the latter allows charge-repulsion effects between the particles to be taken into account. The capabilities of SIMION extend beyond modeling electrostatic fields to include the simulation of particle behavior within vector magnetic fields. SIMION itself does not possess the functionality to calculate magnetic fields internally. Instead, users must rely on external programs to generate the necessary magnetic field data. This data is then imported into SIMION, allowing for comprehensive simulations that incorporate both electrostatic and magnetic field effects [43]. This approach, while requiring additional steps, enables SIMION to offer a more complete particle

trajectory analysis in complex electromagnetic environments.
The precision of SIMION simulations is primarily determined by the simulation grid size and the tracing precision, which is governed by the trajectory quality factor. Smaller grid sizes are preferred for achieving lower error rates in the results, however, they significantly increase the time required for both field calculations and particle flight simulations. Consequently, a trade-off must be made for each simulation to balance accuracy and computational efficiency. The trajectory quality factor in SIMION specifically controls the time step size, dictating how far a particle can move in grid units during each time step. While smaller time steps enhance the accuracy of the results, they also extend the overall simulation time. It is important to note that the effects of modifying the grid size tend to dominate the accuracy of the simulation. Therefore, before initiating any SIMION simulation experiment, it is essential to carefully evaluate the trade-off between computation time and result accuracy to achieve optimal outcomes.

Parameter definition and simulation control

SIMION offers different ways to define the to be simulated system in terms of geometry, applied voltages, particle properties as well as the control and logic of the simulation process and the data recording. A schematic overview of the applied approaches within this thesis is shown in Figure 2.13.
There is the option to set all parameters and control the simulation with the GUI. This option provides only very limited possibilities to meet the user-specific need for the simulation, however for very simple and quick simulation tasks, the interaction with the GUI is a valid option. Besides that, the SIMION GUI allows to display the simulated geometry in 2D and 3D representation, as well as the simulation grid, the potential distribution and the particle trajectories. The main strength of SIMION is the provision of an API to control the simulation in a programmatic way with custom Lua scripts, referred to as user programs. A user program specifies the simulation-specific logic and the actions to be performed. Examples of tasks handled by the user program include assigning electrode voltages and time-dependent voltage switching, monitoring variables, recording and exporting data, and performing automated calculations. This functionality is particularly valuable for complex simulations, as it extends the software's capabilities and facilitates interaction with other scripts or modules and export of data to specific files. A commonly used type of data file are CSV files. There also exist advanced methods for the definition of the system and the simulation parameters. For the definition of the geometry together with the applied

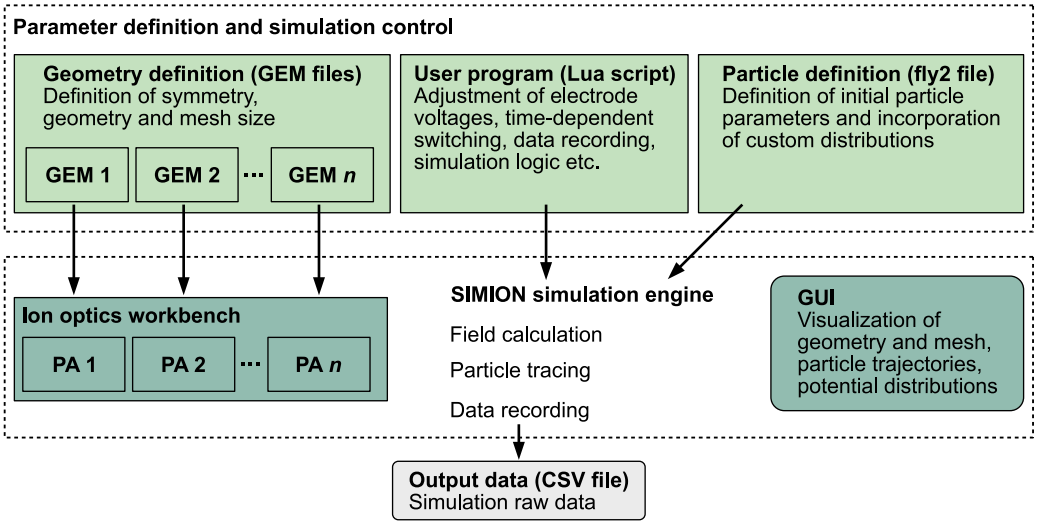

Figure 2.13: Overview of the simulation platform SIMION. The geometry, the symmetry and the simulation mesh size are defined for each PA by a geometry (GEM) file. User programs allow programmatic simulation control. Particle parameters and distributions are set by a fly2 file. With this, the CPO simulation can be performed by the SIMION simulation engine by first calculating the electrostatic fields for each PA in the IOB and performing particle ray tracing and data recording. The simulation outcome is visualized in the graphical user interface (GUI). Simulation raw data is usually exported to comma-separated values (CSV) files.

symmetry and the simulation mesh size, different options are provided. Users can import and convert CAD models as stereolithography (STL) files, providing a way to incorporate complex, pre-designed structures. For simpler geometries, the GUI includes a basic drawing functionality, allowing users to create shapes directly within the program. Additionally, geometries can be defined through text files referred to as GEM files. This method is particularly powerful as it enables programmatic definition and modification of geometries, offering greater flexibility and precision for advanced usage. The GEM file approach is especially useful for creating parametric designs and was thus used in this thesis. The particle properties are specified in another dedicated text file, the so-called fly2 file, which allows users to define particle parameters such as position, velocity, mass, and charge at the start of a simulation. One of the key features of fly2 files is their ability to incorporate custom distributions and sequences, which can be defined using Lua code. This enables precise control over particle properties and allows for complex, non-linear distributions.

3 Optimization Framework for Charged Particle Optics

High-performance ion optical instruments are characterized by a high degree of complexity in their structure and functionality. To further advance the development of these devices and achieve new optimized designs, advanced computational optimization techniques and evaluation methods are essential. This chapter describes a novel optimization framework for charged particle optics, referred to as CPOpt, which can be flexibly applied to a variety of optimization scenarios. Furthermore, this optimization framework is validated by a test case and post-optimization data evaluation procedures are presented.

3.1 Requirements and approach

The state of the art of optimization tools in CPO highlights gaps in optimization methods, with many existing studies offering either limited optimization options or methods that are highly tailored to specific use cases. Notably, there is a certain demand to address the distinct demands of CPO optimization, which involves multiple-objective optimization, optimization across numerous parameters, and the simultaneous yet independent optimization of diverse groups and parameter types. Furthermore, a comprehensive tool that integrates effectively with SIMION, or other simulation platforms, is still lacking. Since SIMION is widely used, integrating advanced optimization features into current simulation processes could significantly improve the results of current CPO development efforts. The large and complicated data produced in multiple-objective optimization is challenging to be accessed and interpreted, emphasizing the demand for a standardized and efficient analysis

process [126]. Most of the methods fall short in providing the higher-level insights required to identify the best solutions among the many possible outcomes.

To bridge these existing gaps, a modular architecture for a comprehensive optimization framework was developed [116]. The core of this framework leverages MOGAs, utilizing the open-source Python library DEAP [127], and establishes an automated interface with the CPO simulation tool SIMION through the messaging library ZeroMQ [128]. The MOGA implementation is based on the NSGA-II, which optimizes multiple parameters and objectives [121]. NSGA-II is particularly effective in producing diverse solutions with strong convergence towards the true Pareto-optimal front. The analysis phase of this optimization process includes a thorough examination of the fitness values and the automated identification of representative clusters of solutions. Visualization techniques, such as parallel coordinate plots, are employed to explore the relationships between system parameters and resulting fitness values across multiple objectives and parameters [126]. A more detailed examination of physical performance further narrows the solution space. Additionally, a subsequent global sensitivity analysis, utilizing dedicated sampling techniques, elucidates the impact of parameter variations and interactions on system outputs [129]. The ultimate objective is to identify parameter configurations that exhibit both high performance and robustness.

3.2 Concept

Based on the outlined requirements and the described approach, an optimization framework was set up, for which the architecture of its building blocks as well as the workflow are illustrated Figure 3.1. Before initiating the optimization and analysis process, it is essential to clearly define the framework input. The parameters subject to optimization, along with their respective boundaries, must be explicitly identified. Additionally, the foundational settings of the GA should be appropriately configured to facilitate a successful optimization process. The optimization problem, including its objectives, needs to be precisely articulated through the formulation of a well-constructed fitness function. Furthermore, an existing solution with a proven parameter configuration can be incorporated into the algorithm, allowing for further refinement and enhancement.

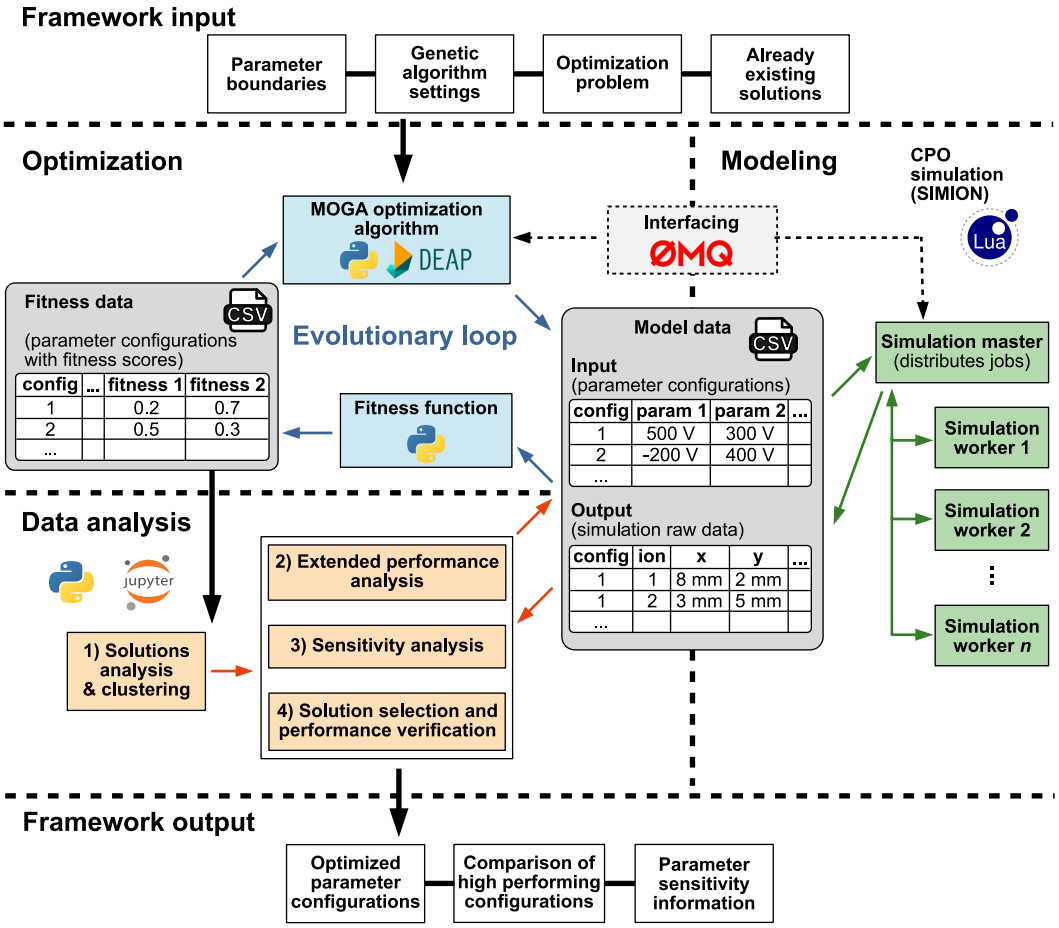

Figure 3.1: The charged particle optics optimization framework (CPOpt) employs a modular architecture. Once the framework input is defined, the evolutionary MOGA optimization process begins. A ZeroMQ-based interface enables automated communication between the GA and the CPO modeling in SIMION. Distributed simulation workers are utilized to minimize modeling time. During optimization, input/output data and computed fitness data are stored in dedicated files. After optimization concludes, a comprehensive data analysis workflow, which includes additional modeling steps, is executed, ultimately producing the framework's output.

With the defined input, the optimization process can be initiated. The MOGA generates a collection of parameter configurations, termed the initial generation. This serves as the input data for the model and may include, for example, sets of voltage values for various electrodes. This data is stored in a designated file, typically a CSV file, which is sufficient for most use cases. To obtain the system's output for each generated parameter configuration, system modeling is necessary. A custom

CPO simulation is executed using SIMION, a well-established simulation software, where the input parameter sets are processed, and raw output data is generated for each configuration. To accelerate the simulation, a distributed architecture is employed, featuring a master instance and multiple simulation workers. The workers are assigned specific parameter configurations for simulation, while the master node manages job execution, data handling, and communication. For fully automated optimization and modeling, the simulation master instance interfaces with the MOGA via a ZeroMQ-based communication protocol. The system output for each modeled parameter configuration is then evaluated using a custom fitness function, which processes the raw simulation data to produce fitness scores for each configuration and objective. These scores are stored in a separate data file and subsequently accessed by the MOGA. Through genetic operations such as selection, crossover, and mutation, the MOGA generates a new generation of parameter configurations aimed at improving fitness scores. This iterative process, known as the evolutionary loop, continues until the termination criteria are satisfied.

Upon completing the evolutionary loop of the optimization process, the data gathered from the generated parameter configurations and their associated fitness scores is transferred to the data analysis module. Through a sequence of analysis steps, the data is filtered, progressively narrowing the range of viable parameter configurations to identify the most optimal solution. This process includes analyzing the Pareto front and applying automated clustering techniques to group high-performing solutions and extract representative configurations from each cluster. The subsequent analysis phases often require additional simulations of the parameter configurations, as they involve more statistically representative particle distributions. Following a detailed performance analysis, a sensitivity analysis is conducted to assess the robustness and sensitivity of performance in response to variations in each parameter. This step, incorporating Latin hypercube sampling, facilitates a randomized local search for further optimization of the solutions. Finally, based on the filtering process and sensitivity analysis, an optimal parameter configuration is selected and validated through extended simulation.

The framework outputs not only a set of optimized parameter configurations but also a comparative analysis of the highest-performing solutions. Additionally, it offers insights into parameter sensitivity and robustness, aiding in the selection of solutions that are not only highly efficient but also stable.

3.3 Optimization and modeling

In the following, the functionality of the optimization framework is explained in terms of the MOGA, the setup of parallelized SIMION simulations for modeling and the communication between these modules with the ZeroMQ communication interface as well as the handling and transfer of data.

3.3.1 Multi-objective genetic algorithm

The process of parameter tuning can be automated through optimization algorithms. These algorithms handle selecting parameter settings, running simulations, assessing the outcomes, and exploring new configurations based on the achieved performance. In CPO design, the challenge of tuning arises due to the involvement of numerous parameters, such as the voltages of different lenses or their geometric arrangements, in achieving a specific output characteristic. Additionally, many optimization scenarios demand the balancing of multiple competing objectives, making manual tuning impractical. This underscores the need for an advanced computational method capable of navigating the large search space and handling complex objective functions. CPOpt employs a specialized GA to fulfill these optimization demands. In the CPO context, each member of the created population, referred to as an individual, represents a parameter configuration to describe the system. The individuals are assembled by genes, where each gene is a real-coded parameter value such as an electrode voltage or an electrode length [69, 119]. CPOpt incorporates a custom MOGA, developed using the open-source Python library DEAP [127]. Figure 3.2 depicts the architecture and operational flow of the MOGA.

Before initiating the optimization process, certain input data must be configured for the MOGA, as outlined below. The initial data is defined directly within the MOGA script using variables or lists. This includes parameters for the GA itself, such as crossover and mutation probabilities, the number of individuals and generations, and the precision and boundaries for the parameters being optimized. Pre-existing parameter configurations are also specified here. Additionally, the fitness function is stored in a separate Python file and imported as a module. The precision and boundaries for each parameter are set first, allowing for hard design constraints such as voltage limits imposed by system specifications to be easily incorporated into the optimization process.

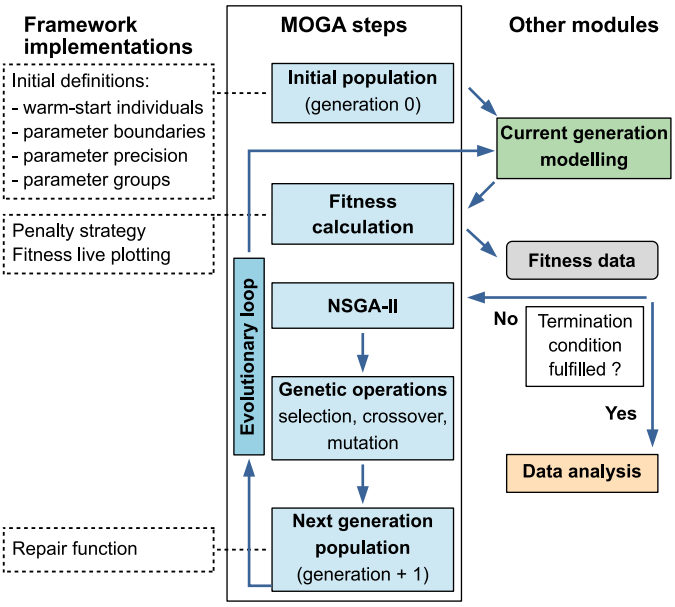

Figure 3.2: The MOGA optimization process in CPOpt involves several steps. This iterative procedure cycles through multiple generations of parameter sets within an evolutionary loop. Each set of parameters is modeled, and its fitness scores are carefully evaluated. The next generation's configurations are generated using NSGA-II along with genetic operations. The framework also includes extra features to address the specific optimization requirements of CPO.

CPO often requires the simultaneous optimization of multiple diverse parameters, such as voltage and geometric properties. In this scenario, each individual consists of genes representing values for parameters like electrode voltage, length, width, and distances. Typically, a GA will treat all genes within an individual uniformly during genetic operations. This can lead to unintended mixing of parameter types and violations of boundary conditions or precision limits. To address this issue, a functionality for grouping parameters has been implemented. In this approach, the GA generates a list of values for each individual, where each value corresponds to a gene and, therefore, a specific parameter. The order of parameters in the list remains fixed, so that each one can be accessed by its index. Parameters are grouped by defining the indices of parameters within each group, and genetic operations are applied to these groups independently. This prevents unintended interactions between different types of parameters and allows for the independent control of boundaries and precision. In CPO, this grouping method enables clear separation between parameters like electrode length, width, distance, and voltage while allowing them to be optimized

simultaneously. Consequently, there is no need to sequentially optimize geometric properties first and then adjust electrode voltages. Further, multiple groups for the same type of parameter, such as voltage, can be created, which enables the application of different precision and boundary settings to different electrodes. A practical example is when specific electrodes require a unique power supply configuration.

The optimization process commences with the MOGA, which generates the initial population of the first generation [71]. CPOpt enables the incorporation of not only randomly generated individuals but also predefined parameter configurations, termed warm-start individuals, into the initial generation. These warm-start individuals are specified prior to the start of the optimization. This approach allows the optimization to leverage one or more existing CPO designs and simulation data, facilitating the refinement of existing systems or their adaptation to new design constraints, operational conditions, or performance objectives, rather than starting from scratch. This method is particularly beneficial when combined with an elitism strategy in the GA. It can significantly reduce the overall optimization effort compared to initiating the evolutionary process without prior solutions, while still enabling exploration of a wide parameter space to discover diverse solutions. Consequently, the warm-start method serves as a foundation for the flexible adaptation of CPO instruments and enhances the versatility of CPOpt in various stages of CPO development. For example, this method supports targeted adjustments of specific parameters, such as electrode voltages, while preserving other aspects like geometric configuration.

Using this input, the MOGA generates the initial population. The parameter data for this population is directly exported into a model input file in CSV format, where each row corresponds to an individual, and each column represents a different parameter. The modeling of this population is carried out by SIMION, as detailed in Section 3.3.2, resulting in raw output data, which is saved in a designated output file, also in CSV format. The MOGA then loads this output data and computes the fitness scores for all individuals for each objective, following the predefined fitness function. The fitness function is a critical component of the optimization process, as it defines the problem and allows each solution to be evaluated based on how closely it aligns with the desired outcome. This function must be specifically tailored to each optimization scenario due to its highly case-specific nature. The basic setup of the fitness function, as implemented in CPOpt, is shown in Figure 3.3.

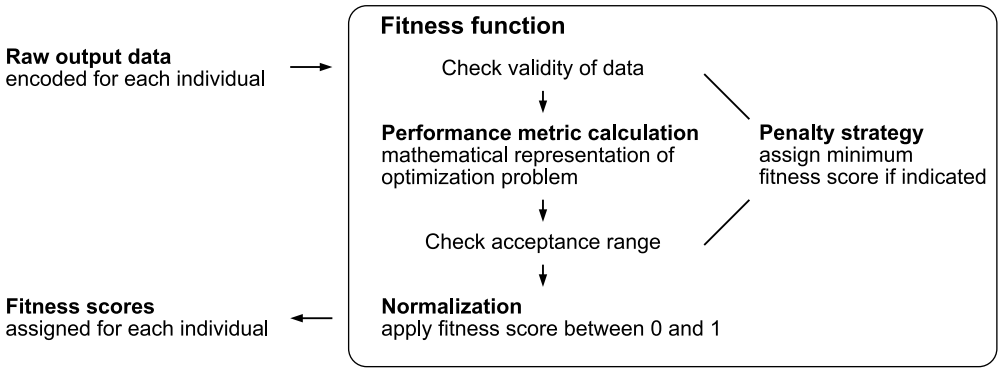

Figure 3.3: Working principle of the fitness function, as implemented in CPOpt. Raw output data is accessed by the fitness function and initially checked for validity under consideration of the penalty strategy. For individuals with proven validity, the performance metrics are calculated and reviewed again based on the penalty strategy. Lastly, the fitness scores are normalized and assigned to each individual.

Normalizing fitness scores can be advantageous, as it facilitates the comparison of different individuals. Within the CPOpt framework, a fitness score of 1 indicates perfect performance, whereas a score of 0 signifies unacceptable performance or an invalid solution. In CPO applications, certain scenarios may arise where the fitness function misinterprets raw data, leading to inaccurate assessments of a solution's fitness. For instance, situations with minimal particle transmission, resulting in a limited number of detected particles, can undermine the statistical reliability of the fitness calculations. This, in turn, can lead to misleading conclusions and negatively impact the optimization process.

To address this issue, the CPOpt framework incorporates a penalty strategy within the fitness function, designed to identify and penalize invalid data. The penalty strategy is context-specific and integral to the fitness function. One approach to refining this strategy is to conduct several iterations of the optimization using a preliminary fitness function and then analyze the distribution of the resulting normalized fitness scores. Particular attention should be given to solutions that achieve a fitness score of 1, as this may indicate an invalid case where the physical performance of the solution has not been accurately reflected in the fitness score. In such instances, it is essential to closely examine the various components contributing to the fitness score to detect any potential issues and adjust the fitness function accordingly. In Section 3.4.1, the implementation of a penalty strategy is demonstrated within the context of a CPO-specific optimization problem. This method allows for the fine-tuning of the

acceptance thresholds for different metrics within the fitness function, as well as the criteria for assigning penalties for invalid cases by setting the fitness score to 0. The fitness data collected during the optimization is saved in a separate CSV file. This data, along with other optimization criteria, is continuously monitored to assess if the termination conditions are met. Once these conditions are fulfilled, the optimization process is concluded, allowing for the initiation of post-optimization data analysis. The process continues until the specified termination criteria are satisfied.

Since the optimization process can extend over several hours, it is crucial for the user to have the ability to monitor its progress. Therefore, a live plotting feature has been integrated, which displays the current fitness values and the evolving shape of the Pareto front in real-time. This functionality enables continuous and detailed observation of the results as the optimization unfolds.

To tackle multi-objective optimization, the NSGA-II algorithm is utilized, known for its efficient and elitist approach to non-dominated sorting with low computational overhead. Initially, NSGA-II sorts individuals based on their non-domination rank and calculates crowding distances. It then incorporates elitism by preserving high-performing individuals and transferring them unchanged to the subsequent generation [121]. The next generation is formed through genetic operations including selection, crossover, and mutation. Tournament selection is used when comparing individuals based on dominance; if this is not applicable, selection relies on crowding distance instead [121, 127]. For performing genetic operations like crossover and mutation on real-coded parameters, the simulated binary crossover [123] and polynomial mutation [121] are commonly used techniques. The effectiveness of these operations also hinges on the probabilities assigned to crossover and mutation, which should be tailored to the specific optimization problem and the desired balance between exploration and exploitation. Following these operations, the population for the next generation is generated.

In complex CPO designs, a typical issue arises where maintaining solution diversity requires avoiding excessively narrow parameter ranges, such as the length and distance of electrodes. However, genetic operations often produce parameter combinations that can breach essential global design constraints, such as the maximum allowable instrument length. To address this, CPOpt includes a repair mechanism. This function iteratively and randomly adjusts the length and distance values of electrodes

while adhering to gene boundaries until the global design constraint is met. This approach ensures compliance with stringent design requirements while preserving parameter boundaries. Once these adjustments are made and the new generation population is formed, the evolutionary process resumes.

3.3.2 Physics modeling with SIMION

Each parameter setting produced by the MOGA requires a corresponding physics model to generate raw data for calculating fitness scores. This model can be represented by a physical experiment, a surrogate model, or a simulation. The upcoming section describes the procedure for performing CPO simulations with the SIMION software [60, 124].

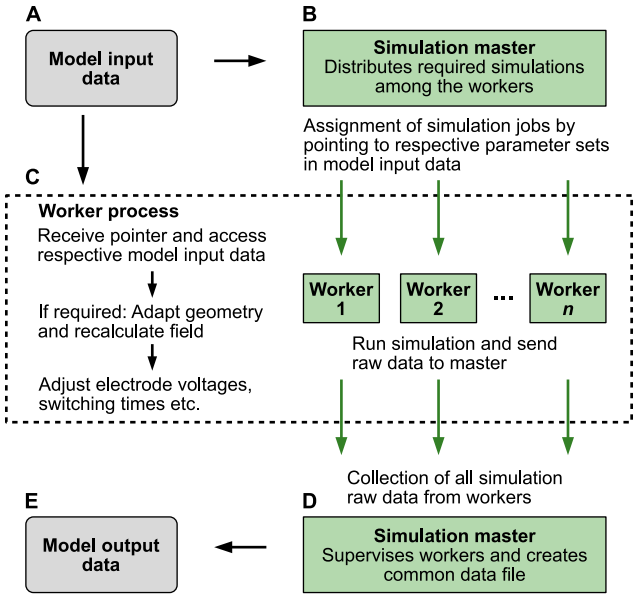

Figure 3.4: The CPO simulation involves multiple simulation workers. First, the simulation master imports the parameter configurations from the input data that need to be simulated (step A) and assigns them to different simulation workers (step B). Each worker accesses the pointer linked to its assigned parameter configuration, loads the corresponding input data, modifies the necessary model parameters for the simulation, and then runs the simulation (step C). The simulation master then collects the resulting raw simulation data (step D) and records the output data in a separate file (step E).

Figure 3.4 illustrates the overall operation of the simulation used to model the population of a given generation. The simulation master initially loads the model input data file, which contains all the parameter configurations for the individuals of the current

generation (step A). There are two approaches to conducting simulations. For less complex simulations that are not computationally intensive, a single instance of the simulation program may suffice. In this scenario, the simulation master and worker are combined into a single instance. However, for more computationally demanding optimization tasks, particularly when simulating a large number of particles through intricate field setups, the simulation process must be accelerated. In such cases, the simulation master distributes the workload across several instances of the SIMION simulation program, referred to as workers (step B). This enables parallel execution of the simulations. Since SIMION 8.2 does not natively support multi-core processing for ray tracing within a single instance, running multiple SIMION instances concurrently, even on the same computer, can enhance performance. In this configuration, one instance is designated as the master, managing communication with both the MOGA and the workers, as well as handling overhead tasks. A predetermined number of worker instances are tasked with performing the actual simulation. A ZeroMQ server-client communication protocol is established between the master and the workers, similar to the communication setup previously described for interactions between the MOGA and the simulation program.

Each worker is allocated a group of individuals for simulation (step C) by obtaining pointers to the relevant model input data. The worker extracts the necessary information regarding the parameter values from the model input data file using the specified encoding and pointer. Afterward, the worker adjusts the simulation variables based on the extracted parameter values. The optimization framework allows for the simultaneous optimization of various parameter types, including geometric parameters like electrode dimensions. A combined optimization of voltage and geometry means that the geometry of the simulated component changes for each individual. In SIMION, this requires recalculating the field using the Laplace equation before each simulation. In this framework, the adjustment of system geometries is designed so that the SIMION GEM file can directly locate the required parameters and modify the system's geometry accordingly. To achieve this in SIMION, the predefined geometry in the GEM file is converted into a fast adjustable PA for which field calculations are performed. This approach allows for a modular separation of the code for adjusting geometry and non-geometry parameters during the simulation, facilitating fully automated simulations. However, executing this for each simulation run considerably slows down the overall process. Once all parameters are adjusted, the simulation can commence. After each simulation is completed, the worker sends a

confirmation along with the recorded raw output data to the master. The simulation master gathers this data (step D) and compiles it into the common model output data file (step E) after all individuals have been simulated. The data is encoded using generation and individual numbers. Unique particle indices are employed for encoding to store information about different particles within each individual simulation. With this, the simulation work for the current generation is concluded.

3.3.3 Communication interface and data transfer

To facilitate embedding the simulation step into the optimization routine, significant attention was directed towards enhancing and automatizing the interaction between the MOGA and the SIMION modeling part, alongside improving data management processes. The open-source messaging library ZeroMQ [128] provides an efficient means for transmitting commands among various scripts and applications. Based on that, an interprocess communication tool was set up, that establishes a robust communication pattern and allows fully automated operation of the iterative search and modeling processes. The approach for storing and exchanging data among the framework modules works in line with this communication interface. Moreover, this approach will allow for the future connection of different framework modules with user-specific applications. ZeroMQ also supports the operation of distinct modules across separate machines, which is advantageous when dedicated workstations are required for simulation tasks. The methodology developed is depicted in Figure 3.5, highlighting the communication and interaction between the MOGA and the SIMION master instance.

ZeroMQ offers a range of communication patterns for interaction among various instances [128]. This framework utilizes a client-server model, facilitating bidirectional communication through a request-reply mechanism. In this setup, the MOGA serves as the client, while the simulation master acts as the server. To begin, both the optimizer and the simulation script must load the ZeroMQ library. The first step is to establish a connection to a shared ZeroMQ socket that is bound to a designated network port. With that, the MOGA starts the evolutionary process by generating the initial population of model input data (step A). This data is saved in a specific file that gets updated with input parameters across generations. To ensure clear identification throughout the optimization and analysis, each individual in the file is assigned a unique identifier composed of generation and individual numbers. The MOGA then issues a request (step B) for the simulation of the generated population

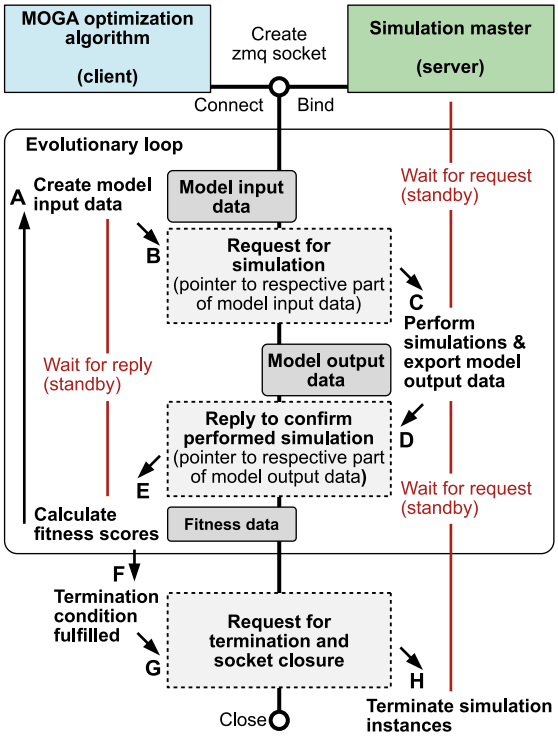

Figure 3.5: Pattern for the interprocess communication and data transfer between the MOGA optimization algorithm and the simulation master instance. The communication is facilitated through a ZeroMQ message queue in a client-server architecture. The MOGA creates input data for the modeling (step A), which is then saved in a specific file, and sends a reference to this data to the simulation master (step B) to initiate the modeling process with that data. Simulations are carried out, producing raw data that is stored in a different file (step C). Once the simulations are complete, the simulation master notifies the MOGA via the messaging queue, providing a reference to the generated raw data (step D). The MOGA then computes and records the associated fitness scores (step E). If the specified termination criteria are satisfied (step F), the MOGA issues a termination request (step G), leading to the closure of simulation instances and the communication socket on both ends (step H).

to the simulation master. In the server-client pattern, after sending out a message, the sender instance goes into standby. It then listens for the response of the recipient and the execution of its program logic is temporarily paused. The sent-out request of the MOGA includes the generation number of the newly created population, which directs the simulation master to the appropriate subset of the model input data file for simulation. Upon receiving the MOGA request, the simulation master, up to then in standby, resumes code execution and retrieves the relevant model input

data (step C). It loads all individuals from the specified generation based on their unique identifiers and initiates the simulation. Each simulation run corresponds to an individual from the population, and the raw data collected is saved in a separate data file, tagged with the generation and individual number. After completing the simulation for the entire population, the simulation master sends a confirmation reply to the MOGA (step D), indicating that the simulation has been completed. This reply also contains the generation number of the processed population and points to the relevant subset in the model output data file. Once the optimizer receives this reply, it loads the corresponding simulation data and evaluates each individual's performance by calculating fitness values, which are then stored in another file (step E). Subsequently, genetic operations are conducted to formulate the next generation's population, and the optimization process continues with the next iteration of the evolutionary loop. The optimization concludes when the optimizer meets a specified termination criterion (step F) and sends a termination command (step G) to the simulation master, prompting it to exit standby mode and cease all operations (step H). Finally, the communication socket is closed for both the client and the server.

The interprocess communication tool, was primarily developed to establish fully automated interaction of the Python-coded MOGA and the SIMION Lua-coded simulation scripts. Hence, straightforward communication between different programming languages was demonstrated, which allows further application scenarios within the optimization framework to establish interconnectivity with different other code-controlled modules.

3.4 Framework validation and post-optimization analysis

3.4.1 Test case and post-optimization data evaluation sequence

To test and validate the functionality of the CPOpt framework while steering the optimization and analysis with actual data, an exemplary CPO optimization problem was established as a test case. This setup involved two Einzel lenses positioned with an intermediate aperture, leading to a detector at the far end, as depicted in Figure 3.6. The dual lens configuration features an arrangement of ring-shaped electrodes that exhibit cylindrical symmetry. The optimization goals include reducing the beam spot size of an initially divergent beam at the detector plane and enhancing the transmission through the electrode arrangment and the aperture concurrently by adjusting the voltages and the inner radii of the six lens electrodes (specifically,

electrodes 2, 3, 4, and 6, 7, 8). Consequently, this test case embodies a two-objective optimization challenge with 12 adjustable parameters that integrate both voltage settings and geometrical configurations. The voltage applied to the electrodes was confined to a range between −2 kV and 2 kV. Additionally, the inner radius of each electrode relative to the optical axis could be modified within the limits of 3 mm to 10 mm. The voltages for the electrodes positioned before (electrode 1) and after the lenses (electrode 9), as well as for the aperture (electrode 5), were maintained at ground potential, with their shapes remaining unchanged. All simulations and computations were conducted on a workstation equipped with a 3.00 GHz CPU and 512 GB of RAM. The simulations in SIMION were executed across a total of eight instances, comprising one instance working as both the simulation master and a worker and aditionally seven simulation workers.

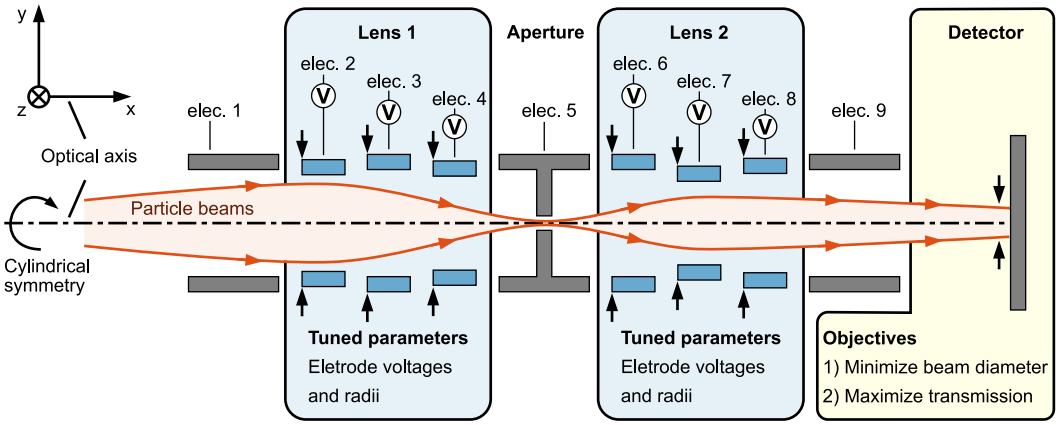

Figure 3.6: For testing and validating the optimization framework, an exemplary optimization problem was defined as a test case comprising a two-lens arrangement with an integrated aperture. An initially divergent beam passes the system and requires double focusing by the electrodes of lens 1 (electrodes 2, 3, and 4) and lens 2 (electrodes 6, 7, and 8) to meet the output objectives of minimized beam spot size and enhanced particle transmission on the detector plane. The optimization involves tuning of the voltage and inner radius for each of the six lens electrodes. However, the electrodes positioned before (electrode 1) and after the lenses (electrode 9), and the aperture (electrode 5), were not modified and remained at ground potential.

For each parameter configuration simulated, a total of n particles (either $n = 601$ or 2001, as detailed in Sections 3.4.2 and 3.4.3) were created, each with a mass of 50 amu and a charge of 1 e. The particle ensemble includes one reference particle that follows a trajectory along the optical axis with a reference energy of 1750 eV, alongside

$n-1$ particles characterized by a specific distribution of initial positions, angular motion vectors, and energies. To meet varying needs for computational efficiency and statistical validity, the total number of particles n and their respective distributions are adjusted for the simulations performed during the optimization phase compared to those required for subsequent data analysis. Further details regarding the particle distributions employed can be found in the relevant sections.

Fitness function

For the described test case, a fitness function comprising two fitness metrics $f_{1,\text{ spot size}}$ and $f_{2,\text{ transmission}}$ was defined to represent the optimization problem of the to be reduced beam spot size and increased particle transmission. This fitness function is indicated by

$$
\begin{aligned}
f_{1,\text{ spot size}} &= \begin{cases} 0 & : \text{Ref}_{\text{detector}} = \text{false} \\ 0 & : d \geq d_{\max} \\ 0 & : d = 0 \\ 1 - \dfrac{d}{d_{\max}} & : d < d_{\max} \text{ and } d \neq 0 \end{cases} \\
f_{2,\text{ transmission}} &= \begin{cases} 0 & : \text{Ref}_{\text{detector}} = \text{false} \\ \dfrac{n_{\text{detector}}}{n_{\text{total}}} & : \text{Ref}_{\text{detector}} = \text{true} \end{cases}
\end{aligned}
\tag{3.1}
$$

The beam spot size at the detector is represented by d, which is measured using the FW50. A maximum allowable FW50 beam spot size of $d_{\max} = 2$ mm has been established. The variable n represents the particle count. When fitness score values are zero, it signifies that a penalty has been applied and the solution is deemed invalid. The optimal fitness for both objectives is achieved when scores reach 1. However, in the case of beam spot size, an optimal fitness would imply an impossibly small spot size, which is not physically realizable. To ensure solution validity, it is necessary for the reference particle (Ref) to reach the detector while maintaining a trajectory along the optical axis (indicated by $\text{Ref}_{\text{detector}} = \text{true}$) for both objectives.

Simulation precision

Prior to optimization, the influence of varying simulation grid sizes and tracing precision on the results and computation times was assessed under controlled condi-

tions. Grid sizes of 0.1 mm/gu, 0.05 mm/gu, and 0.01 mm/gu, as well as trajectory quality factors of 3, 9, 18, and 27 in SIMION, were tested while maintaining all other parameters constant. The effects on the FW50 beam spot size, transmission, and total simulation time were measured. Reducing the grid size from 0.1 mm/gu to 0.05 mm/gu resulted in a doubling of the simulation time, while further reducing it to 0.01 mm/gu led to a twelvefold increase in computation time. Transmission remained unaffected, and the spot size showed variations of up to 10 µm, equivalent to a 1.10 % change in beam spot size. Adjustments to the trajectory quality factor caused a spot size variation of up to 5 nm (or 0.55 %), without any impact on transmission or simulation time. Based on these findings, a grid size of 0.1 mm/gu and a trajectory quality factor of 3 were selected for further simulations, balancing accuracy with computational efficiency.

Post-optimization analysis workflow

A structured workflow for data analysis and optimization was established to identify the most optimal parameter configuration. The results of the MOGA optimization, due to its numerous adjustable parameters, can initially appear complex and overwhelming. Therefore, it is essential to implement robust data analysis methods to increase transparency and systematically filter the data. This process involves gradually narrowing down the pool of viable parameter configurations, while additional data is collected to support and validate the final choice of the most appropriate configuration. The process begins with an examination of the optimization results and an initial assessment of trade-offs between objectives. Using standard unsupervised learning techniques, clusters of relevant solutions are then automatically identified, and representatives from each cluster are selected. These cluster representatives are subjected to further analysis in subsequent post-optimization steps, where simulations using a more statistically significant particle distribution provide preliminary quantitative estimates of the physical performance of these optimized solutions. This step helps to further refine the pool of viable solutions. Finally, a robustness and sensitivity analysis of the performance within the remaining solution clusters is performed using a Delta Moment-Independent Measure (DMIM) sensitivity analysis [130, 131], supported by targeted Latin hypercube sampling (LHS) [132].

3.4.2 Analysis of multi-dimensional solution space

The optimization process for this test case involved 120 individuals per generation. The termination condition was set to abort the optimization after 100 generations. The GA used a crossover probability of $P_{\text{crossover}} = 80\,\%$ and a mutation probability of $P_{\text{mutation}} = 30\,\%$. Particular care was taken when defining the particle distributions. To enhance computational efficiency for this extensive optimization model, a relatively low particle count of $n = 601$ was chosen. The particle distribution was kept consistent across all simulations to minimize noise introduced by variations in initial particle conditions. With the exception of one reference particle, the remaining particles were divided into six groups, each comprising 100 particles. In each group, one particle parameter was varied, while the others were held constant at reference values. Specifically, three groups were created where either the initial energy $E = [1730\,\text{eV}; 1770\,\text{eV}]$, the initial off-axis position $y = [-2\,\text{mm}; 2\,\text{mm}]$, or the initial angle of the motion vector relative to the optical axis $\alpha = [-2°; 2°]$ were adjusted in uniform steps. Additionally, three more groups were formed by simultaneously varying two parameters (energy and off-axis position, energy and angle, or off-axis position and angle) within the same intervals but with smaller step sizes to generate 10 distinct values per parameter.

The optimization and simulation process with these settings took a total of 10 h 35 min, including 10 h 29 min for the simulations and 6 min for MOGA-related tasks and interprocess communication. The fitness scores for both objectives were scatter-plotted, as shown in Figure 3.7 (a), for all individuals generated throughout the optimization. This delivers the Pareto diagram providing initial insights into the obtained fitness scores and application of penalty. The Pareto front, which is clearly visible, highlights the trade-off region where one objective cannot improve without compromising the other [121]. Optimization workflows using Pareto techniques, typically select a solution from this front based on the preferences and custom trade-offs. However, further data evaluation can assist this selection process with higher level information to finally provide a more meaningful solution. For this reason, a region of interest (ROI) for further evaluation was defined for fitness values of $f_{1,\,\text{spot size}} \geq 0.8$ and $f_{2,\,\text{transmission}} \geq 0.8$, comprising both dominated and non-dominated individuals.

The fitness scores and parameter values of the contained individuals of the ROI were visually correlated to determine trends in the behavior. The complexity of visualizing many parameters across multiple parameter sets is addressed using parallel coordinate plots (PCPs), which have been suggested as a powerful visualization tool [126].

Figure 3.7 (b) illustrates a PCP for the individuals in the defined ROI. Although the number of parameter sets is still considerable, the PCP reveals clusters of solutions with similar parameter distributions. To further refine the analysis, the k-means clustering algorithm, commonly used in unsupervised machine learning, was applied to identify a predetermined number of clusters [126, 133]. For this particular test case, 10 clusters were identified. In the subsequent analysis, selecting one representative individual from each cluster as the individual closest to the cluster's centroid, proved useful [126]. This step ultimately yielded a set of 10 cluster representatives, each characterized by high performance but distinct parameter distributions.

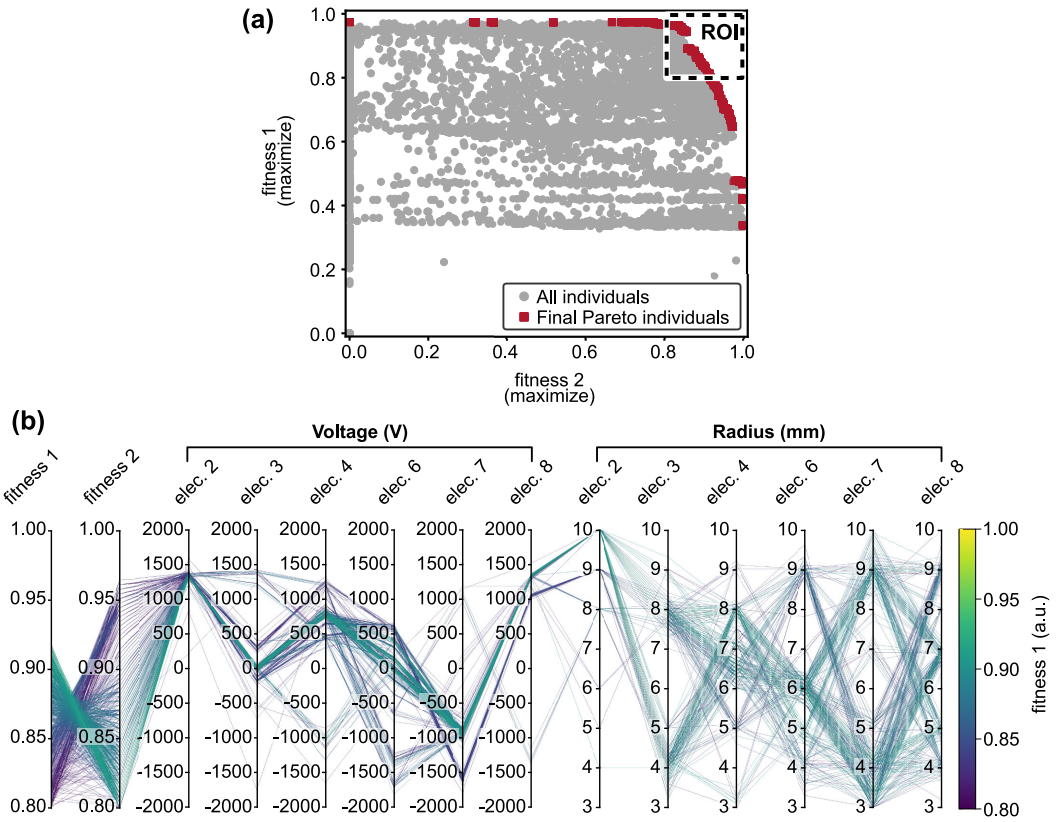

Figure 3.7: (a) The optimization finally delivers a Pareto diagram containing the normalized fitness scores for all the created individuals. The final Pareto front comprises the non-dominated individuals. A ROI with fitness scores for objective 1 and 2 being higher than 0.8 was defined. (b) All the contained individuals in the ROI were further evaluated by means of correlation of their fitness scores with the parameter distribution in a PCP

3.4.3 Validation of physical performance

The selected cluster representatives undergo a more detailed performance analysis using a statistically significant particle distribution. This entails re-modeling and simulating each cluster representative with the updated particle distribution. For each parameter configuration, $n = 2001$ particles were generated. Unlike the optimization process, where particles were distributed in a uniform step sequence, the new particles follow a Gaussian distribution with narrower boundaries to more accurately represent real-world conditions. The specific particle distributions applied are defined as follows:

- Initial particle position: Three-dimensional Gaussian distribution defined by the mean vector of the initial particle position (x, y, z) at $(10\,\mathrm{mm}, 0\,\mathrm{mm}, 0\,\mathrm{mm})$ and a standard deviation $(\sigma_\mathrm{x}, \sigma_\mathrm{y}, \sigma_\mathrm{z})$ of $(0.5\,\mathrm{mm}, 0.5\,\mathrm{mm}, 0.5\,\mathrm{mm})$;
- Initial particle direction of motion: Three-dimensional angular Gaussian distribution defined by the normalized mean vector of the initial particle direction of motion $(d_\mathrm{x}, d_\mathrm{y}, d_\mathrm{z})$ of $(1, 0, 0)$ and a standard deviation of the angle with the optical axis of $(\sigma_\mathrm{dx}, \sigma_\mathrm{dy}, \sigma_\mathrm{dz})$ of $(0.5°, 0.5°, 0.5°)$. This creates initial straight particle trajectories within a cone around the optical axis;
- Initial energy distribution: Gaussian distribution defined by the mean energy of $W_\mathrm{mean} = 1750\,\mathrm{eV}$ and a full-width half maximum of $W_\mathrm{FWHM} = 40\,\mathrm{eV}$.

The simulations for this analysis had a total runtime of 2 min. Unlike the optimization process, performance was not evaluated using normalized fitness scores. Instead, the physical performance was assessed based on the actual FW50 beam spot size and absolute transmission values. No penalty strategies or normalization techniques were applied, allowing for the extraction of quantitative data reflecting the true performance of the simulation design. To compare the performance of the simulated cluster representatives, various data visualization methods can be employed depending on the optimization problem and performance metrics. For this test case, which involves comparing beam diameter and transmission across parameter sets, using heat maps to display normalized particle density on the detector plane provides valuable insights, as illustrated in Figure 3.8.
Based on the presented data, four cluster representative individuals (gen. 49 indiv. 74, gen. 79 indiv. 52, gen. 87 indiv. 51, and gen. 96 indiv. 30) were selected for further analysis due to their high particle transmission and tightly concentrated, dense beam spots on the detector plane. These individuals will undergo more detailed examination in the subsequent analysis stages.

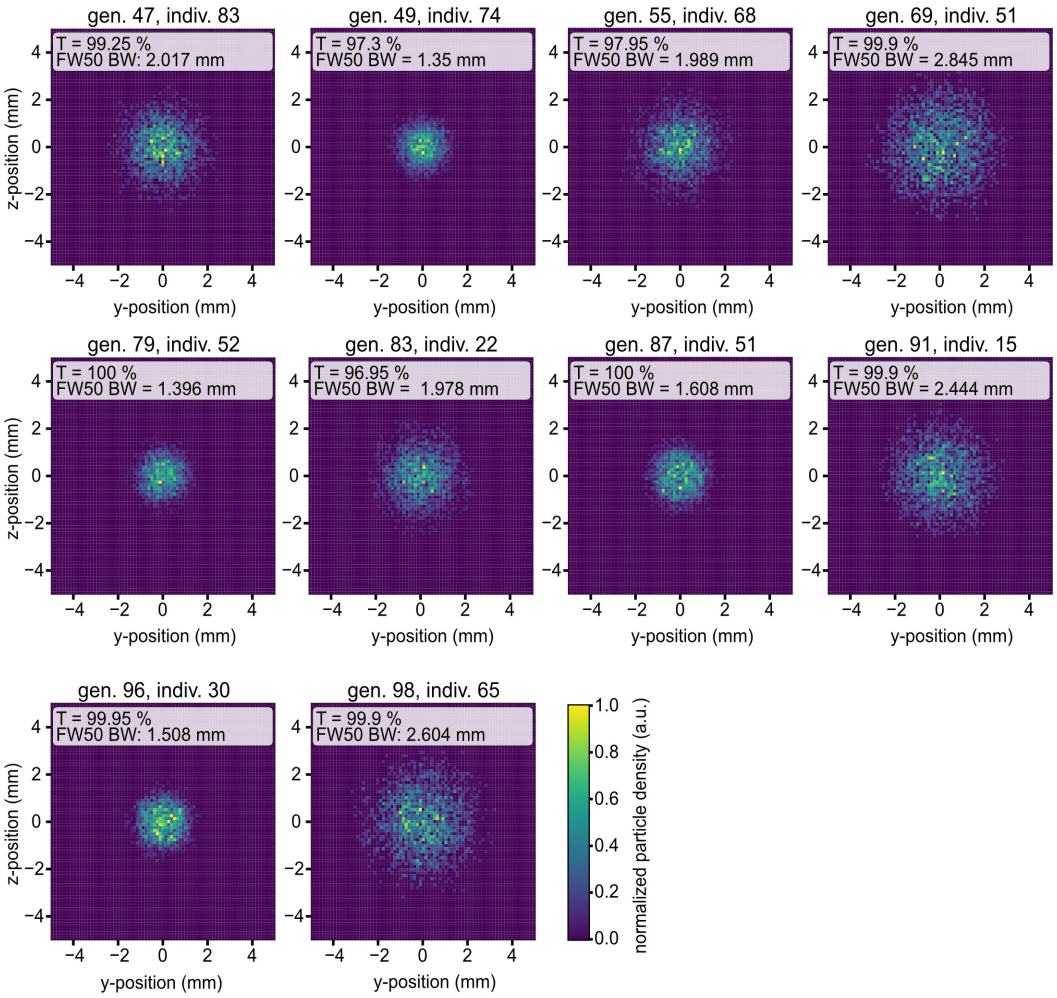

Figure 3.8: The selected cluster representatives underwent re-simulation with a statistically more representative particle distribution. The obtained results for the beam characteristic on the detector plane as well as the FW50 beam width (FW50 BW) and the transmission (T) are shown for comparison of the solutions.

3.4.4 Evaluation of parameter sensitivity

Besides high performance, the robustness of a solution against parameter deviations is crucial for selecting a suitable candidate. For instance, high-voltage values applied to an electrode often deviate from the intended threshold, so a similar output characteristic despite these variations is desirable. Therefore, the stability of high-performance cluster representatives must be examined through global sensitivity analysis.

Global sensitivity analysis

A sensitivity analysis asses the relationship between the variable input parameters and the corresponding model output [134]. In global sensitivity analysis, all the input variables are varied at a time to evaluate their influence on the output. Besides the influence of isolated tuning of a single parameter, also the interaction between the parameters is examined with this [129, 131]. The analysis generates sensitivity indices for each parameter, indicating both total sensitivity (ST) and interactions with other parameters (S1) [134]. A method providing this capability is DMIM [130], whis was applied in this framework. DMIM looks at the entire distribution for the input and the output and can handle also interaction of parameters. It finally delivers sensitivity indices in the range from 0 to 1, where 0 indicates no dependence of the output on the respective parameter and 1 means, that the output is entirely determined by the input parameter.

Latin hypercube sampling

Sensitivity analysis requires specific sampling of the parameter space based on a defined sampling scheme in order to evaluate the influence of parameter changes on the output. Numerous parameter combinations are generated within set boundaries around the representative cluster's parameter values. The LHS allows pseudo-random sampling for multi-dimensional solution spaces within certain boundaries with high uniformity. Thereby, the range of each variable is divided into equal intervals where each interval is sampled only once such that the risk of clustering is effectively reduced [129, 132]. For sampling a solution with N variable parameters, an N-dimensional hypercube is applied. To properly evaluate the influence of parameter changes on the output by the subsequently applied sensitivity analysis, the number of the created samples $S = k \cdot N$ must be at least a few times (k) higher than the dimension of the parameter space N [129].

Sampling and sensitivity evaluation

Before initiating the LHS and sensitivity analysis based on the implementation from SALib [135], the four high-performance solution cluster representatives identified in Section 3.4.3 were examined based on their parameter values. This inspection revealed that three of the four representatives (gen. 79 indiv. 52, gen. 87 indiv. 51, and gen. 96 indiv. 30) shared closely distributed parameters, leading to their grouping into Region 1. In contrast, the fourth representative (gen. 49 indiv. 74) exhibited

distinctly different parameter distributions, designating it as Region 2. To optimize computational resources, Latin hypercube sampling was applied to these two regions collectively, rather than individually for each representative. Sampling with LHS focused on a narrow range around each region's specific parameter values, enabling targeted and efficient analysis. Sampling boundaries were set at $\pm 50\,\mathrm{V}$ for voltage parameters and $\pm 1\,\mathrm{mm}$ for radius parameters. For the test case with $N_{\mathrm{parameters}} = 12$, LHS was applied with a sample size $S = 100 \cdot N_{\mathrm{parameters}} = 1200$, which provided a good compromise for statistically representative coverage of the search space and required computational effort. Simulations were conducted for the sampled configurations, with each region's simulations taking approximately 3.5 h.

The subsequent DMIM sensitivity analysis determined the real performance values and, ultimately, the sensitivity indices for each parameter in both regions. The analysis revealed that Region 1 exhibited lower sensitivity indices overall, indicating reduced sensitivity and parameter interaction compared to Region 2. Figure 3.9 (a) presents the derived sensitivity indices ST (total effect) and S1 (parameter interaction) for Region 1, highlighting their influence on beam spot size and detector transmission. The variations in the radii of elec. 2 and elec. 8 were found to have the greatest impact on FW50 beam spot size, affecting both the total effect and parameter interaction. Transmission was primarily influenced by the radius of elec. 2.

Figure 3.9 (b) presents the actual physical performance values for all Latin hypercube sampled parameter configurations within Region 1. A comparison with the performance of previously identified high-performing cluster representatives reveals that the LHS yields an even smaller FW50 beam spot size, while maintaining high transmission levels. This underscores the effectiveness of LHS as a randomized local search and optimization method around existing optimal solutions. This method adds significant value to the analysis process, enabling not only the identification of stable high-performance clusters but also the discovery of even better-performing solutions within those stable regions.

To focus the analysis on a high-performance regime, ROI was defined where the FW50 beam spot size is below 1 mm and transmission exceeds 98 %, as marked by the dashed box in Figure 3.9 (b). The minimum and maximum parameter values within this target area were determined, as shown in Figure 3.9 (c). By calculating the centroid of all parameters and solutions within this range, a high-performance solution with a sufficient safety margin can be identified, as indicated in Figure 3.9 (c).

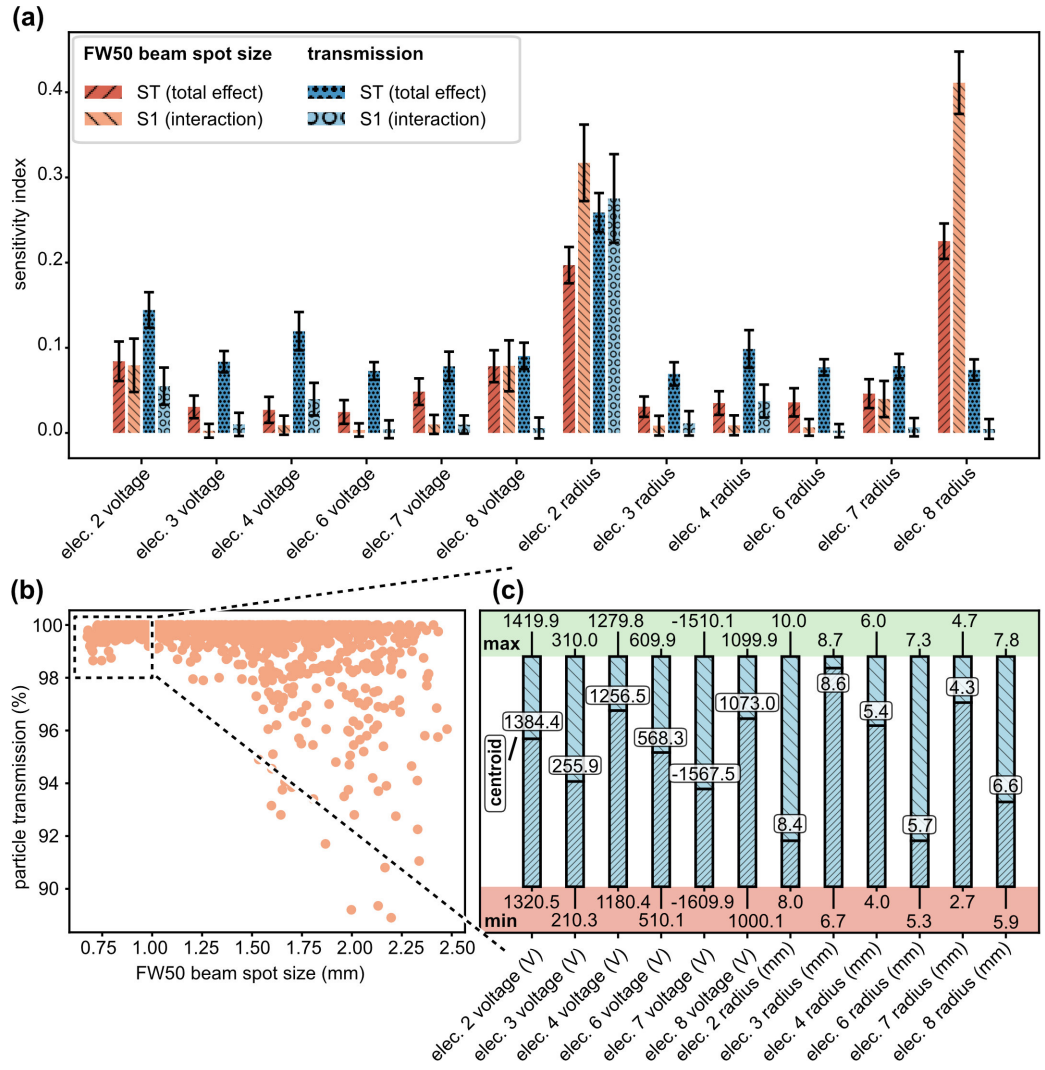

Figure 3.9: Latin hypercube sampling around the up-to-then optimal solutions comprised in Region 1 was applied to perform a subsequent DMIM sensitivity analysis. (a) The sensitivity indices for the total effect (ST) and the interaction between parameters (S1) were derived for all parameters and both FW50 beam diameter and transmission. (b) Some of the new sampled parameter configurations delivered even improved performance compared to the Region 1 solutions. A ROI was defined for further evaluation. (c) The minimum and maximum parameter values were identified for the ROI and the centroid value was determined for each parameter, finally providing high performance and stability.

3.4.5 Solution selection and verification

The centroid calculated for the final target area in the Region 1 samples was identified as the optimal solution. The corresponding parameter values for this solution are presented in the center boxes of Figure 3.9 (c). To complete the analysis process, this solution underwent verification through a repeated simulation with identical settings, followed by a manual review of the particle trajectories. The final optimized configuration, including the resulting trajectories and beam spot characteristics, is illustrated in Figure 3.10.

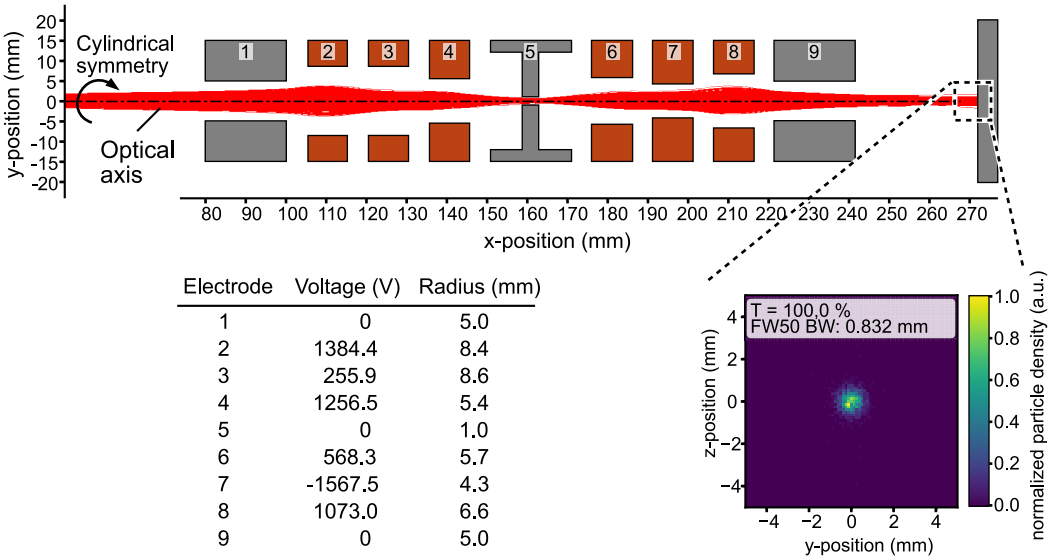

Electrode	Voltage (V)	Radius (mm)
1	0	5.0
2	1384.4	8.4
3	255.9	8.6
4	1256.5	5.4
5	0	1.0
6	568.3	5.7
7	-1567.5	4.3
8	1073.0	6.6
9	0	5.0

Figure 3.10: The identified parameter values for the most suitable solution were verified by a repeated simulation and visual consideration of the ion trajectories. Compared to the solutions, obtained through the actual optimization process, the post-optimization data analysis finally provided a stable solution with even better performance in terms of beam profile and transmission.

This solution emerged from a comprehensive yet efficient computational search strategy and demonstrated superior performance compared to the Pareto-optimal solutions identified during the initial optimization phase. Furthermore, sensitivity analysis of two critical performance metrics, beam width and transmission, enabled the selection of a solution with enhanced stability. This benchmarking exercise highlights the effectiveness of the optimization framework for CPO, showcasing its ability to flexibly address complex optimization problems while enabling further performance and stability improvements through post-optimization analysis.

Although the runtime for the initial optimization was approximately 1.5 times longer than the combined runtime of the post-optimization simulations, which took about seven hours, this ratio can vary significantly based on factors such as the number of individuals, generations, and the selected particle count during optimization. In some cases, the computational effort required for post-optimization may dominate. The simulations involving Latin-hypercube sampled configurations can be particularly time-consuming, especially when multiple sampling regions need to be evaluated during sensitivity analysis. Nevertheless, as demonstrated in this test case, the additional computational effort can result in substantial benefits.

3.5 Summary and conclusions

Optimization within the context of CPO is critically significant, as the advancement of innovative tools relies heavily on robust algorithms. To enhance the accessibility and speed of this process, a thorough and adaptable integration of all necessary modules for optimization, modeling, and data analysis is essential, something that is currently lacking in its entirety. The CPOpt framework has been developed to offer enhanced capabilities for MOGA optimization, featuring effective parameter grouping and functionalities that meet global design criteria. It allows for the simultaneous optimization of various parameter types, such as electrode voltage and geometric configurations, with the ability to independently set parameter limits and precision levels. Existing parameter setups can be integrated into the optimization process to expedite outcomes and improve solutions based on prior designs. The framework includes methods for creating custom fitness functions, incorporating penalty strategies as needed. The MOGA operates automatically and seamlessly with the CPO simulation platform SIMION, facilitated by a specially designed interprocess data exchange and communication tool. Additionally, strategies for parallelizing the CPO simulation within SIMION have been introduced to speed up modeling and potentially distribute tasks across multiple machines. A standardized workflow has been established for assessing extensive optimization data, specifically designed to address the common multi-objective optimization challenges in the CPO field. This allows for the identification of high-performing and stable solutions through a systematic filtering of the solution space. The integration of optimization process modules with a comprehensive data-processing workflow enables capabilities that surpass those of most existing techniques in CPO. The analysis methodology enables the extraction of essential information from complex optimization data sets

in a structured and iterative fashion. Furthermore, incorporating global sensitivity analysis along with Latin hypercube sampling in the evaluation of post-optimization data significantly enhances existing workflows. Global sensitivity analysis provides insights into how variations in parameters influence instrument output, thereby shedding light on the robustness of proposed solutions. Meanwhile, the application of Latin hypercube sampling as a local and randomized optimization strategy within an already identified high-performance solution space has shown promising outcomes. The modular design of the CPOpt framework allows for easy customization and the replacement or extension of modules. In particular, the integration of other simulation tools capable of calculating and managing magnetic fields could further broaden the applicability of CPOpt. Given that the modeling process through SIMION is crucial for time efficiency, exploring the use of surrogate models in future developments should also be considered.

4 Design and Development of a MRTOF Mass Spectrometer

To develop a high-performance MRTOF mass spectrometer, profound simulation work is substantial to derive a solid instrument design and operation concept, which is the basis for all subsequent prototyping work. This chapter describes the design and development work, based on analytical approaches and CPO simulation and optimization for the novel MRTOF instrument. The modular design of the instrument itself allowed to split the development work on the main components, which are the mass analyzer and the ion source and injection system. The complete instrument's operation was successfully validated through simulation.

4.1 Instrument overview

4.1.1 Requirements and objectives

The principle-based fast and comprehensive mass analysis in MRTOF devices and the high sensitivity and resolution available facilitate application scenarios in nano-analytics, space exploration and beyond. The instrument was primarily designed as a technology demonstrator for future new miniaturized mass spectrometers and comprises besides the MRTOF mass analyzer a pulsed ion source and injection system and a fast time-resolved ion detector. Peripheral components such as power supplies, fast electronics and the vacuum system are not considered at this point.

The MRTOF instrument shall cover compact dimensions with the mass analyzer as the main optical component providing a length of no more than 20 cm and a

height and width below 10 cm. Further, the instrument shall provide a design without moving parts to reduce the probability for maintenance of the optical components. To meet the demands of various applications, the spectrometer must operate flexibly in different modes, each offering distinct performance characteristics. The mass analyzer requirements for the mass resolving power and transmission in these performance regimes are listed in Table 4.1.

Table 4.1: Requirements for the mass analyzer to achieve the mass resolving power R_{M} and transmission T across different instrument performance regimes are outlined. In this context, transmission is defined as the ratio of the number of particles recorded by the detector to the number of particles initially introduced into the mass analyzer.

Performance regime	R_{M}	T
Broad spectrum (linear TOF)	> 60	$> 80\,\%$
Medium resolution (MRTOF)	< 10000	$> 75\,\%$
High resolution (MRTOF)	> 10000	$> 70\,\%$

Based on the given performance regimes, the instrument must operate flexibly in different ways:

- The broad spectrum regime with linear TOF foresees no reflections of the ions in the mass analyzer. Instead the ion mirrors are switched off with all electrodes being at ground potential to allow the pass through of ions from the source towards the detector directly.

- The medium resolution regime with MRTOF operation involves the reflections in the mirror fields to extend the flight path. This method increases the mass resolving power, however, to keep the unambiguous mass range still wide, only a low to medium number of reflections shall be performed.

- The high resolution regime with MRTOF requires a large number of performed full-turns in the mass analyzer to significantely prolong the flight path and thus the total flight time and the mass resolving power.

High sensitivity and SNR should be provided for all operating modes. The targeted particle energy was kept below 2 keV to keep the requirements for the voltage ranges of the electrodes and thus the necessary electronic components low.

4.1.2 Design concept

The optical design of the spectrometer was chosen to be modular and is basically divided into an ion source and injection system, a mass analyzer and a detector, as shown in Figure 4.1. This modular concept allows individual development and

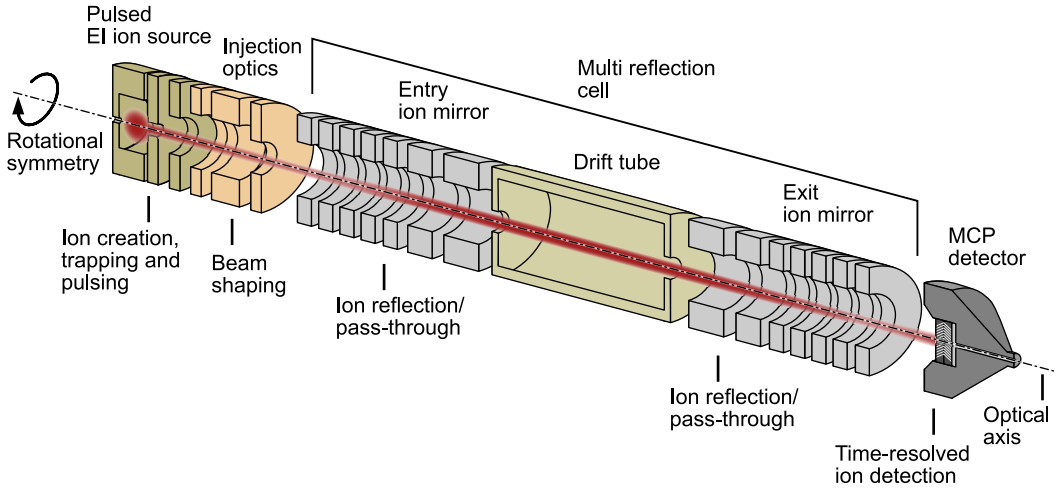

Figure 4.1: MRTOF instrument design concept, comprising a pulsed ion source, injection optics, a mass analyzer, assembled by two axially aligned ion mirrors with intermediate field-free drift tube and a detector.

consideration of the system components. The geometric dimensions of the overall system can therefore also be scaled and the performance characteristics adapted. This scaling option allows the given spectrometer design to be optimized for a wide range of specific applications. The optimization framework described in the previous chapter can be used for this purpose. The performance requirements of the scaled system can be quickly integrated into the optimization to identify the new optimal system parameters. The modular structure is also advantageous in the development process of the overall system. Since the complexity of the simulation-based optimization, as well as the data collected, is directly dependent on the number of electrodes and particles to be simulated and several full-turns must also be taken into account in the MRTOF structure, a consideration of the entire instrument in the modeling is too complicated, too slow and too resource-intensive.

A cylindrical symmetry with an alignment of all components along the optical axis was chosen for the spectrometer for various reasons. On the one hand, this significantly simplifies and accelerates the simulation and optimization process. On the other

hand, the cylindrical symmetry facilitates the compensation of aberration effects due to off-axis trajectories, as a simplified two-dimensional case can be assumed due to the symmetry. Furthermore, such a configuration also allows geometric scaling of the system without changing the essential optical properties. A closed-path configuration for the ion trajectories is possible with the planned setup, so that the different operating modes mentioned above can be realized.

The fast time-resolved ion detector is an integral part of the instrument. A commercially available detector with small physical dimensions and sufficient detection speed must be selected. Simulations of the mass analyzer, as described in Section 4.2, delivered information about the obtainable time spreads for the iso-mass peaks. Based on this and the available dimensions, the MCP-type detector APD 2 APTOF (Exosens/ Photonis, Merignac, France), featuring two stacked MCP layers in chevron arrangement, was chosen. It provides a minimum electron gain of 2×10^6 and a maximum pulse width (FWHM) of 350 ps thus allowing rapid signal processing and high sensitivity. The operating concept of the detector for positive ions involves applying a negative potential to the front side of the MCP, enabling the efficient and fast detection and analysis of the ions of interest. Within all the simulations, a voltage $U_{\text{MCP, front}} = -4\,\text{kV}$ was applied. As the simulations in this chapter only cover the ion tracing until the collision with the detector surface, the voltages applied to the MCP backside $U_{\text{MCP, back}}$, the detector grid $U_{\text{out, grid}}$ and the anode U_{anode} are not considered in the simulation. To avoid an accelerating field in the otherwise field-free drift region, created by $U_{\text{MCP, front}}$, a fine grid was placed before the detector and put at ground potential such that the accelerating field is confined between this grid and the detector.

4.1.3 Operation concept

Time focus shifting

To facilitate rapid and simple adjustments to the number of full-turns or the ion dwell time, especially in MR mode, without requiring further modification of the time focus position, the mass analyzer was set to maintain an energy-isochronous state at the same position after each full-turn [136]. This assumes that, in MR mode, the reflection cell has a symmetrical potential curve due to identical mirror fields, ensuring that both mirrors have the same focal distance. This makes the isochronous operation of the MR cell independent of the number of performed full-turns N. However, two

situations require to shift the time-focus plane: First, if the primary time focus plane, created by the source and injection system is not located in the center of the mass analyzer, the first reflection in in the exit mirror (injection mode) must guarantee to shift the focus to the center of the MR cell by applying a different potential setting than for the MR mode. Second, the detector plane must finally provide an isochronous state, such that the time focus plane must be shifted from the MR cell center to the detector with the last reflection in the entry mirror (ejection mode). Hence, another voltage setting at the entry mirror must be applied for this mode.

Operating modes

To meet the requirements of operating the spectrometer in different ways (linear/ MRTOF) and implement the time focus shifting there must be different operating modes for the mirrors in the mass analyzer. These operating modes involve different potential settings for the ion mirrors [136], as illustrated in Figure 4.2.

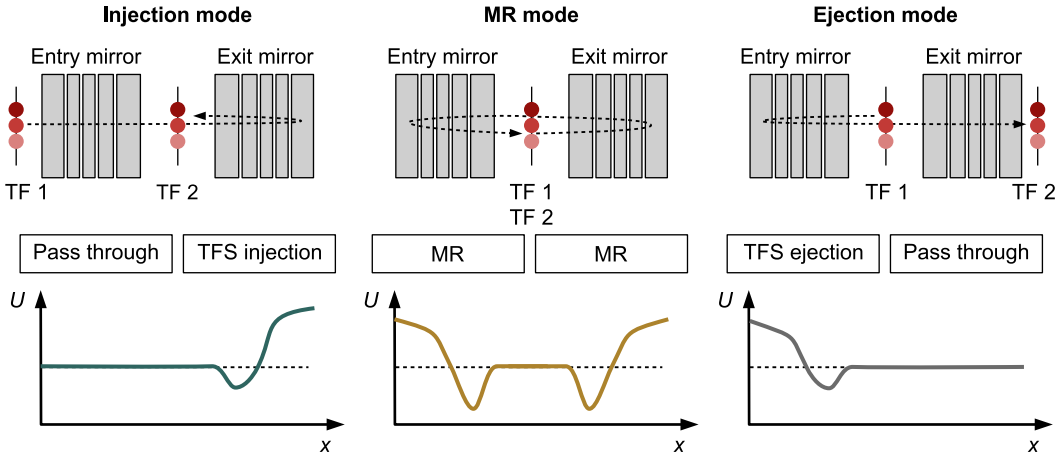

Figure 4.2: Operating modes for the mass analyzer to allow the conduction of a full MRTOF measurement and to enable time focus shifting to keep the overall operation energy-isochronous.

In the closed-path MRTOF configuration, particles must first enter the MR cell before performing the multiple full-turns in the mass analyzer. The introduction of particles into the mass analyzer necessitates the injection mode, which applies a pass-through potential setting to the entry mirror. Particles coming from the ion source and injection optics transmit the entry mirror and get reflected by the exit mirror, in which a high-voltage potential setting (time focus shift (TFS) injection) is applied. This potential setting creates a reflecting electric field in the mirror, which

takes the primary time focus (TF1) as an object plane and shifts the secondary time focus (TF2) of the ions onto the central plane of the MR cell as the image plane.

In the MR mode, the particle oscillation between the mirrors is kept stable and energy-isochronous. Both ion mirrors apply the same potential setting (MR), which takes the central plane as the object plane for the primary time focus and as the image plane for the position of the secondary time focus.

The ejection mode finally allows the ions to exit the MR cell after the required dwell time in the mass analyzer to be recorded by the detector. The entry mirror thereby applies a potential setting (TFS ejection) to shift the time focus plane from the MR cell center onto the detector plane to finally have a full isochronous MRTOF operation. The exit mirror is switched to a potential setting (pass through) at ground, such that ions can transmit this mirror.

Besides the operation as a MRTOF, also a linear TOF operation is possible by switching both ion mirrors to the pass through potential setting, such that the mass analyzer itself is only used as a drift tube. To keep the overall instrument isochronous, the primary time focus created by the source must be placed on the detector plane, as described in Section 2.1.2, by tuning the acceleration stage of the ion source.

The time focus shift with each operating mode facilitates the energy-isochronous MRTOF concept, as the final position of the time focus becomes independent of the number of performed full-turns in the mass analyzer [136].

Mass range selection

To ensure unambiguous mass measurement in MR operation, the instrument must be precisely set to a desired mass range. A methodology was derived to determine the times for switching the ion mirrors for ejection. This corresponds to the approach of setting the maximum dwell time in the mass analyzer so that the same number of full-turns is ultimately available for all ions of the desired mass range.

4.2 MRTOF mass analyzer

The mass analyzer is the core component of the MRTOF mass spectrometer. It consists of two opposing ion mirrors with a centrally placed field-free drift tube, forming an MR cell. This configuration extends the flight path and increases the total TOF of the ions, enabling time-resolved mass separation. In conjunction with the compensation of the energy-induced TOF errors by the ion mirrors, high mass resolving powers can thus be achieved. Despite the simple basic functional principle, the mass analyzer is characterized by a very high level of complexity in its detailed design and operation, as many parameters, target variables and physical principles interact and influence each other. The following section describes the simulation-based design, validation and optimization process for the MRTOF mass analyzer.

4.2.1 Initial ion mirror design and development

At the outset of developing the MRTOF mass analyzer, the primary objective was to design an initial gridless ion mirror and demonstrate the feasibility of achieving higher-order time focusing, as well as the potential for spatially focusing the ion beam. The simulations in SIMION, the calculations and parameter adjustments were performed manually and did not involve automated optimization at this stage. This also allowed the basic simulation and evaluation process to be developed, which served as the basis for the optimization framework developed later.
Based on the known approaches for gridless ion mirrors, a very simple design was initially chosen in which seven identical ring electrodes are arranged laterally in an axially aligned and cylindrically symmetric structure. The bipolar fields of existing gridfree ion mirrors with included acceleration lens served as a template for the design of the potential curve [137].

Simulation setup

The simulation concept for the ion mirror initially only envisages the observation of a single reflection at the ion mirror in order to consider the basic optical properties of this element. The structure and concept of the simulation as well as the geometry of the ion mirror are shown schematically in Figure 4.3
The particles were initially all generated at the same x-position along the optical axis. To determine the optical properties of the ion mirror, three different sequences with 100 particles each were generated for each simulation, whereby one parameter (kinetic energy, angle with the optical axis, off-axis position along the y-axis) were varied for

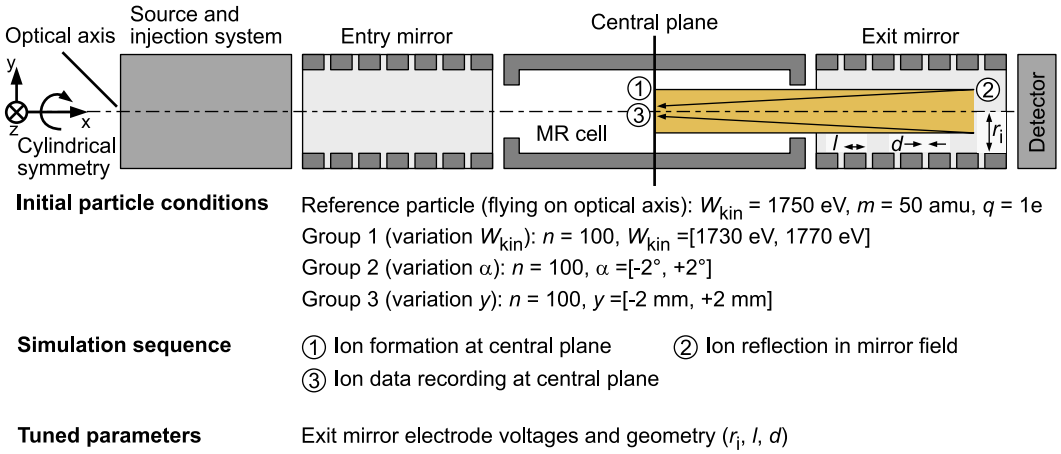

Figure 4.3: Setup of the simulation to model the gridless ion mirror and to obtain information about the focus properties after one half-turn in the MR cell. Besides one reference particle, 300 particles are created, divided in three groups. Each group shows a deviation of one distinct parameter (kinetic energy W_{kin}, angle with optical axis α, off-axis y) from the reference value in a uniform step sequence, while the other parameters are kept at the reference values.

each sequence with a uniform step size. The optimal trajectory was determined using a reference particle that traveled along the optical axis with the desired reference energy and remained unaffected by aberrations. Since all particles were generated simultaneously, the initial ion formation plane can be considered the ideal primary time focus, enabling the independent examination of aberration effects in the ion mirror. The initial ion formation plane was positioned opposite the entrance of the ion mirror to align with the central plane of the MR cell. In this configuration, the generated ions initially travel toward the ion mirror with their respective energies and motion vectors. The ions are reflected accordingly in the respective electric field of the ion mirror and move out in the direction of the initial ion formation plane after leaving the mirror field in field-free space. The particle properties are finally recorded for later evaluation when colliding with the central plane. In the overall structure of a MR cell, this would simulate a half-turn of the ions.

Parameter tuning

The geometric parameters and the electrode voltages of the ion mirror were adjusted purely manually in this phase. The aim of this manual optimization was to position both the spatial focus and the time focus in the central plane of the MR cell and to achieve a high order for the focus in each case. With the given ion sequences, several

aberration effects in the time as well as in the spatial domain could be detected, whereby the influence of the initial deviations from the ideal particle properties for the energy, the angle and the off-axis position were considered. Thereby, the interpretation of the optical properties and the achieved foci for each simulated configuration was based on the aberration plots obtained on the measurement plane.

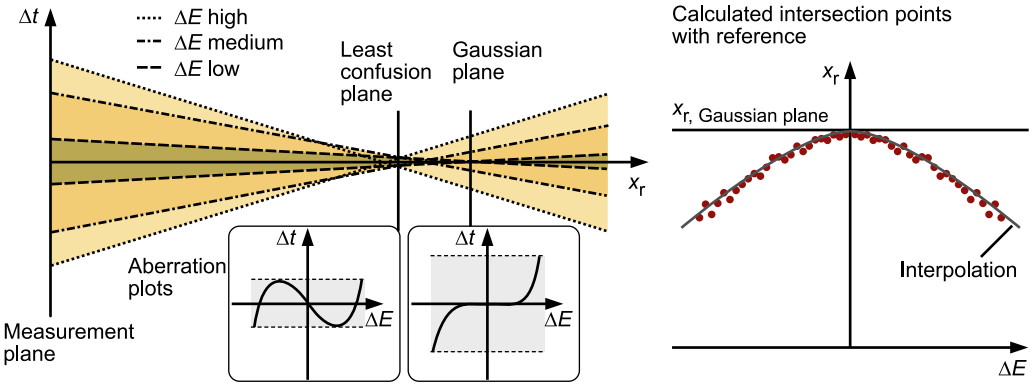

Figure 4.4: Methodology of the focal plane determination in the linear drift region by extrapolation. The schematic illustrates the determination of the Gaussian focal plane for the time domain with initial particle energy deviation. All measured particle flight time deviations Δt and energy deviations ΔE refer to the reference particle flying along the optical axis and experiencing no aberration effects.

Numerical methods were developed to make it easier to identify the position of the actual focal plane for each simulated parameter configuration. The principles considered for the focal plane determination are schematically shown in Figure 4.4 for the time domain with particles of different initial energy. The same principles apply for the spatial domain and other initial parameter deviations. On the one hand, the plane of least confusion can be selected as the focal plane, which shows the lowest total output variation over the selected input range and thus represents the plane with the smallest spot size. On the other hand, the Gaussian focal plane can be selected, which represents the focal plane for the paraxial case. To determine the focal properties and the compensation of aberration effects, the Gaussian focal plane can be considered. Therefore, the ion mirror parameters were tuned so that the Gaussian focal plane coincides with the center plane.

To determine the position of the Gaussian plane, the particle properties recorded on the test plane were used to calculate for each particle the position x_r, relative to the measurement plane, where its trajectory intersects with the trajectory of the

reference particle. For the time domain, this intersection indicates zero flight time deviation Δt. The position of the intersection is calculated by linear extrapolation. For the time domain, x_r is given for each particle by

$$x_\mathrm{r} = \frac{t_0 - t_{0,\,\mathrm{ref}}}{\frac{1}{v_{\mathrm{x0,\,ref}}} - \frac{1}{v_{\mathrm{x0}}}} \tag{4.1}$$

where t_0 and $t_{0,\,\mathrm{ref}}$ denote the flight time measured for the particle and the reference particle at the measurement plane and v_{x0} and $v_{\mathrm{x0,\,ref}}$ indicate the measured velocity contribution in the x-direction (optical axis). For the calculation of the intersection distance in the spatial domain, this term changes to

$$x_\mathrm{r} = \frac{y_0 - y_{0,\,\mathrm{ref}}}{\frac{v_{\mathrm{y0,\,ref}}}{v_{\mathrm{x0,\,ref}}} - \frac{v_{\mathrm{y0}}}{v_{\mathrm{x0}}}} \tag{4.2}$$

where y is the off-axis deviation from the optical axis and v_y is the velocity component in this axis. The approach of a linear extrapolation is possible due to the non-accelerated movement through the field-free drift region. The Gaussian plane is given by the plane where particles intersect the optical axis, in this case the reference trajectory, under the paraxial assumption. To approximate this intersection point, the extrapolated intersection points with the reference trajectory were plotted for all initial particle deviations. The actual intersection point with the reference was then determined through interpolation. The resulting distance x_r along the optical axis to the measurement plane corresponds to the relative position of the Gaussian focal plane.

Gridless ion mirror design

Using the above methodology, a geometric configuration and voltage potentials for the electrodes were worked out analytically and iteratively. In relation to the geometry of the electrodes, the inner radii to the optical axis, the width of the electrodes and the distance between them were varied. These variations ultimately delivered an initial design for the ion mirror as shown in Figure 4.5. The electrode voltage values and the geometric dimensions of this design can be found in Figure 4.6.

The ion mirror provides a bipolar field distribution, as shown in Figure 4.5 (a), by integrating an accelerating lens field before the reflecting mirror field. This lens field has a focusing effect on the particle beam in the spatial domain which allows a certain compensation of off-axis deviations of the ion trajectories from the optical axis as

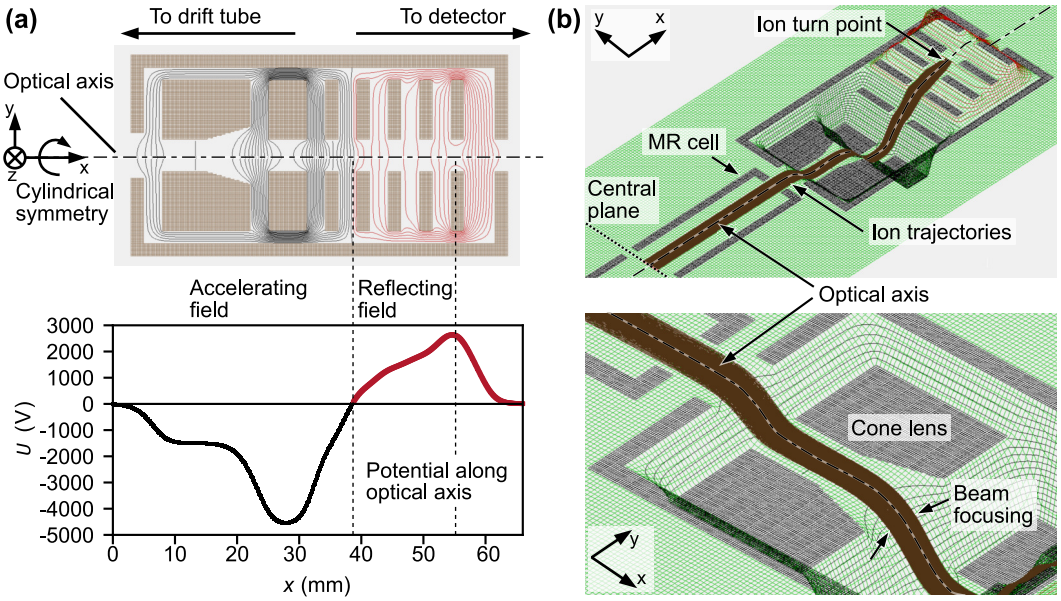

Figure 4.5: Initial design of the gridless ion mirror, obtained by manual tuning of electrode geometries and voltages. (a) The 2D side cut through the cylindrical symmetric ion mirror reveals the electrode configuration and the field distribution. The black equipotential lines indicate negative and the red lines positive potential. A bipolar field distribution, as indicated below for the optical axis, is obtained with an accelerating lens field before the reflecting mirror field. (b) The potential energy representation from SIMION shows the field gradients and the particle trajectories. The cone lens creates a strong field curvature, which allows sufficient spatial beam focusing with a low electrode length.

well as angular spread. Figure 4.5 (b) shows the potential energy representation from SIMION together with the particle trajectories. As described earlier, the start and end of the ion flight was on the central plane of the MR cell. The potential energy representation clearly shows the curvature of the electrostatic field, which gives information about the acting forces on the particles. Strong field gradients imply high forces. This finally led to a distinct design of the electrode 1, which is given by a conical recess. This shape provides strong field curvature and thus beam focusing in the spatial domain also with a moderate negative voltage applied to this electrode. Further, the cone-shaped recess facilitates the potential transition in the section of the electrode. Hence, for a certain potential gradient, the electrode length can effectively be reduced. With the strong spatial focusing effect at this electrode, incoming particles with angular divergent trajectories are first focused to allow further propagation towards the reflecting mirror field. After the reflection, the particles are

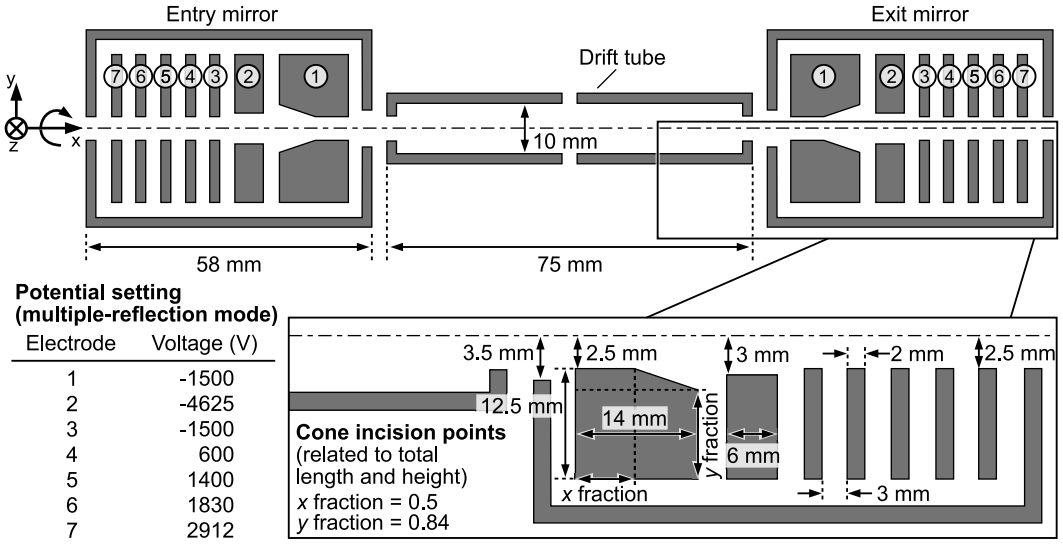

Figure 4.6: Potential setting for the operation in MR mode and the geometry parameters of the manually tuned mass analyzer. The geometry of the conical incision on electrode 1 is defined by the starting point of the incision in the x and y directions as a fraction of the total electrode length (x-axis) and the total electrode height (y-axis) respectively. This allows the conical incision to be scaled in relation to the dimensions of electrode 1.

again spatially focused when they pass the lens field in the reverse direction.

Besides the inspection of the ion trajectories and the obtained electrostatic field in the mirror, the evaluation also involved the previously described methods for the determination of the Gaussian focal plane and the characterization of the focus quality by the aberration plots. The presented design and parameter configuration yielded a calculated position of the Gaussian focus plane for the time and spatial domain very close to the central plane ($x_\mathrm{r} < 1\,\mathrm{mm}$ for all initial particle parameter variations. The aberration plots were created for the central plane and are shown in Figure 4.7 for the time domain.

Each plot shows for one particle parameter the effect of initial deviations from the reference value on the measured TOF difference $T = t - t_\mathrm{ref}$ with the reference particle. The initial particle parameter variations are given by the kinetic energy deviation $K = W_\mathrm{kin} - W_\mathrm{kin,\,ref}$, the off-axis position along the y-axis $Y = y - y_\mathrm{ref}$, and the angular deviation $A = \alpha - \alpha_\mathrm{ref}$. The reference particle properties are given by $W_\mathrm{kin} = 1750\,\mathrm{eV}$, $y_\mathrm{ref} = 0\,\mathrm{mm}$ and $\alpha_\mathrm{ref} = 0°$. The aberration plot for the time focus based on initial particle energy spread $(T|K)$ reveals already a very good performance

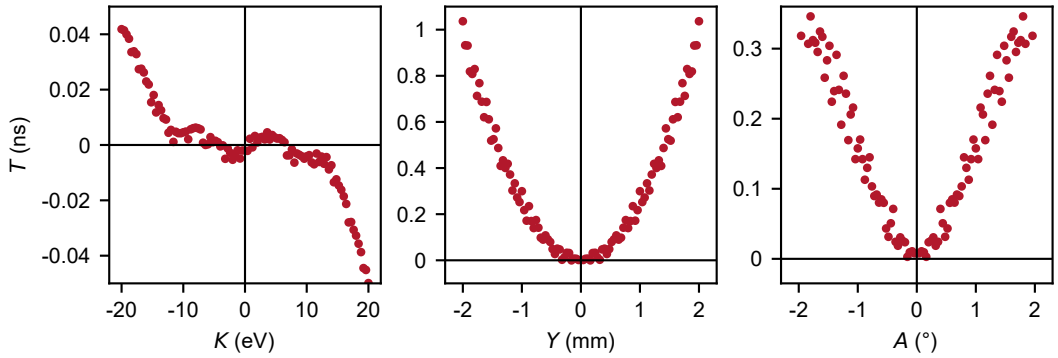

Figure 4.7: Aberration plots for the focusing in the time domain.

with fifth order aberration coefficient. The aberrational time spread per reflection in the mirror field can be kept below 0.02 ns for an energy range ±10 eV around the reference energy. Particles beyond this energy range have a larger deviation of TOF. The time focus for initial deviations of the particle off-axis positions $(T|Y)$ shows second order aberration coefficient contributing heavily to the total time spread. The time focus for initial angular spread $(T|A)$ also provides a second order aberration coefficient and shows similar time spread as $(T|Y)$. The time spread caused by the off-axis trajectories of particles is thus dominant for this configuration. Hence, a further reduction of this time spread is desirable and can preferably be achieved by improved focusing. Alternatively, the reduction of the initial parameter deviation also reduces the time spread.

For the focusing in the spatial domain, the strategy was set to focus an incoming parallel beam to a sharp point on the central plane after the first reflection. For this evaluation, the initial parameter deviation Y was applied with the same boundaries as for the time focus. The output deviation was measured based on the off-axis positional deviation from the reference $Y = y - y_{\mathrm{ref}}$. Figure 4.8 shows the aberration plot for the focusing in the spatial domain.

For the initial deviation of the off-axis position (incoming parallel beam) the aberration plot reveals that there is a focusing with third-order aberration coefficient $(Y|Y)$ towards a point. For an initial incoming parallel beam within the range ±0.7 mm, a very sharp point focus in the center of the MR cell can be reached. This already represents a good spatial focusing situation, however, particles with higher initial off-axis position do not experience very strong spatial focusing.

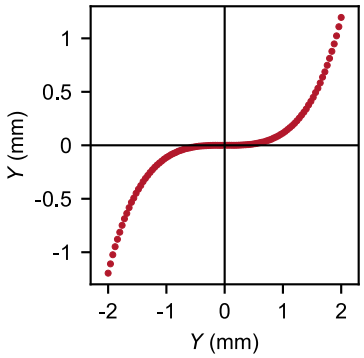

Figure 4.8: Aberration plot for the focusing of the particle beam in the spatial domain. After performing one half-turn, a parallel-to-point focusing was envisaged.

The evaluation of the aberration plots and focusing capabilities of the applied mirror setting for both the time and the spatial domain revealed, that especially the initial energy spread is already well compensated for the flight time by the time focusing of the ion mirror. Initial spatial deviations of the particles from the ideal trajectory along the optical axis, contribute much more significantly to the overall time spread. Hence, a reduction of these contributions is subject to further development and optimization. For the spatial focusing, the focusing of an incoming parallel beam to a sharp point in the center of the reflection cell was proven for a certain initial beam width. The evaluation of the focusing capabilities has confirmed that a combined time and spatial focus plane for different initial particle input deviations can be obtained. Further, the tuning process has shown, that the time and spatial focusing can be controlled independently. The mirror in the given configuration with the bipolar field allows to control the spatial focusing mainly with the accelerating lens field (negative polarity) while the time focusing is controlled primarily with the reflecting field part (positive polarity).

Iso-mass operation in multiple-reflection mode

The developed design and parameter set of the ion mirror was verified for the operation in the MR mode, where two opposing ion mirrors are used. Both mirrors provide an identical setup and utilize the same parameter sets for voltage and geometry, as indicated in Figure 4.6. Thus, the operation of the full mass analyzer is tested. For this, other than for the previously described parameter tuning and observation of a single reflection, not the optical properties in terms of aberration plots are considered but the evolution of the mass resolving power and the transmission over multiple

performed full-turns in the mass analyzer. The setup of the corresponding simulation is indicated in Figure 4.9.

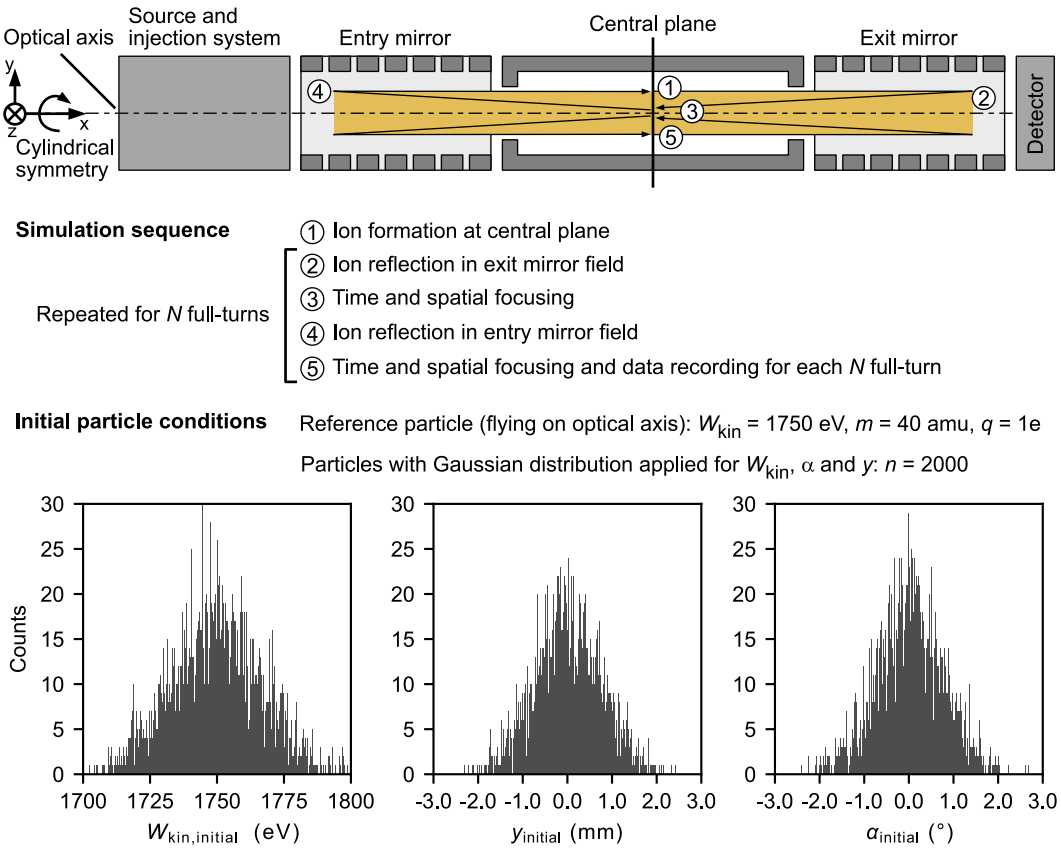

Figure 4.9: Simulation setting and applied particle distribution for the evaluation of the mass analyzer performance for R_{M} and T over N full-turns.

To obtain reliable results for these performance indicators, a statistically representative particle distribution involving Gaussian distribution of the particle parameters W_{kin}, α, y is applied as indicated in Figure 4.9. This is crucial for accurately measuring the mass resolving power and transmission over different numbers of full turns in the center of the reflection cell. An iso-mass measurement ($m/z = 40\,\mathrm{amu/e}$) is sufficient to evaluate the performance. This simulation still assumes a perfect primary time focus in the center of the MR cell as a starting condition for the ion flight. Hence, effects of the source or time focus shifting are not considered and the performance of the mass analyzer in the MR mode is characterized independently. The measurements of R_{M} and T are conducted over varying numbers of full-turns N in the center of the MR cell to understand how the system performance changes, as shown in Figure 4.10.

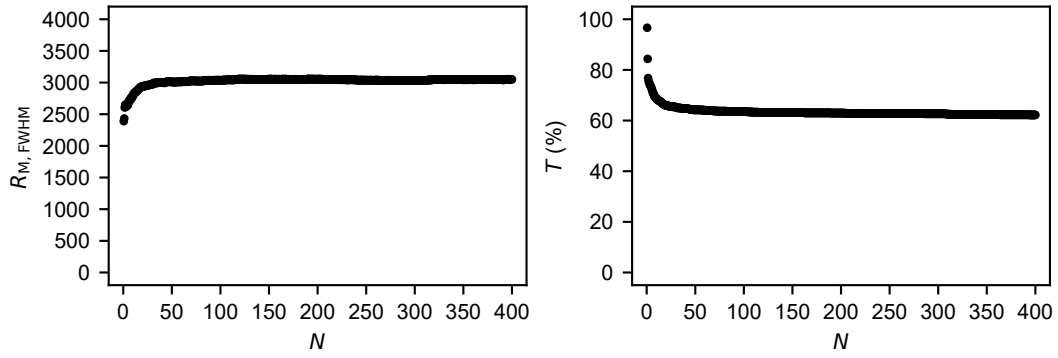

Figure 4.10: Evolution of the mass resolving power $R_{\mathrm{M,\,FWHM}}$ and the transmission T over the performed full-turns N for the operation of the mass analyzer in a MR mode with identical settings for both entry and exit mirror. The measurements were performed in the center of the MR cell. The transmission is here defined as the ratio of the number of particles recorded on the central plane after the respective number of full-turns and the initial number of particles when starting the ion flight in the center of the mass analyzer.

The mass resolving power R_{M} is calculated for each performed full-turn N for the FWHM. The results of this simulation show that the mass resolving power increases sharply for the first few full-turns and that the transmission decreases at the same time. From around 20 full-turns onwards, the curves for the mass resolving power and the transmission approach their maximum value ($R_{\mathrm{M,\,max}} = 3000$) and minimum value ($T_{\mathrm{min}} = 62\,\%$) to approximately the same extent. These values are reached after about 100 performed full-turns. The opposing curves indicate that there is initially a lower mass resolving power for the full particle distribution generated, while the decreasing transmission and the associated loss of particles narrows the distribution of particle properties and thus reduces the TOF error generated by aberrations for each reflection, so that the resolution increases. After a certain number of full-turns, a stable distribution of particle properties is reached, with minimal particle loss. As a result, the reference time for one full-turn t_{FT} and the corresponding TOF error Δt_{FT}, caused by aberration effects, stabilize for each reflection at the ion mirror, ensuring a constant mass resolving power

$$R_{\mathrm{M,\,FWHM}} = \frac{t_{\mathrm{FT}}}{2\Delta t_{\mathrm{FT}}} \tag{4.3}$$

This correlation leads to the conclusion that a gradual approximation of the particle properties in the spatial domain with each full-turn towards the reference properties enables an increase in the mass resolving power by lowering Δt_{FT}. The determined

curves for R_M and T represent the best achievable result for the given particle distribution and the defined system parameters. By incorporating the ion source and the associated initial time-of-flight error, a poorer curve is to be expected for the mass resolving power. Although the final values for resolution and transmission already reflect a high-performance design for the mass analyzer, a further increase in performance is desirable. Further, the sharp spatial focusing to the center of the MR cell with each mirror reflection is critical, as this can limit the acceptance range of the particle parameters. Especially, for particles with strong off-axis trajectory or high angular spread, the sharp spatial point-focusing leads to highly divergent particle trajectories afterwards, which can end up in collisions with the electrodes and loss of the concerned particles. Consequently, a modified method for spatially focusing the particles should be evaluated to optimize the particle parameter acceptance range and further improve the mass resolving power.

4.2.2 Design optimization

By applying a modified focusing concept and computer-aided optimization of the ion mirror design, a further improvement in performance is to be achieved. In particular, the effects of particles with an initial off-axis trajectory are to be minimized. So far, a focus in the center of the MR cell has been achieved with each reflection of the particles in the ion mirror for both the spatial and the time domain. Consequently, the optimization of the optics has always considered a single reflection (half-turn). An alternative approach is to consider the focusing of the beam for the optimization only after two reflections (full-turn), since the isochronous state only has to be achieved for each full-turn.

Instead of performing a point-to-parallel/ parallel-to-point focusing in the spatial domain for each half-turn, as applied in most of the MRTOF mass analyzers [86], an attempt can be made to gradually approximate the trajectory of the particles to the reference trajectory along the optical axis with each full-turn in the ion mirror. This approach is outlined in Figure 4.11 in comparison to the previous approach. The basic idea is to reduce the spatial particle distribution with each full-turn. On the one hand, this is intended to achieve a stable trajectory of the particles within the MR cell, which is ultimately reflected in an improved transmission characteristic. On the other hand, aberration effects caused by off-axis particle behavior in the time domain should be minimized to further increase the achievable resolution.

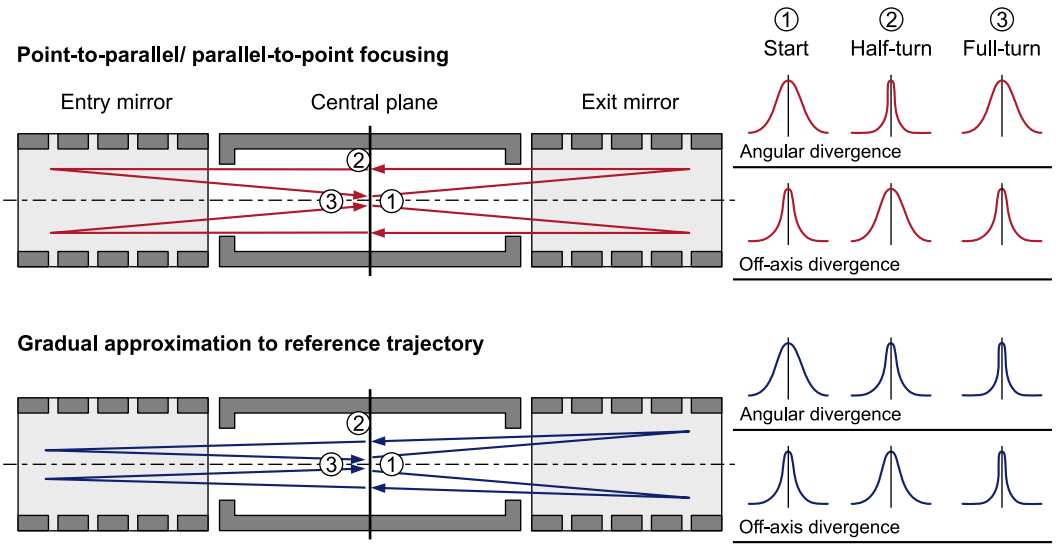

Figure 4.11: Concepts for the spatial focusing of particles in the MR operation. The point-to-parallel/ parallel-to-point focusing is the method of choice in most of the MRTOF mass analyzers and requires sharp focusing with each reflection. The gradual approximation to the reference trajectory instead applies moderate focusing with each reflection such that the angular and off-axis divergence of the particles is reduced with each full-turn.

These approaches serve as the basis for further optimization of the mass analyzer design. Due to the complexity of the optimization problem, a further manual, analytical approach is not practicable. Instead, this step was the initial motivation for the development of the computer-aided optimization framework described in Chapter 3. The further optimization of the mass analyzer was therefore carried out with the same optimization framework CPOpt and is described below. The setup of the optimization and the respective simulations is described in Figure 4.12. The optimization included the tuning of both the seven electrode voltages and 9 selected geometrical parameters. The selection of the variable geometry parameters for the optimization is based on initial manual tests, in which the corresponding parameters showed the greatest influence on the beam shape and time focusing. The tuning of the geometrical parameters included a variation of the shape of the conical recess at electrode 1. For this, the starting point of the recess was varied as a fraction of the total electrode length (x fraction) and the electrode height (y fraction).

After performing all cycles of the optimization with the required simulations, the obtained fitness of the modeled solutions was evaluated. The Pareto diagram in Figure 4.13 shows the fitness scores achieved and the progression of the Pareto

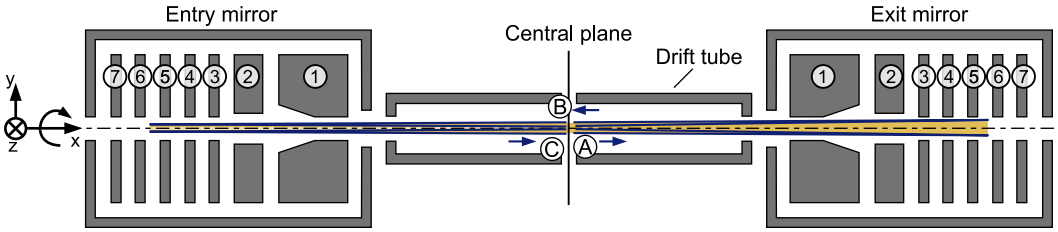

Initial particle conditions

Reference particle(flying on optical axis):
W_{kin} = 1750 eV, m = 50 amu, q = 1e

Applied particle parameter ranges for uniform step distributions:
α =[-2°, +2°], y =[-2 mm, +2 mm],
W_{kin} =[1730 eV, 1770 eV]

Group 1 variation W_{kin} n = 100	Group 2 variation α n = 100	Group 3 variation y n = 100
Group 4 nested variation α and W_{kin} n = 100	Group 5 nested variation y and W_{kin} n = 100	Group 6 nested variation y and α n = 100

Simulation sequence

Ⓐ Ion formation at central plane

Ⓑ Ions crossing central plane (half-turn)

Ⓒ Ion data recording at central plane (full-turn)

Genetic algorithm settings

Population size: 160
Max. generation: 100
$P_{crossover}$ = 80 %, $P_{mutation}$ = 30 %

Tuned parameters

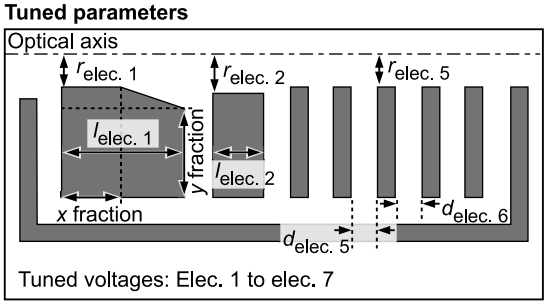

Fitness function

Penalty (assignment of fitness score of 0):
- Reference particle not measured after 1 full-turn
- Performance metrics exceeding acceptance range

Calculated performance metrics:
T, Δt (FW50), Δy (FW50), $\Delta\alpha$ (FW50)

fitness 1 (time domain)

$$1 - (\Delta t \ / \ \Delta t_{max})$$

fitness 2 (spatial domain)

$$T \cdot \left(\frac{1-(\Delta y \ / \ \Delta y_{max})}{2} + \frac{1-(\Delta\alpha \ / \ \Delta\alpha_{max})}{2} \right)$$

Figure 4.12: Setup of the optimization of the mass analyzer design applied in CPOpt. The simulations were performed for one full-turn and applied a distribution of 601 particles for each design setting. Besides the electrode voltages, selected geometrical parameters were tuned. The fitness function involves two independent objectives, considering the focusing in the time and spatial domain.

front for the best individuals. The parameter configuration, derived in the previous section through an analytical approach, was incorporated into the optimization as a warm-start individual and is shown in the Pareto diagram. An ROI was defined in the range of fitness scores greater than 0.993 for objective 1 and greater than 0.6 for objective 2. For this ROI, nine cluster-representative individuals were automatically extracted using k-means clustering. These individuals were then evaluated in terms of their iso-mass TOF spectra, as well as the mass resolving power and transmission achieved. For this purpose, these parameter configurations were simulated again. The simulation conditions were identical to those used in the iso-mass MR evalu-

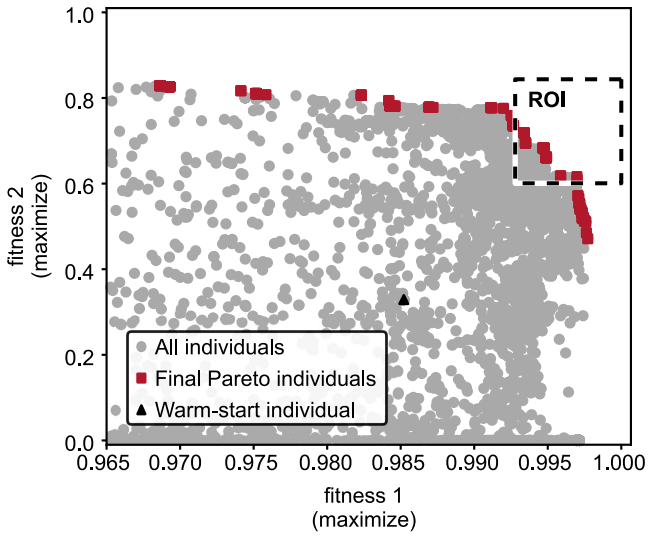

Figure 4.13: Pareto diagram for the best fitness scores obtained by the optimization. The fitness scores of the initial ion mirror design from Section 4.2.1, given as warm-start individual, is indicated. A ROI for further analysis was defined for fitness 1 larger than 0.993 and fitness 2 larger than 0.6.

ation in Section 4.2.1 and for each cluster representative 50 full-turns have been performed, to reliably estimate the behavior in the MR mode. The mass resolving power R_{M} (FWHM) and the transmission T after 50 full-turns were calculated for each cluster-representative individual and are presented alongside the obtained TOF histogram in Figure 4.14.

In direct comparison with the initial design of the mass analyzer, a significant increase was achieved for both R_{M} and T. To further reduce the solution space, cluster representatives exceeding a value of 10000 for R_{M} and 80 % for T were considered. As a result, two solutions (gen. 32, indiv. 63 and gen. 39, indiv. 55) were selected for further examination. These solutions have geometry parameters that closely resemble those of the initial mirror design. The influence of all parameters on the mass resolving power and transmission was subsequently evaluated for these solutions by means of a sensitivity analysis. For the required sampling (LHS), the parameter limits were chosen to encompass both selected solutions, which is suitable given the predominantly small deviations in the parameter values. The sample size $S = 100 * N_{\mathrm{parameters}}$ was specified as 1600. The boundaries of the sampling range for each parameter type are given in Table 4.2. Additionally, the conical incision of electrode 1 was evaluated

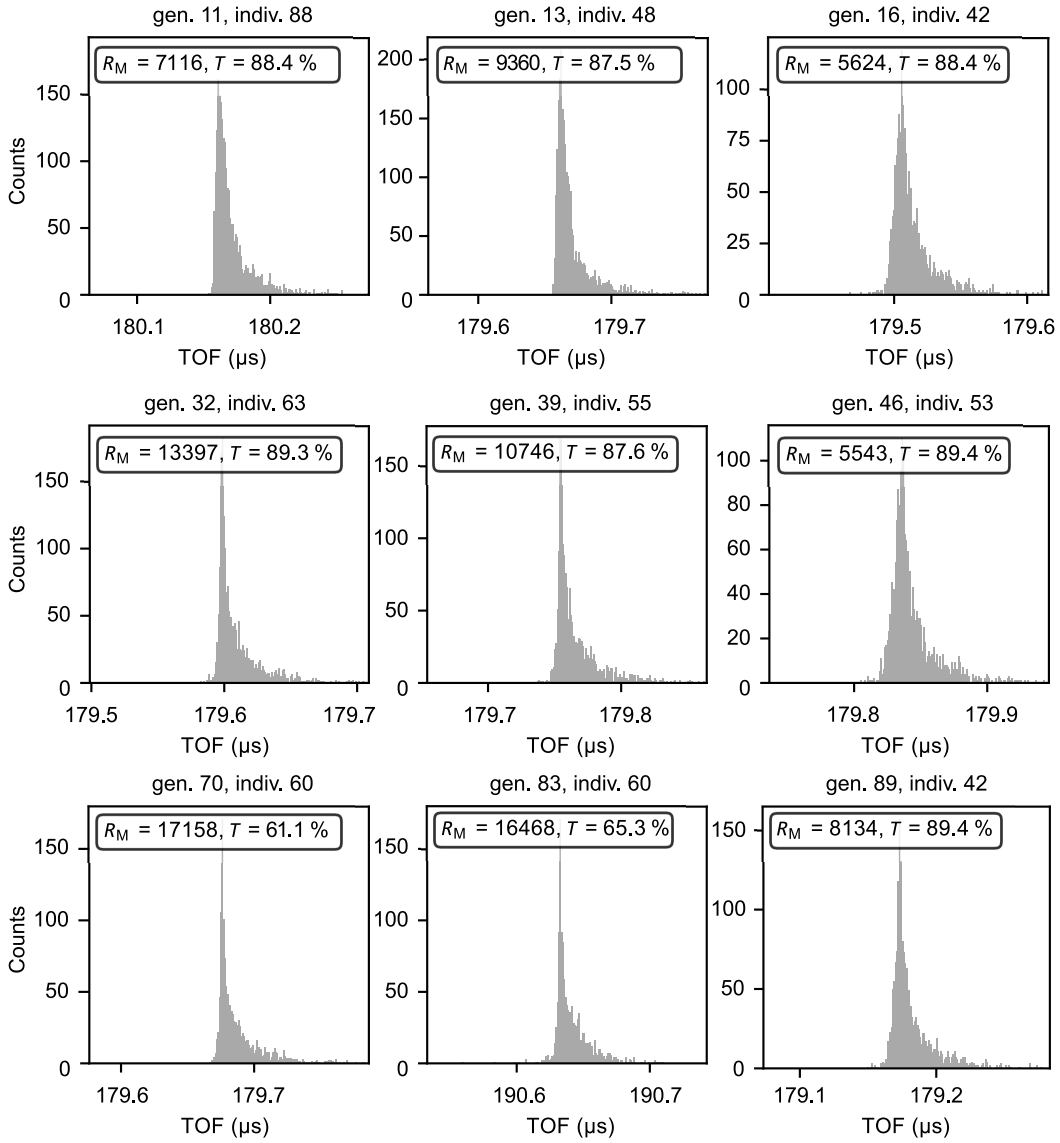

Figure 4.14: Performance evaluation for the nine cluster-representative individuals identified in the ROI of the Pareto plot for 50 performed full-turns in the mass analyzer. The performance was characterized in terms of the mass resolving power R_{M} (FWHM) and the particle transmission T. Both performance metrics could be enhanced in comparison to the initial mass analyzer design.

again by applying a different fraction of the electrode length and height as the starting point of the incision in each axis. The applied range for these fractions was set for the x-axis from 0.3 to 0.7 and for the y-axis from 0.5 to 0.9.

Table 4.2: Applied Latin hypercube parameter sampling ranges and fixed parameter values for subsequent simulation and sensitivity analysis.

	U (V)	l (mm)	d (mm)	r (mm)
Elec. 1	[-2620; -2520]	[12; 14]	3	[2; 4]
Elec. 2	[-4430; -4330]	[5; 7]	3	[2; 4]
Elec. 3	[-3950; -3850]	2	3	2.5
Elec. 4	[-460; 360]	2	3	2.5
Elec. 5	[1270; 1370]	2	[2; 4]	[2; 4]
Elec. 6	[1850; 1950]	2	[2; 4]	2.5
Elec. 7	[3000; 3100]	2	3	2.5

The sampled parameter configurations were simulated again with the same remaining settings as in the iso-mass MR evaluation in Section 4.2.1 but due to the high computational effort only for five full-turns. For each sampled and simulated parameter configuration, the mass resolving power R_{M} and the transmission T were calculated in the mass analyzer center after five full-turns and the effect of parameter value variation within the sampling ranges on R_{M} and T was evaluated by a DMIM sensitivity analysis, which delivered the sensitivity indices ST (total effect) and S1 (interaction with other parameters) as shown in Figure 4.15.

This analysis reveals that for the variation of electrode voltage values, the mass resolving power is mainly influenced by the electrodes 5 and 6, which form the field curvature around the reflection point of the ions. Electrode 7 has negligible influence on both R_{M} and T, which is in line with previous observations with the initial manual mirror design where the ion turn point was also located between electrodes 5 and 6. The potential applied to electrode 7 thus has minor impact on the ion trajectories. The transmission is mainly affected by the voltages of electrodes 1 and 2, which represent the lens part of the ion mirror.

The variation of geometrical parameters within the given sampling ranges showed low effect on R_{M} and T for the length and distance of the considered electrodes. However, varying the inner electrode radius affects the transmission behavior, as a smaller electrode radius causes particles to collide with the electrode. The variation of the conical incision of electrode 1 showed low effects on R_{M} and some minor impact on

the transmission by variation of the vertical cone dimension (y fraction).

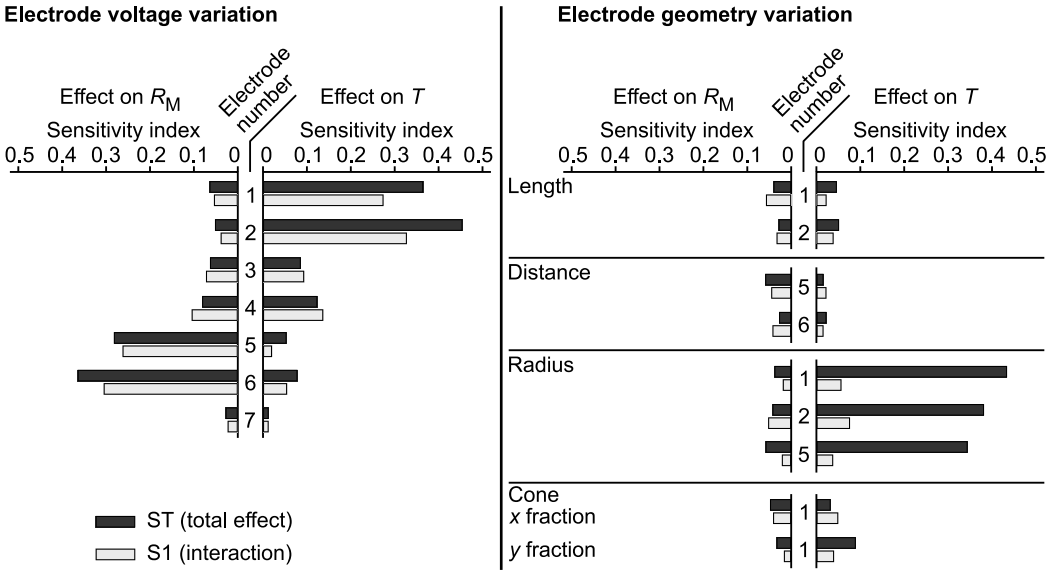

Figure 4.15: Sensitivity indices derived by DMIM for the LHS parameter configurations indicating the sensitivity of R_M and T on variation of the electrode voltage and geometric parameter values.

The optimization process resulted in geometric parameters similar to the initial ion mirror design. The sensitivity analysis showed that geometric variations had minimal impact on the system's output, leading to the retention of the initial geometric design for the mass analyzer. This configuration, along with suitable electrode voltage settings, ensures favorable output characteristics. The simple design, with constant electrode distances and identical shapes for electrodes 3 to 7, facilitates mechanical prototyping. The sensitivity analysis also highlighted the required manufacturing tolerances. While electrode 7 had negligible impact on output, it was kept in the design for maximum flexibility in shaping the mirror field.

Based on the values obtained for R_M and T for the LHS parameter configurations, the final voltage setting for the MR mode was determined, as shown together with the potential distribution and the obtained ion trajectories in Figure 4.16. The direct comparison of the LHS parameter sets with the performance achieved by the two previously identified cluster representatives from the optimization for the same number of five full-turns showed a slight increase in terms of R_M by up to 500 by the LHS sets and constant performance in terms of transmission. For the LHS parameter

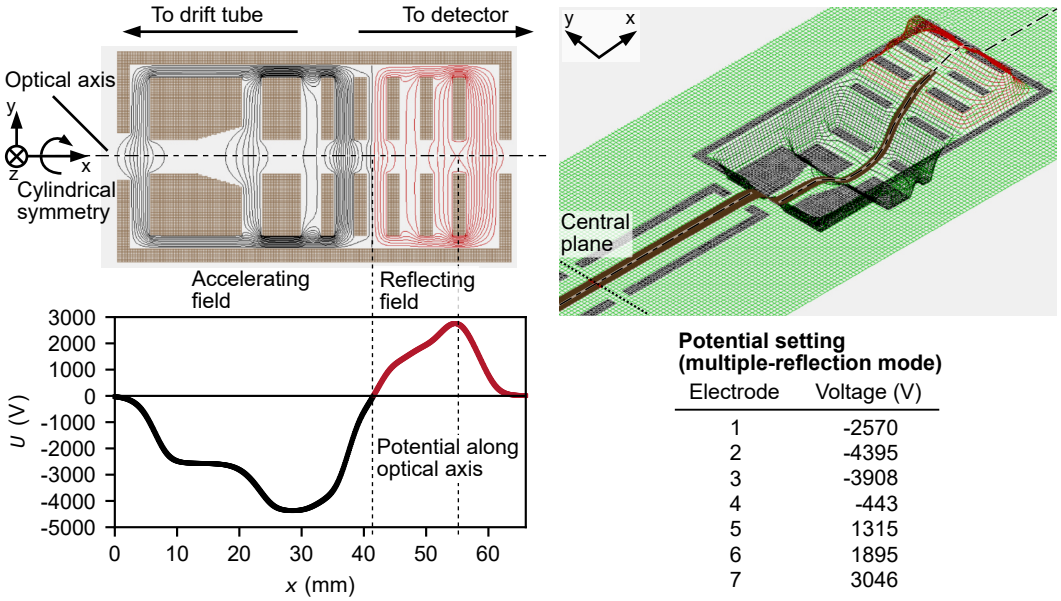

Potential setting (multiple-reflection mode)

Electrode	Voltage (V)
1	-2570
2	-4395
3	-3908
4	-443
5	1315
6	1895
7	3046

Figure 4.16: Potential distribution and particle trajectory in the ion mirror with the given optimized potential setting for the MR mode.

configurations with increased mass resolving power and constant transmission, the centroid was determined as described in Section 3.4.4, whereby only the voltage values were taken into account. This voltage setting was simulated again for verification and characterization with the finally selected geometric parameters. For this, the mass analyzer design was characterized in terms of R_{M} and T the same way as it was described earlier in Section 4.2.1. The obtained evolution of these performance indicators over the number of performed full-turns N is shown in Figure 4.17.

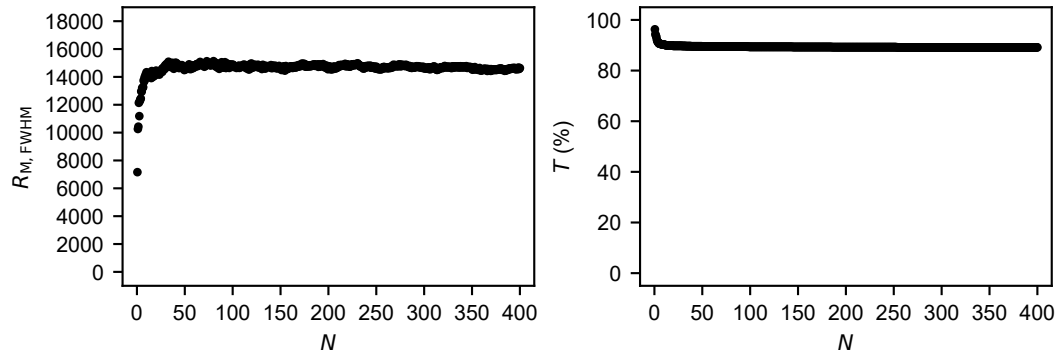

Figure 4.17: Characteristics of the full-turn dependent mass resolving power and transmission of the optimized mass analyzer in iso-mass operation in MR mode.

Compared to the initial mass analyzer design, the optimization significantly increased mass resolving power and improved transmission, demonstrating that the modified spatial focusing strategy enhances beam confinement.

4.3 Ion source and injection system

In time-resolved mass spectrometry, it is essential to have a well defined start time for the ion movement in order to precisely determine the total time of flight. This is achieved by the pulsed injection of the ions into the mass analyzer. Common methods for forming such pulsed ion bunches are described in Section 2.1.4. Within this thesis, the pulsed storage EI ion source [106] was considered for this purpose. This method is a promising concept to combine small geometrical dimensions with high sensitivity and possibly good duty cycle for the pulsed operation in TOF experiments. This section evaluates this technology with simulations for applicability in the MRTOF mass spectrometer. Further, a novel method is developed and evaluated for the formation of pulsed ion bunches, which overcomes some limitations of current injection systems applied in TOF mass spectrometers.

4.3.1 Electron impact storage ion source

Multiple criteria must be fulfilled for the pulsed ion source and injection system to satisfy the overall MRTOF instrument specifications, as listed in Section 4.1.1. Considering the potential particle losses in the mass analyzer while performing the full-turns, a high injected initial particle count is crucial, to allow high-sensitivity and reliable m/z measurements. Methods, which apply a pulsed ionization, allow only a low particle count. Furthermore, the restriction to mainly laser ionization reduces both the flexibility in terms of use cases and the compactness of the instrument. Approaches that rely on the formation of ion bunches through continuous beam modulation necessitate a trade-off between short ion pulses and the number of injected ions, making their use in MRTOF ineffective. The EI storage ion source, on the other hand, enables ion accumulation through continuous ionization and particle trapping until pulsed extraction, significantly enhancing sensitivity.
The mass resolving power in MRTOF mass analyzers for many performed full-turns is mainly defined by the achievable aberrational time spread per full-turn Δt_{FT}. In order to achieve low values for Δt_{FT}, not only a suitable design of the ion mirrors is required, but also small deviations of the initial properties of the injected ions from the reference value. The aim must therefore be to keep the distribution of particle properties as narrow as possible around the ideal reference value. In particular, the energy spread of the ions must be kept as low as possible during extraction from the source and acceleration of the particles, as the particle energy itself cannot be corrected. The deviation of the particle trajectories from the ideal trajectory along

the optical axis must also be kept to a minimum by using appropriate optics for beam confinement.
The initial temporal spread of the ion packet on the primary time focus plane is also a decisive criterion. However, for MRTOF measurements with many full-turns, less decisive than for linear TOF and single-reflection TOF measurements.
Lastly, in the pulsed extraction of particles, it is crucial that the usable mass range is kept as large as possible and that high extraction efficiencies are achieved over the entire mass range to achieve high sensitivity and duty cycle. The source and injection system also significantly determines the quality of the achievable spectrum in terms of background noise, which must be very low to ensure a high SNR and the reliable detection of very weak signals.

Design

To implement a pulsed ion storage source based on EI ionization for the MRTOF mass spectrometer to be developed, an existing rotationally symmetric and continuously emitting crossbeam Nier-type EI ion source was initially used as the design basis. By modifying certain electrodes, an alternating operation of the source was made possible, which allows both an accumulation of particles during a trapping phase and their rapid extraction from the ionization and trapping chamber during the extraction phase. The schematic structure of this modified ion source is shown in Figure 4.18.

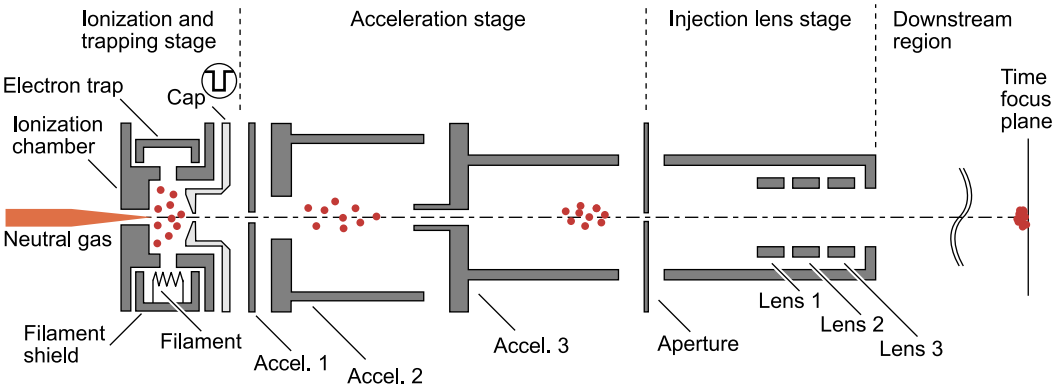

Figure 4.18: Structure of the modified EI to operate in a pulsed manner. The cap electrode can be switched independently to allow rapid voltage pulsing for the extraction of the previously trapped ions from the ionization chamber.

Neutral gas molecules are inserted through an opening in the ionization chamber and are ionized by a continuous electron beam crossing the ionization chamber from the filament towards the electron trap. The filament bias voltage is set 70 V below the ionization chamber potential, while the electron trap potential is 10 V above the chamber potential. The mean energy of the extracted ions is adjusted by the static potential difference of the ionization chamber to the ground. The electrodes within the acceleration and focusing stage are static. Between the cap electrode and accel. 1, between accel. 1 and accel. 2 and between accel. 2 and accel. 3 (always at ground), accelerating and focusing fields are formed. Ion bunches are thus compressed in their temporal and spatial dispersion by approaching the time focus plane. The position of the time focus plane is set by the potentials applied to accel. 1 and accel. 2. At the end of this acceleration and focusing stage there is placed an aperture to block particles with highly divergent trajectories. Subsequently, an injection lens stage was implemented, consisting of three identical ring electrodes forming an Einzel lens to enhance spatial beam focusing.

The key feature of this ion source is the electrically isolated cap electrode, which separates the ionization and trapping chamber from the acceleration and focusing stage, allowing it to be switched independently of the surrounding electrodes and potentials. By applying different potentials, particles can be trapped as well as quickly extracted from the chamber. This concept does not use grids and is based on the operation of existing systems [106, 138, 139]. The functionality was evaluated using simulation in SIMION for both the trapping phase and the ion extraction.

For all subsequent tests, the constant electrode potentials of the acceleration and focusing stage, as well as the injection lens stage, were set to position the primary time focus plane 142 mm behind the aperture of the acceleration stage, assuming a chamber potential of 1780 V and an applied extraction voltage gradient of 200 V. This corresponds to the position of the central plane of the developed mass analyzer when it is positioned directly after the injection lens stage. This plane acted as the measurement plane for the extracted particles in the subsequently described evaluations. The optimization framework was used to set the potentials of accel. 1, accel. 2 as well as lens 1, lens 2 and lens 3. The objectives of the optimization were a reduction of the time spread at the desired position of the time focus plane, as well as a reduction of the off-axis and angular distribution on the same plane. This meant that both the focusing in the time domain and in the spatial domain were taken into

account in the optimization. The voltage values of the electrodes mentioned were thus obtained as shown in Table 4.3.

Table 4.3: Identified voltage settings for the respective electrodes of the ion source and injection system to place the primary time focus 142 mm behind the aperture of the acceleration and focusing stage, which corresponds to the position of the mass analyzer central plane in the full instrument configuration.

	Accel. 1	Accel. 2	Lens 1	Lens 2	Lens 3
Voltage (V)	1426	1480	180	1036	0

Particle trapping and accumulation

During the trapping phase, a constant potential U_{chamber} is maintained within the ionization chamber, preventing the produced particles from immediately experiencing an accelerating force towards the cap. The created ions can distribute within the ionization chamber according to their initial velocity vectors. The space charge of the electron beam assists the trapping by compressing the ions to a dense volume [86, 106, 138]. The modified ion source also comprises a permanent magnet, which is intended to increase the ionization efficiency by forcing the electrons onto spiral trajectories, which increases the probability for collisions with neutral gas particles [140, 141]. The applied magnetic field can also contribute to the trapping of the particles. However, this study does not cover the beneficial effects of these methods. Instead, a worst-case scenario was assumed, where particles can freely distribute until they either collide with the chamber walls or exit the ionization chamber through the extraction aperture as leakage current. These two phenomena contribute to the overall ion loss rate R_{loss}. This overall loss rate equals zero at the beginning of the ionization process and gradually approaches the particle creation rate R_{creation} over time, until a balance between particle creation and loss is achieved. Thus, R_{loss} shows a time-dependent behavior. Due to the temporal delay in the equilibrium between R_{creation} and R_{loss}, particles can accumulate in the ionization chamber until the equilibrium between creation and loss rates is reached, significantly increasing the number of particles that can be effectively extracted. At the point of equilibrium, the maximum particle density within the ionization chamber is achieved. By quickly applying an extracting electric field at this moment, a significantly higher number of particles can be extracted compared to a continuous ion source.

For the simulations of the particle trapping, the potential of the ionization and trapping chamber U_{chamber} was set to 1780 V. Due to the mass dependence of ion mobility, the characterization was performed for different representative m/z ratios (2, 20, 50, 100, 500 amu/e). For each m/z, particles were generated at a constant generation rate ($R_{\text{creation}} = 10$ particles/ns) over a period of 50 µs by implementing a uniform distribution of the ion time-of-birth (TOB) in SIMION. Within the simulation, for the initial position of the ions, a Gaussian distribution was assumed along the optical axis (x-axis) with the mean set to the center of the ionization chamber and the FWHM set to 0.8 mm for a total lateral dimension of the ionization chamber in the x-direction between 2.6 mm and 4 mm. The distribution for the initial position along the z-axis was set with the same parameters as for the x-axis. For the initial position along the y-axis representing the direction of the electron beam, a uniform distribution ranging from −1 mm to 1 mm of the center of the ionization chamber was applied. The initial thermal motion of the ions was considered by applying a Maxwell energy distribution for a temperature $T = 598$ K. In the simulation, the cumulative number of lost particles (those no longer available in the ionization chamber) was determined at discrete time intervals. The rate of particle creation or loss is given by

$$R = \frac{dN}{dt} \tag{4.4}$$

where dN is the number of created or lost particles, and dt is the time interval considered. The time derivative of the smoothed temporal distribution of lost particles thus yields the loss rate of the particles over time. For better comparability, this loss rate was normalized according to

$$R_{\text{loss, normalized}} = \frac{R_{\text{loss}}}{R_{\text{creation}}} \tag{4.5}$$

as shown in Figure 4.19 (a).

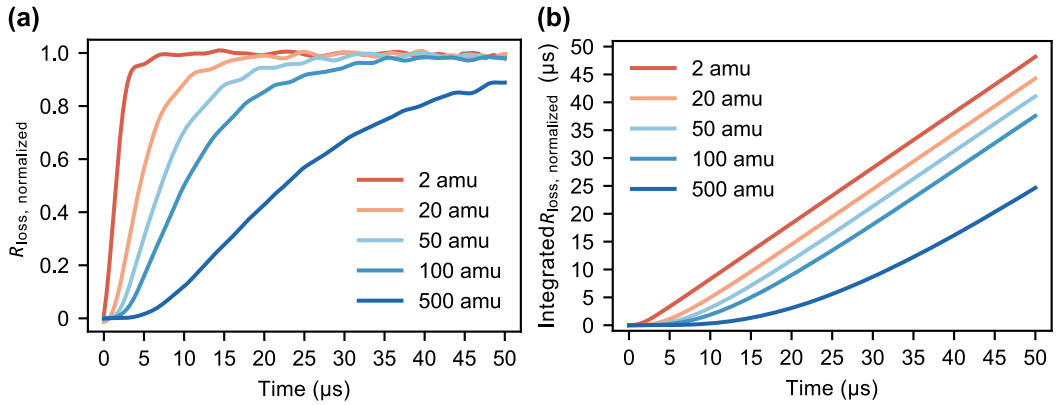

Figure 4.19: (a) Normalized total particle loss rate in the ionization and trapping chamber over time. Low mass ions need less time to reach the equilibrium ($R_{\text{loss, normalized}} = 1$) of particle creation and loss due to their higher mobility compared to high mass particles. (b) Cumulative integral of $R_{\text{loss, normalized}}$ over time to be used with Equation 4.7 to calculate for a given R_{creation} the total number of trapped particles within the ionization and trapping chamber.

The equilibrium between ion loss and creation rates is reached at values of 1. For lower masses, this equilibrium is achieved significantly earlier. Due to the higher mobility of lighter ions, they collide with the chamber walls more quickly after ionization, and the probability of prematurely leaving the chamber as leakage current through the extraction aperture is increased compared to heavier particles. To deduce the number of particles contained in the chamber as a function of the ionization rate, the following relationship can be used:

$$N_{\text{trapped}}(t) = \int_0^t R_{\text{creation}} dt - \int_0^t R_{\text{loss}} dt \tag{4.6}$$

Assuming a constant ion creation rate, this term simplifies to:

$$N_{\text{trapped}}(t) = R_{\text{creation}} \cdot \left(t - \int_0^t R_{\text{loss,normalized}} dt \right) \tag{4.7}$$

Given the known particle creation rate, integrating the normalized loss rate, as shown in Figure 4.19 (b), allows for the calculation of the absolute number of particles contained in the chamber at any given time.

The trapping behavior of the particles is also characterized by the decay of the accumulated particle volume in the chamber after the particle generation has ceased. For this purpose, the continuous particle generation was abruptly stopped after some time, the chamber potential was maintained at the trapping level, and the cumulative

number of lost particles was recorded at discrete time intervals. The temporal progression of the trapping efficiency, as depicted in Figure 4.20, was determined using the following equation:

$$\eta_{\text{trapping}} = \left(1 - \frac{N_{\text{lost, cumulative}}}{N_{\text{trapped, max}}}\right) \cdot 100\% \tag{4.8}$$

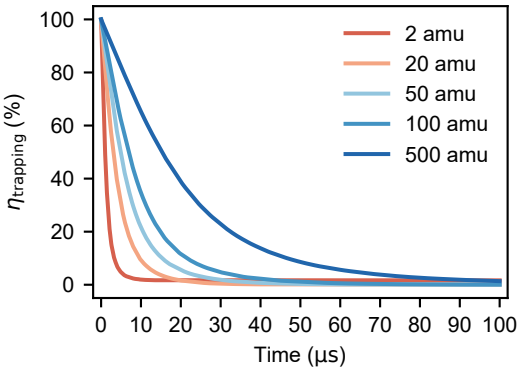

Figure 4.20: Temporal evolution of the trapping efficiency η_{trapping} in the trapping chamber after abruptly switching off the ion creation and maintaining the trapping potentials in the chamber. The ion creation cut-off corresponds here to $t = 0\,\mu s$. Fast ions are lost faster due to collisions with the chamber walls and leakage through the extraction aperture caused by the high mobility.

It is also evident that particles with higher mass leave the chamber more slowly due to their lower mobility. Consequently, a high trapping efficiency is maintained in the chamber for a longer period after the cessation of particle generation.

These tests have shown that the present design basically enables the accumulation and retention of particles in the ionization chamber. Especially for particles with high m/z a high degree of accumulation can be achieved due to the low ion mobility.

Evaluation of the state-of-the-art extraction method

Besides the trapping capabilities of the given design, also the extraction of particles was characterized by simulations in SIMION. The suitability of the state-of-the-art extraction method for this type of ion source was thereby determined for the formation of pulsed ion packets in TOF and MRTOF in particular. The pulsed extraction of particles is achieved by rapidly switching the cap electrode from the trapping potential to the extraction potential and back to the trapping potential. The main parameters

of this process are the applied potential difference between the trapping and the extraction $U_{\text{extraction}}$ and the duration of the extraction pulse $t_{\text{extraction}}$. The effect of these parameters on the performance characteristics was evaluated using series of measurements. For all tests, a constant rise and fall time of 50 ns was used to reach the maximum voltage difference. The extraction time $t_{\text{extraction}}$, defined as the dwell time at the lower extraction potential relative to the higher trapping potential, was varied (800 ns, 1000 ns, 1200 ns). For $U_{\text{extraction}}$, the value was varied between 100 V, 200 V, 300 V and 400 V. The measurements were performed for m/z at 50 amu/e and the remaining electrode voltages were kept as in the previous simulations to evaluate the trapping behavior. For each configuration of these parameters, the FW50 time spread and the FW50 energy spread of the impinging ion packet were recorded on the same measurement plane located 142 mm behind the aperture of the acceleration stage. The results are shown in Figure 4.21.

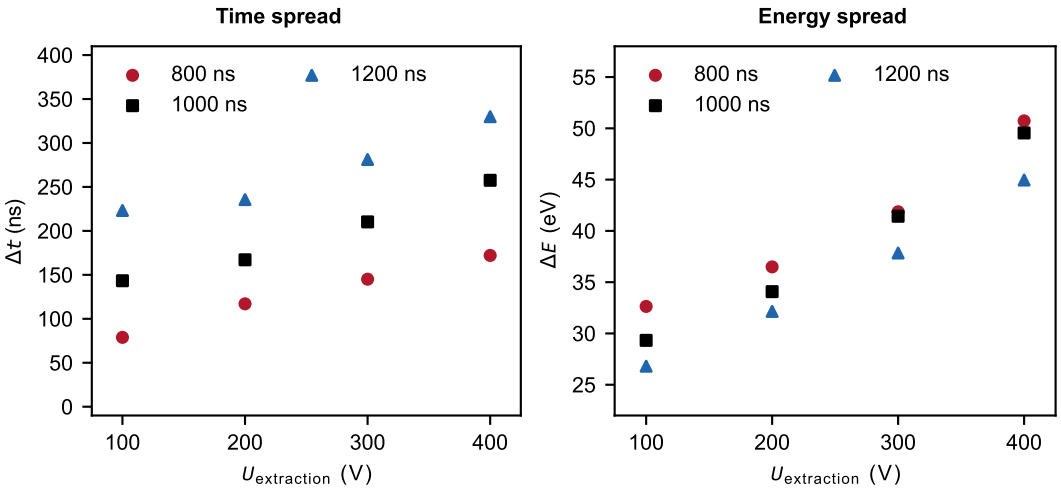

Figure 4.21: Timespread Δt and energy spread ΔE of the extracted particles recorded at the primary time focus plane. Both Δt and ΔE show linear dependence on the extraction voltage $U_{\text{extraction}}$. The duration of the extraction pulse $t_{\text{extraction}}$ influences Δt by the flight time incertitude Δt_{TOB} of continuously created ions starting their motion during the extraction phase.

These results show that both the time spread and the energy spread of the particles in the parameter space under consideration increase linearly with $U_{\text{extraction}}$. The duration of the extraction pulse $t_{\text{extraction}}$ also influences both the time spread and the energy spread. Shorter $t_{\text{extraction}}$ shows increased ΔE. Particles generated during the extraction phase are extracted directly. Unlike the particles generated during the trapping phase, these ions cannot spread spatially in the ionization chamber,

but have only a very small spatial distribution in the x-axis. This means that the initial energy spread of these particles is lower than that of the trapped particles. An extended extraction phase thus increases the proportion of ions with a narrow energy distribution, thereby reducing the total FW50 ΔE. Longer pulses also lead to a higher time spread, which is directly attributable to the contribution to the total TOF error due to the different start times Δt_{TOB} of the continuously generated ions during the extraction pulse. This can also be seen in Figure 4.22, which shows the TOF peaks on the primary time focus plane for different applied values of $t_{\mathrm{extraction}}$. These measurements were all applied with 200 V for $U_{\mathrm{extraction}}$ and m/z of 50 amu/e.

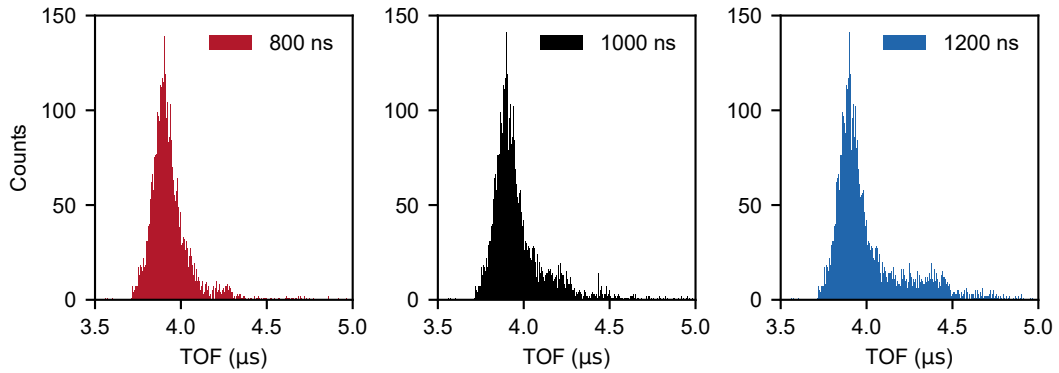

Figure 4.22: Comparison of ion TOF peaks for m/z at 50 amu/e, recorded at the primary time focus plane, with different applied duration of the extraction pulse $t_{\mathrm{extraction}}$ (800 ns, 1000 ns, 1200 ns). The applied extraction voltage gradient $U_{\mathrm{extraction}}$ for all measurements was 200 V. Longer $t_{\mathrm{extraction}}$ leads to broader peaks and significant formation of a peak tail due to the flight time error contributions Δt_{TOB} by the different motion starting times of continuously created ions during the extraction.

Thereby, the effect of $t_{\mathrm{extraction}}$ on the peak shape can clearly be depicted. Longer extraction times lead to a an enhanced tail of the peak, which ultimately produces background noise. This tail is caused by the fact, that ions, which are first created during the extraction phase have different TOB and thus different starting times for their motion. Hence, these different starting times for the ion motion create a TOF error Δt_{TOB}, which broadens the temporal peak. As stored ions in the chamber, which were effectively created before the application of the extraction pulse, are accelerated and reaching the detector first, the rising edge of the peak is relatively sharp in all configurations. However, even after the majority of these stored ions has already left the ionization chamber, the ions continuously created during the extraction phase can still be accelerated towards the downstream region until the

cap electrode is switched back to the trapping state, such that they will cause the delayed TOF signals forming the tails of the peaks.

Considering these effects, a pulsed operation of the ion source with low $U_{\text{extraction}}$ and $t_{\text{extraction}}$ is desirable to reach single-mass peaks with low temporal spread and low spectral background noise. For low energy spread, also a low $U_{\text{extraction}}$ but longer $t_{\text{extraction}}$ is desirable with this operation principle. However, the extraction of ions of different masses is also dependent on the parameters $U_{\text{extraction}}$ and $t_{\text{extraction}}$ and was thus evaluated in terms of the temporal evolution of the trapping efficiency $\eta_{\text{extraction}}$. For this, ions of different m/z (2, 20, 50, 100 and 500 amu/e) were created and stored in the ionization chamber for 5 µs until they were extracted by applying a lower potential to the cap electrode. To ensure that the extraction process is free from parasitic effects caused by continuously generated ions during the extraction phase, the generation of new ions was switched off at the start of the extraction pulse in the simulation, allowing only the behavior of the trapped particles to be recorded. The measurements were carried out for two different $U_{\text{extraction}}$ (100 V and 400 V). The cap electrode was kept permanently at the lower extraction potential. At the beginning of the extraction pulse, the number of ions contained in the chamber $N_{\text{trapped, max}}$ was recorded and the cumulative number of extracted particles $N_{\text{extracted, cumulative}}$ was continuously recorded directly at the cap electrode. The extraction efficiency can therefore be determined similarly as the trapping efficiency using

$$\eta_{\text{extraction}} = \frac{N_{\text{extracted, cumulative}}}{N_{\text{trapped, max}}} \tag{4.9}$$

The results of this test series are shown in Figure 4.23.

It can be seen that particles with a higher mass are extracted much more slowly than particles with a lower mass. This is consistent with the observations on trapping behavior. The comparison of the two applied values for $U_{\text{extraction}}$ shows that the higher voltage accelerates the extraction process. Consequently, to extract particles within a specific mass range during a defined $t_{\text{extraction}}$, $U_{\text{extraction}}$ may need to be increased, which in turn results in a significant time and energy spread.

These characteristics show that the desired behavior of the ion source for use in TOF and MRTOF in particular is not fulfilled in all points and that a trade-off must always be made when selecting the parameters and the achievable performance. In reported setups [106, 138], extraction times of more than 1 µs are typically chosen

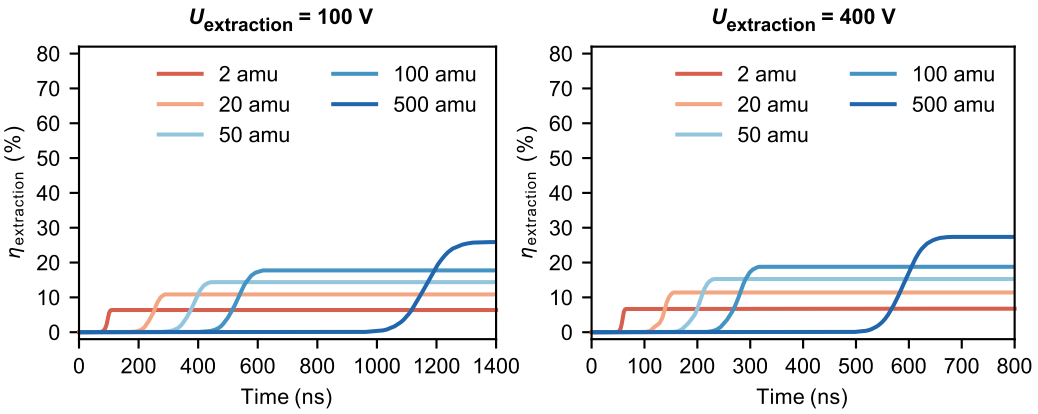

Figure 4.23: Temporal evolution of the extraction efficiency for different masses and two different applied extraction voltages (100 V and 400 V). Particles with higher mass require more time to be fully extracted. By applying a higher extraction voltage gradient, the required time for extraction of a given mass range can be reduced.

for $t_{\text{extraction}}$ to ensure sufficient extraction efficiency across a wide mass range. At the same time, extraction voltages of at least 200 V to more than 400 V are usually selected. This inevitably leads to considerable background noise from continuously generated ions during the extraction phase, with the ions exhibiting a strong energy spread. The background noise limits the SNR considerably. Although the background noise can be reduced by post-acquisition spectrum data treatment, very weak peaks are always lost in the noise and cannot be detected. For linear TOF and reflectron TOF, the initial time spread on the primary time focus plane is particularly decisive for the achievable mass resolving power, while for MRTOF the energy spread is more relevant, as this significantly influences the aberrational time spread per full-turn Δt_{FT}, which ultimately determines the maximum achievable resolution. This leads to the conclusion, that the conventional pulsed storage EI ion source may provide reasonable performance for linear and reflectron TOF setups but not for operation in MRTOF instruments. Therefore, an improved solution must be developed.

4.3.2 Refined electron impact storage ion source

Due to the given limitations of the conventional storage EI ion source for injecting pulsed ion bunches, a novel methodology was developed to establish optimized starting conditions for MRTOF experiments. The requirements for the ion source described at the beginning should be fulfilled as far as possible. In particular, the problem of background noise should be addressed to allow measurements with increased SNR.

Design and operation concept

The evaluation of the operating concept of the conventional storage EI ion source has shown that the continuously generated ions during the extraction phase in particular have a decisive influence on the achievable performance in terms of Δt, ΔE and the background noise. To achieve a clean spectrum with minimal or ideally no background noise, the contribution of continuously generated ions during the extraction phase must be eliminated. This also allows a significant reduction of Δt due to the elimination of the initial TOF error Δt_{TOB}. By eliminating these continuously generated particles, the energy spread becomes independent of $t_{\mathrm{extraction}}$. To achieve a low energy spread, $U_{\mathrm{extraction}}$ must be kept low. The problem of a low extractable mass range is then circumvented by increasing $t_{\mathrm{extraction}}$, which in turn does not have a negative effect on the remaining characteristics due to the suppressed contribution of continuously generated ions. To allow such an operation concept from a technological perspective, the continuous generation of ions during the extraction phase must be blocked. A simple and stable approach is to maintain the extraction of electrons from the filament but to cut off the electron beam entering the ionization chamber such that no further ionization due to EI can take place. This cut-off must then be synchronized with the extraction pulse applied to the cap electrode. In the given design of the ion source, the electron beam cut-off was implemented by applying a higher potential to the filament shield than to the ionization chamber to reverse the direction of electron movement away from the ionization chamber. This novel operation concept is schematically shown in Figure 4.24.

To allow this operation, within the ionization and trapping stage, the filament is electrically isolated from the filament shield and the cap electrode with the extraction aperture. This allows to independently apply different pulsed potentials to these electrodes. During the trapping phase the potential of the cap electrode U_{cap} is kept at U_{chamber} such that no electric field can accelerate the generated particles. The potential of the filament U_{filament} is kept around 70 V below U_{chamber}. Electrons emitted from the filament are thus accelerated with sufficient energy towards the ionization chamber such that electron impact ionization can occur. At the time of particle extraction, U_{cap} is lowered by the extraction voltage $U_{\mathrm{extraction}}$ below U_{chamber} to establish a moderate accelerating field within the ionization chamber. At the same time, the potential of the filament shield $U_{\mathrm{filS.}}$ is increased from $U_{\mathrm{filS.1}}$ well above U_{chamber} to $U_{\mathrm{filS.2}}$ while U_{filament} stays at its original potential. Electrons emitted from the filament are thus much more likely accelerated towards the filament shield than towards the ionization chamber such that the ionization rate is effectively reduced

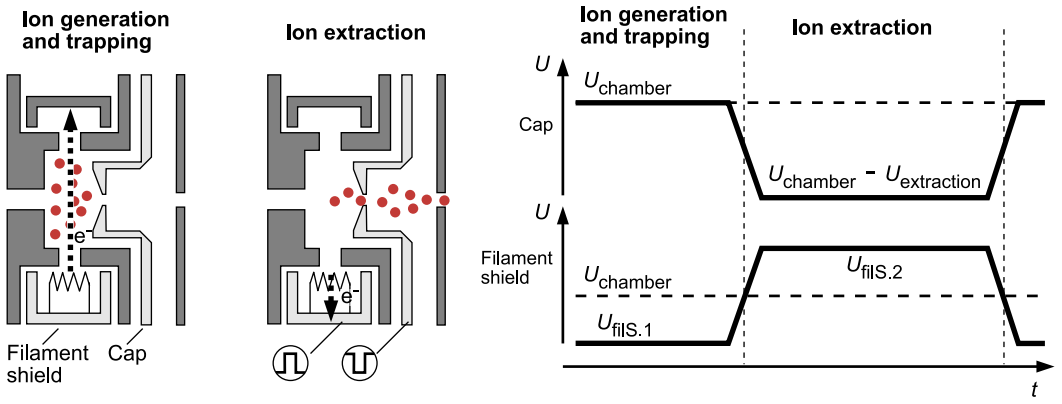

Figure 4.24: Electrode configuration and operation principle of the refined EI storage ion source. The continuous ionization during the trapping phase foresees to keep the filament shield potential $U_{\mathrm{filS.1}}$ below the potential of the ionization chamber and the cap electrode. For the pulsed particle extraction, an accelerating electric field is applied in the ionization chamber by lowering the cap potential from U_{chamber} by $U_{\mathrm{extraction}}$. At the same time, the potential of the filament shield is increased from $U_{\mathrm{filS.1}}$ to $U_{\mathrm{filS.2}}$, which accelerates the electrons towards the filament shield instead of towards the ionization chamber. After the desired extraction time, the potentials of the cap and the filament shield are switched back to the trapping configuration.

to a minimum. Particles contained in the ionization chamber can now leave the chamber to the downstream region. The duration of this extraction process depends on m/z. Therefore, the minimum pulse duration has to be set in accordance with the extraction time of the highest mass of interest. Once, all the desired particles are extracted, the cap electrode switches back to U_{chamber} to stop particle extraction and the filament shield electrode is again set to $U_{\mathrm{filS.1}}$ to allow electron acceleration towards the ionization chamber and continuous ionization until the next extraction pulse is applied.

Pulsed particle extraction

The pulsed extraction of the particles after the initial trapping phase is carried out as described in Section 4.3.2. The extraction of the particles was again modeled using the SIMION simulation environment. The simulation conditions and constant electrode voltages for these tests have been chosen to be in line with the previous simulations for the trapping behavior and the conventional extraction method. The applied extraction voltage gradient $U_{\mathrm{extraction}}$ at the cap electrode was varied in a given voltage range from 20 V to 120 V, being significantly lower than in the test

series for the conventional extraction method. The resulting time spread Δt, the energy spread ΔE and the extraction efficiency $\eta_{\text{extraction}}$ were measured at the same measurement plane, located 142 mm behind the aperture, as applied for the conventional extraction method. The observations, made for the time spread, are shown in Figure 4.25. Particles with higher mass have in general higher time spread, which is caused by the mass-dependency of the ion mobility and the resulting time spread contribution of the turn-around time Δt_{TA}. For very low $U_{\text{extraction}}$, there is a high time spread, as the particles do not experience a sufficient acceleration and the turn-around contribution Δt_{TA} is still high. For $U_{\text{extraction}}$ at around 45 V, a minimum for the time spread is reached for all observed masses. When increasing the voltage after this optimal voltage setting, the time spread at the measurement plane also increases. This increase of the time spread is due to the fact that stronger extraction fields cause a higher energy spread of the particles, as shown in Figure 4.26. This, in turn, finally leads to higher time spread at the time focus plane due to imperfect focusing. The energy spread increases thereby linearly with $U_{\text{extraction}}$. This aligns with the previously described assumptions about the dependency of the particle energy spread on the extraction field strength. The simulation also reveals, that particles with higher mass have a lower energy spread. As the trapping time for this simulation was kept short, to maintain high computational efficiency, particles of higher m/z and low mobility, such as 500 amu/e, have not distributed over the full volume of the trapping chamber when the extraction field was applied, such that the energy spread is effectively reduced by the lower lateral expansion of the trapped ion volume. However, with longer trapping times, the behavior between the individual masses becomes more equal. The minimum time spread at $U_{\text{extraction}}$ around 45 V can be explained by the fact that the extraction field is strong enough to keep Δt_{TA} low, while the energy spread remains low as well. With respect to the time and energy spread, this setting represents a good candidate.

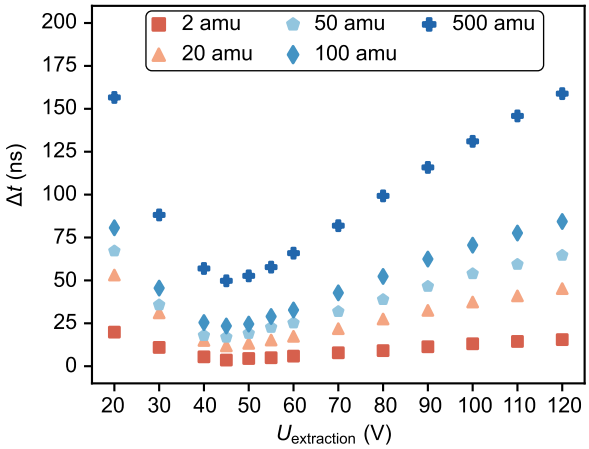

Figure 4.25: FW50 time spread of the extracted ions recorded at the measurement plane. The minimum time spread at $U_{\text{extraction}} = 45\,\text{V}$ is reached by low contributions of Δt_{TA} and Δt_{energy}.

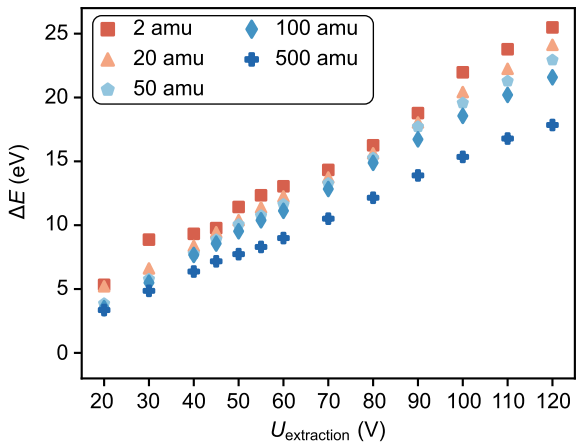

Figure 4.26: FW50 energy spread of the extracted ions recorded at the measurement plane. Higher applied voltage gradients during the extraction lead to higher spread of the particle energy.

However, the evaluation of the obtained extraction efficiencies for different $U_{\text{extraction}}$, as shown in Figure 4.27, reveals that in this voltage range still only a low fraction of the trapped ions is effectively extracted. Stronger extraction voltages show an increased extraction efficiency and a maximum can be reached for all observed masses at around 100 V. A trade-off is thus required between low time and energy spread and high extraction efficiency. For subsequent studies, $U_{\text{extraction}}$ was set to 60 V,

which enabled energy spreads for all considered masses below 15 eV, a time spread for m/z of 50 amu/e around 30 ns and an extraction efficiency of 7 %.

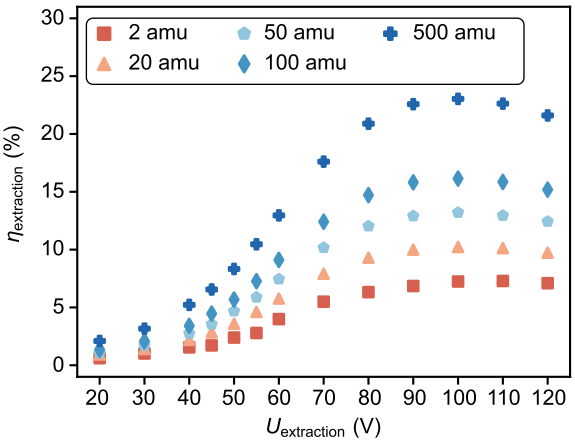

Figure 4.27: Ion extraction efficiency recorded at the measurement plane. A maximum can be reached for all masses at $U_{\text{extraction}} = 100\,\text{V}$.

To directly compare the effects of the novel and the conventional ion extraction method, the TOF spectrum for air as a representative gas mixture, was recorded for both methods on the primary time focus plane, as shown in Figure 4.28. To model the ion generation in SIMION, the generation rates were set according to the typical relative abundances of the m/z ratios contained in air. The ionization and accumulation of the particles took place over a period of 5 µs. For both methods, the particles were then accelerated towards the primary time focus plane by applying $U_{\text{extraction}} = 60\,\text{V}$. The primary time focus is suitable as the measurement plane for direct comparison of the spectra, as the flight time is largely independent of the energy distribution of the particles at this point. The voltages applied to all electrodes were identical to the previously described measurements for both methods. For the conventional extraction method, continuous ongoing ionization was assumed during extraction. The cap electrode was pulsed by decreasing the potential by the extraction voltage with an assumed rise and fall time of 50 ns each and a static duration at the extraction potential of 1750 ns. This extraction pulse width was chosen because it allows the extraction of the mass range for m/z from 1 amu/e to 500 amu/e at given voltage values and thus covers the common spectra. For the novel operation method the continuous creation of ions was switched off at $t = 5\,\mu\text{s}$ when the extraction pulse was applied. The rise time for the extraction pulse was also set to 50 ns, however there was not applied a back switching of the cap electrode to the

trapping potential, instead it was kept at the extraction potential. The comparison of the obtained spectra in Figure 4.28 reveals that there is an intensive spectral baseline for the conventional operation method (a). This baseline is caused by the continuously generated particles during the extraction phase and overlaps with the actual spectrum from the trapped ions leading to noise in the signal. It can be seen that this baseline increases up to a certain level with increasing time in the recorded spectrum, which is due to the mass-dependent mobility of the continuously generated ions. Light and fast ions with high mobility thus contribute to the baseline relatively early on, while heavy and slow ions with low mobility only become visible after a delay. In the air spectrum shown, the relatively weak peaks for m/z at 40 amu/e and 44 amu/e are completely overlaid by the baseline noise. The spectrum obtained with the novel extraction method (b) reveals that there is no such baseline, as only particles created during the trapping phase contribute to the spectrum. The weak peaks for m/z at 40 amu/e and 44 amu/e are thus still distinguishable. The novel extraction method allows an improved SNR for the recorded spectrum and thus increased dynamic range.

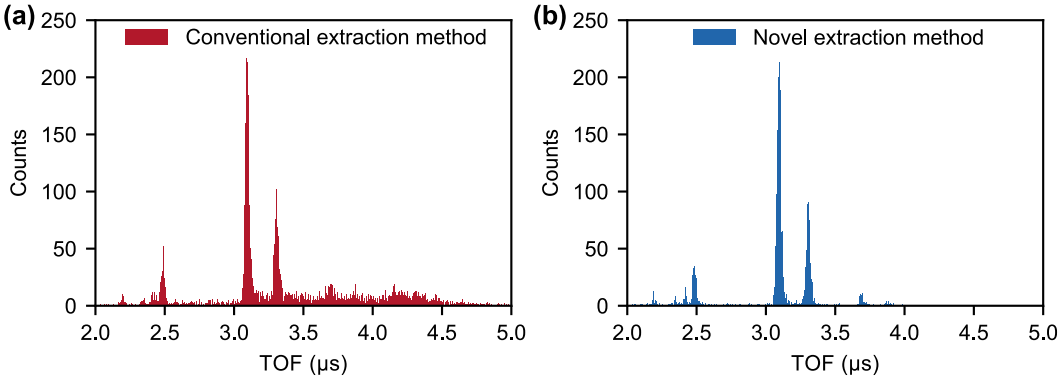

Figure 4.28: Comparison of the simulation TOF spectra for air recorded at the measurement plane for (a) the conventional extraction method and (b) the novel extraction method. The conventional extraction method involved an ongoing continuous ion generation during the extraction phase and a back switching of the cap potential to the trapping potential after 1750 ns. For the novel extraction method, the ion generation was switched off during the extraction phase and the cap electrode was kept at the extraction potential. The noise, caused by particles being generated and extracted during the extraction phase, limits the signal to noise ratio and thus the dynamic range and sensitivity for the conventional extraction method. The novel extraction method eliminates this noise and allows high SNR and improved dynamic range.

4.4 Complete mass spectrometer

The developed ion source, injection optics, and mass analyzer were initially considered separately. The overall system was then simulated to coordinate these components, verify the functionality of the MRTOF mass spectrometer, and evaluate its performance. In particular, the final geometric dimensions of the system components were used to adjust the focusing in both the time and spatial domains, in accordance with the instrument's operating concept. The tuning of electrode voltages, necessary for the potential settings in the different operating modes, was performed using the CPOpt framework. The simulations and evaluations conducted are described below.

4.4.1 Linear time-of-flight analysis

As described earlier, the design of the mass spectrometer also allows the operation as a linear TOF by setting all electrodes of the ion mirrors to ground potential and thus allowing ion transmission. The mass analyzer then acts as a field-free drift tube. As the linear TOF represents an open-path configuration, the unambiguous mass range is not restricted. However, the lack of additional flight time compensation of energy-distributed particles by an ion mirror as well as the limited total flight time do not allow high mass resolving power for this configuration.

To keep $\Delta t_{\mathrm{total}}$ small and finally obtain the best R_{M}, the primary time focus must be placed on the detector by the source and injection system. For this purpose, the source and injection system was optimized with the CPOpt framework to shift the time focus to the final detector position. The objectives are defined by a minimized FW50 time spread and an increased FW50 beam diameter, both measured on the detector plane. The second objective aims to maximize the used fraction of the MCP surface to reduce detector saturation. The optimization involved the tuning of the voltages for the source acceleration electrodes, the injection lens electrodes. Finally, suitable potentials for the respective electrodes were determined by the optimization and post-optimization data analysis process, as listed in Table 4.4

Table 4.4: Identified voltage settings for the respective electrodes of the ion source and injection system for the operation of the mass spectrometer in the linear TOF mode. All electrodes of the mass analyzer are set to ground potential for transmitting the ions.

	Accel. 1	Accel. 2	Lens 1	Lens 2	Lens 3
Voltage (V)	1320	1330	258	647	0

The performance of the mass spectrometer in the linear TOF mode was evaluated for the given voltage settings in the simulation. For this, the source was operated with a continuous ion creation ($R_{\text{creation}} = 10\,\text{particles/ns}$) during the retention phase for a duration of 5 µs and a subsequent pulsed release with the described novel extraction method. For this evaluation, an iso-mass measurement was performed with m/z of 40 amu/e and the particles were recorded on the detector plane. The acquired time-resolved mass peak is shown in Figure 4.29 (a). A mass resolving power (FWHM) of 95 with a time spread Δt (FWHM) of 27 ns and an ion transmission T of 90 % ($T = N_{\text{recorded}}/N_{\text{injected}}$) was measured. This indicates reasonable results, however higher R_{M} is desirable. In this configuration the recorded peak width is solely caused by contributions from the ion source. The recorded spatial beam profile on the detector plane in Figure 4.29 (b) reveals that the particles are evenly distributed over the impingement area with an overall maximum spot width of 5 mm, thereby covering 7.8 % of the available active MCP surface. A larger spot size is physically not reachable in the current configuration, due to the given inner diameters of the mirror electrodes.

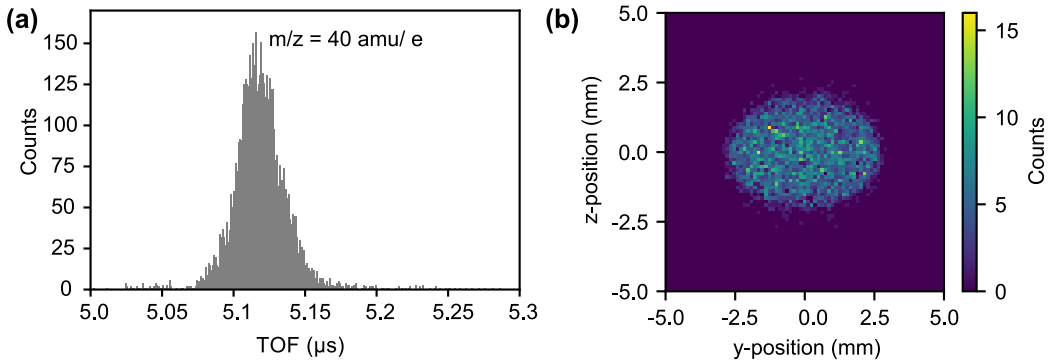

Figure 4.29: (a) TOF spectrum for an iso-mass peak (40 amu/e), recorded at the detector plane for the operation in linear TOF mode. (b) Spatial beam profile on the detector plane for the impinging particles.

The linear TOF mode was also evaluated for a measurement with multiple contained masses. For this, again the representative air sample from Section 4.3.2 was applied. The other simulation settings remained unchanged to the iso-mass measurement. The recorded TOF spectrum was converted to a mass spectrum based on Equation 2.8, which is shown in Figure 4.30. All contained mass peaks can be distinguished from each other, except the peak for m/z of 29 amu/e , which provides only very low signal and gets lost in the base of the major peak for 28 amu/e.

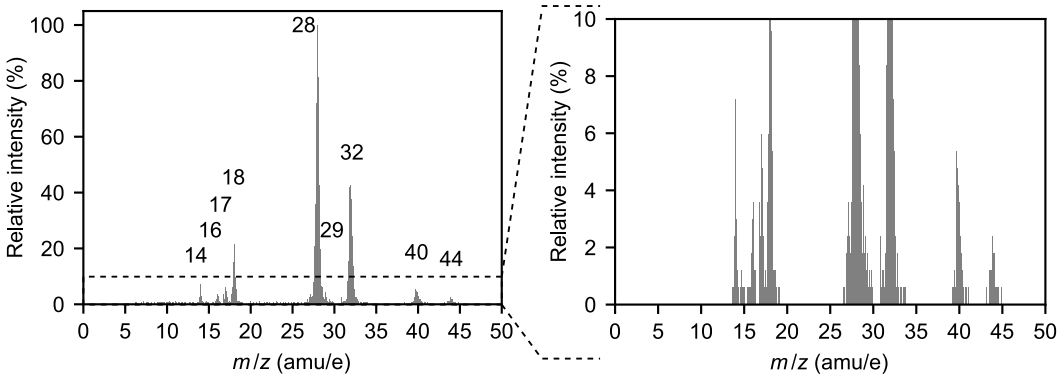

Figure 4.30: Mass spectrum of an air sample recorded at the detector plane in the linear TOF setup. The m/z ratios of the contained peaks are indicated.

Further enhancement of the performance is hardly doable, as the drift length and thus the total TOF of the ions is fixed by the total length of the instrument. A further reduction of the aberrational time spread can eventually be reached by further optimization of the ion source acceleration stage.

4.4.2 Multiple-reflection time-of-flight analysis

Injection mode

This operating mode for the mass analyzer is designed to introduce the ions in the mass analyzer and shift the time focus from the primary time focus plane, which is given by the source and injection optics, to the central plane of the MR cell. It is assumed that the primary time focus plane lies between the injection optics and the central plane of the MR cell. To introduce the ions into the mass analyzer in this mode, the potentials of the entry mirror are at a pass-through potential (ground). In the exit mirror, a dedicated potential setting is applied to shift the time focus.

To implement this operating mode in the developed mass spectrometer, the ion source and injection optics were initially set to achieve a primary time focus at a short distance from the injection optics. A shorter focus distance tends to result in smaller initial time spreads on the primary time focus plane. For this purpose, the ion source and injection system were tuned with CPOpt to achieve a minimum time spread on the entry plane of the entry mirror facing the source, located 43 mm behind the aperture of the source acceleration stage. For this optimization, an extraction voltage of 60 V was applied. At the same time, the aim was to minimize the deviations for the off-axis trajectory and the angular divergence on the central plane of the MR cell, taking into account the particle transmission through the ion source. With this objective, which is processed in the fitness function, the potentials at the electrodes accel. 1, accel. 2, as well as lens 1, lens 2 and lens 3 were optimized again. The most suitable potential setting resulting from this optimization is shown in Table 4.5.

Table 4.5: Potential setting for the respective electrodes of the source and injection system to set the primary time focus plane in short distance.

	Accel. 1	Accel. 2	Lens 1	Lens 2	Lens 3
Voltage (V)	1300	1320	150	900	0

With this setting, a FWHM time spread of 18.55 ns was achieved on the desired primary time focus plane for an iso-mass peak at $m/z = 40$ amu/e and the novel operation principle of the source with trapping for 5 µs before the pulsed extraction. With this configuration for the source, 72 % of all the extracted particles could effectively be introduced into the mass analyzer. The properties of the particle beam in terms of energy, off-axis distribution and angular spread were recorded on the central plane of the MR cell and are shown below.

The following optimization of the exit mirror is based on the position of the primary time focus plane as an object plane. The optimization was carried out largely analogously to that of the mass analyzer for the MR mode. However, only the electrode voltages were varied. In addition, the initial position of the particles was placed on the new primary time focus plane at the entrance of the entry mirror and only a reflection at the exit mirror was performed and the particle properties for the calculation of the fitness scores on the central plane were recorded after this injection TFS. The fitness function was identical to that for the MR mode. This optimization

ultimately provided a suitable voltage configuration for the electrodes of the mass analyzer, which is shown in Table 4.6.

Table 4.6: Voltage settings for the entry and exit mirror of the analyzer for the operation in the injection mode. To introduce ions coming from the ion source into the mass analyzer, the entry mirror is switched to the pass-through configuration with all electrodes at ground. The exit mirror potential setting shifts the time focus onto the central plane of the MR cell.

Voltage (V)	Elec. 1	Elec. 2	Elec. 3	Elec. 4	Elec. 5	Elec. 6	Elec. 7
Entry mirror	0	0	0	0	0	0	0
Exit mirror	-2545	-1277	-1061	-493	1572	1857	3047

Ejection mode

This operating mode allows the ions to exit the MR cell after the desired dwell time to enable particle detection and flight time recording at the detector. For this purpose, the exit mirror is switched to a pass-through setting by applying the ground potential to all electrodes. During ejection through the last reflection in the field of the entry mirror, the time focus is shifted from the MR cell center to the detector plane to ultimately keep the instrument energy-isochronous. The beam is also widened as much as possible while still maintaining high transmission to cover a large area of the detector and thus achieve better detection efficiency. For this purpose, a potential distribution different from the MR mode is used in the entry mirror, which is again initially determined by multi-objective optimization with CPOpt.

The finally selected potential setting for this operating mode is shown in Table 4.7, as this configuration achieved the lowest time spread on the detector plane, as well as a broad expansion of the beam and thus a large and uniformly occupied incident area on the detector.

Table 4.7: Chosen voltage settings for the entry and exit ion mirror in the ejection mode. The high-voltage setting applied for the entry mirror shifts the time focus from the MR cell center to the detector plane and widens up the beam. The voltage setting for the exit mirror foresees the pass-through setting with ground potential applied to all electrodes for unhindered ion transition.

Voltage (V)	Elec. 1	Elec. 2	Elec. 3	Elec. 4	Elec. 5	Elec. 6	Elec. 7
Entry mirror	-4480	-5601	-1710	-1552	1564	1897	2591
Exit mirror	0	0	0	0	0	0	0

Mass range selection

While linear and reflectron TOF, as well as open-path MRTOF mass spectrometers have a theoretically unlimited mass range, closed-path MRTOF configurations have the decisive disadvantage that the unambiguous mass range described in Section 2.1.3 is essentially limited and depends on the number of full-turns performed. Measurements with high mass resolving power are therefore always accompanied by a limited mass range. The operational procedure for the measurement within a defined mass range is described below.

With a known target mass range, which is defined by the minimum (M_{min}) and maximum (M_{max}) contained m/z, the maximum number of full-turns that can be performed is first determined using Equation 2.18. Since the mass analyzer does not provide any information about the number of full-turns carried out during operation and must be controlled purely time-dependent, it is therefore necessary to be able to predict the number of full-turns performed and the position in the mass analyzer for each mass as a function of the flight time. For this purpose, a calibration measurement is conducted with the simulation, in which the flight times $t_{\mathrm{injection}}$ for the injection onto the central plane of the mass analyzer, which depend on m/z, as well as the full-turn flight times t_{FT}, the ejection time t_{ejection} and the drift velocities $v_{\mathrm{D,\,x}}$ along the optical axis are determined for the given voltage configuration. In order to set the number of feasible full-turns for the given mass range, the respective switching times for the entry and exit mirror are calculated based on these measured values to switch them from MR mode to the ejection mode. The optimum switching times for this result from the boundary conditions as shown in Figure 4.31.
Two boundary conditions are assumed for the switching of each mirror, which specify the earliest and latest possible switching process. These boundary conditions are

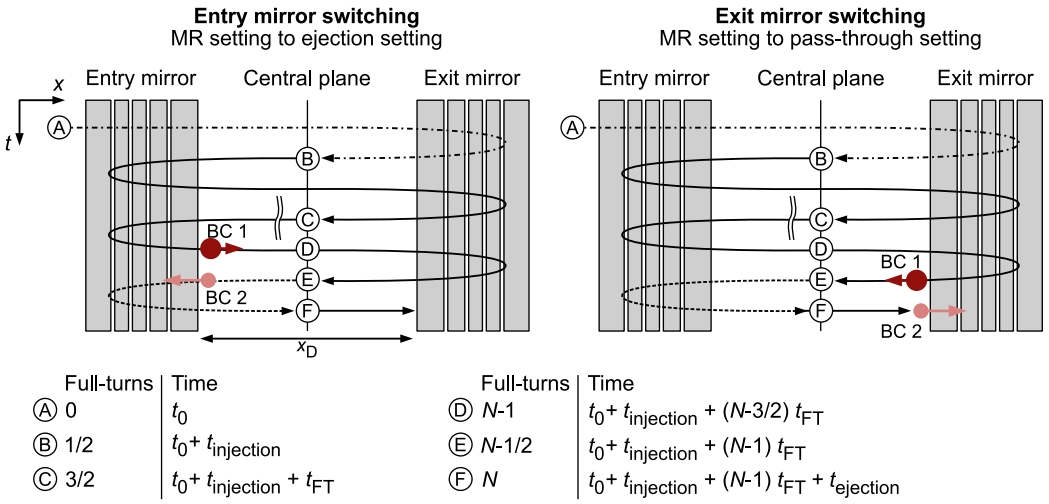

Figure 4.31: Boundary conditions to be considered for the identification of the optimal switching times for the entry and exit mirror from MR mode to ejection mode. The slowest particles (M_{max}) contained in the desired mass range deliver BC 1, while the fastest contained ions (M_{min}) indicate BC 2. The ion trajectories in the setup still reflect a closed-path configuration, while this graphical representation highlights the temporal dependence of the axial ion position in the mass analyzer.

given by the position of the fastest (M_{min}) and slowest particles (M_{max}). To switch the entry mirror from the MR potential setting to the ejection setting, the slowest particles that are about to complete $N-1$ full-turns must have already left the entry mirror (BC 1), while the fastest particles that have already completed $N-1/2$ full-turns must not yet have entered the field of the entry mirror for the last reflection (BC 2). The calculated entry mirror switching time for BC 1, which is given by

$$t_{\mathrm{entry,\ BC1}} = t_0 + t_{\mathrm{inject,\ M_{max}}} + (N-3/2)\cdot t_{\mathrm{FT,\ M_{max}}} - \frac{x_{\mathrm{D}}}{2v_{\mathrm{D,\ x,\ M_{max}}}} \tag{4.10}$$

thus represents the earliest possible switching time, while BC 2 indicates the latest applicable switching time, given by

$$t_{\mathrm{entry,\ BC2}} = t_0 + t_{\mathrm{inject,\ M_{min}}} + (N-1)\cdot t_{\mathrm{FT,\ M_{min}}} + \frac{x_{\mathrm{D}}}{2v_{\mathrm{D,\ x,\ M_{min}}}} \tag{4.11}$$

These equations require the previously measured data about the mass-dependent injection time to the central plane $t_{\mathrm{inject}}(M)$, the required flight time per full-turn $t_{\mathrm{FT}}(M)$ and the drift velocity $v_{\mathrm{D,\ x}}(M)$, which allows with the known drift distance

x_D to calculate the position-dependent drift times. Hence, a range for the switching time is given. In practice, the time delays due to the electronics have to be considered, such that these constraints must be taken into account for the selection of the applied switching time. Similarly, the switching time for the exit mirror is determined, where BC 1, describes the situation where the slowest particles have just performed the last reflection in the exit mirror. This reflects the earliest switching time for the exit mirror, given by

$$t_{\mathrm{exit,\ BC1}} = t_0 + t_{\mathrm{inject,\ M_{max}}} + (N-1)\cdot t_{\mathrm{FT,\ M_{max}}} - \frac{x_\mathrm{D}}{2v_{\mathrm{D,\ x,\ M_{max}}}} \tag{4.12}$$

The fastest particles, which have already performed the complete number of required full-turns N, must not yet be immersed in the exit mirror at the time of switching (BC 2). Hence, this defines the latest possible switching time for the exit mirror, given by

$$t_{\mathrm{exit,\ BC2}} = t_0 + t_{\mathrm{inject,\ M_{min}}} + (N-1)\cdot t_{\mathrm{FT,\ M_{min}}} + t_{\mathrm{eject}} + \frac{x_\mathrm{D}}{2v_{\mathrm{D,\ x,\ M_{min}}}} \tag{4.13}$$

After the slowest particles of the desired mass range have left the mass analyzer, the mirrors can either be switched back to MR mode or the resulting TOF spectrum is clipped after the peak of this mass. This method makes it possible to separate particles of a desired mass range with the same number of full-turns in the mass analyzer and then to extract and detect them. The required calibration data for the finally selected potential settings of the mass spectrometer are given in Figure 4.32.

Up to this point, with this method there is the fundamental problem that particles with a number of full-turns deviating from $N_{\mathrm{mass\ range}}$ also leave the MR cell when the mirrors are switched and superimpose the signal on the detector. Approaches to obtain a clear spectrum are either to clean up the spectrum by appropriate post-measurement data processing or to gradually remove particles beyond the desired mass range during the dwell time in the MR cell [87]. The latter method typically involves a deflector installed in the MR cell, which is activated with each full-turn of the particles and removes a fraction of the unwanted masses from the mass analyzer [55, 142], such that ideally only particles of the desired mass range can effectively reach the detector. Within this work, the idea of removing unwanted particles at every full-turn was followed, however instead of deflecting ions, the exit mirror was switched to the pass-through setting with each full-turn for a certain time window to let ions

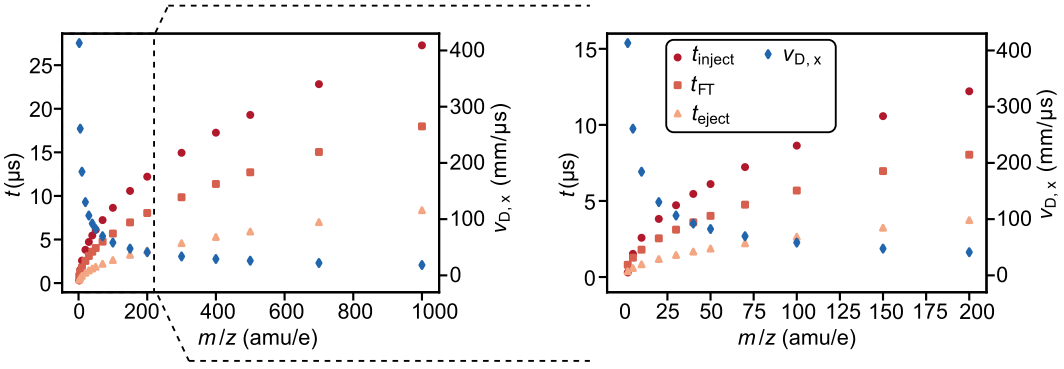

Figure 4.32: Simulated m/z-dependent flight times for the injection $t_{\mathrm{injection}}$, one full-turn t_{FT} and the ejection half-turn t_{ejection} and the drift velocity in direction of the optical axis $v_{\mathrm{D,\,x}}$. The simulations involve the operation with the source and the derived values represent the mean for all particles of the respective m/z.

outside the desired mass range leave the MR cell. The switching times were again derived based on two boundary conditions, which are shown in Figure 4.31 for the exit mirror. However, other than for the previously described ejection of the mass range of interest, the boundary conditions do not deliver the earliest and latest possible switching time to the pass-through setting, but give the start and end time for this potential setting. The time for each full-turn N to switch the exit mirror from the MR setting to the pass-through setting is given by the slowest particles of the considered mass range, which must have just left the exit mirror (BC 1). Switching back to the MR setting must take place at the latest when the fastest particles of the desired mass range reach the exit mirror again (BC 2).

Performance

To finally characterize the performance of the developed mass spectrometer and demonstrate its suitability for use cases in the fields of nano-analytics and space exploration, the MR operation of the entire mass spectrometer and all operating modes was simulated.

First, the characteristics of the mass resolving power were determined by performing varying numbers of full-turns for an iso-mass peak (40 amu/e). The initial simulation conditions were identical with the ones for the linear TOF characterization in Section 4.4.1. However, the primary time focus plane was kept at short focal distance by applying the respective voltage settings for the source and injection system derived earlier in Section 4.4.2 and the mass analyzer operation was involved with the settings

for the injection, MR and ejection mode. The particles were recorded on the detector plane after different number of performed full-turns (up to 400) in the mass analyzer and the evolution of the mass resolving power was derived, as shown in Figure 4.33.

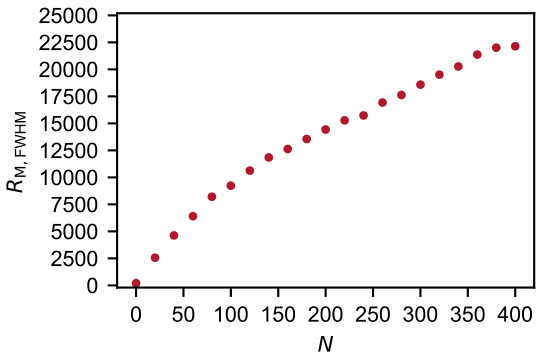

Figure 4.33: Evolution of the mass resolving power, measured at the detector plane, over the performed full-turns for full operation of the mass spectrometer.

The mass resolving power obtained after 400 full-turns exceeds 22000 and is thus higher than the simulated maximum mass resolving power for the chosen MR setting in Section 4.2.2. This is due to the fact, that the obtained initial particle distribution given by the source is more narrow than the particle distribution applied for the isolated simulation for the mass analyzer. Furthermore, there is a slow increase for R_{M} for the operation of the entire mass spectrometer, while for the isolated consideration of the mass analyzer in Section 4.2.1 and 4.2.2 a constant maximum R_{M} was already present after very few full-turns. This is due to the fact that for the simulation of the complete mass spectrometer there is an initial time spread caused by the ion source, which considerably limits the mass resolving power, while the isolated consideration of the mass analyzer did not include an initial time spread. With each additional full-turn performed, the influence of the initial time spread on R_{M} is reduced by extending the total flight time, allowing the mass resolving power to gradually approach the theoretical maximum value of $t_{\mathrm{FT}}/2\Delta t_{\mathrm{FT}}$. The overall transmission, given by the ratio of the number of recorded particles on the detector plane and the number of initially extracted ions from the source, was relatively stable for all full-turns with 55 %.

To evaluate the performance for operation with multiple masses, the mass spectrum of air was recorded again. To unambiguously measure the mass range from 14 to

44 amu/e, only two full-turns can be carried out. The resulting spectrum acquired on the detector plane is shown in Figure 4.34.

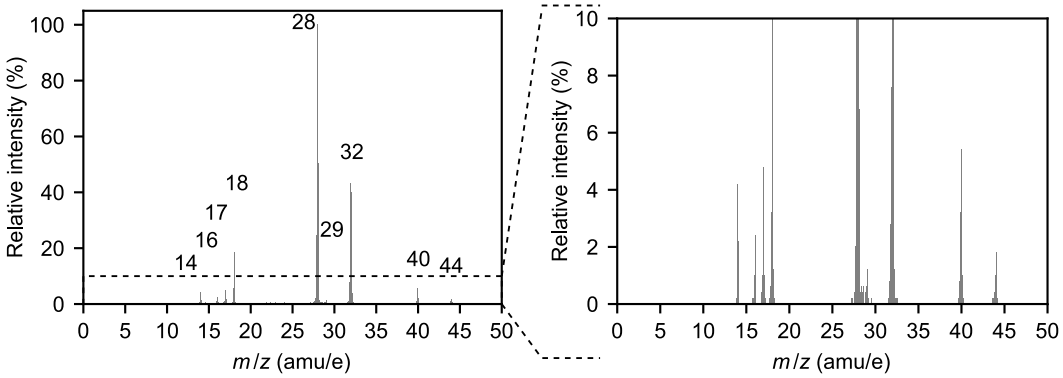

Figure 4.34: Mass spectrum of an air sample recorded at the detector plane after two performed full-turns in the MRTOF mass analyzer. To better visualize the weak peaks, the range for the relative intensity up to 10% is plotted separately.

The separation of the peaks is thereby already more distinct than with the linear TOF measurement. However, the air spectrum offers very closely spaced isotope peaks, which cannot be resolved individually in the full-spectrum acquisition. The ability to display such isotope peaks individually in a narrow mass range in the spectrum through correspondingly high-resolution measurement is the essential requirement for a MRTOF mass spectrometer to be used in nano-analytics and space exploration. In the air spectrum, a targeted measurement in the range from 17.9 to 18.1 amu/e is particularly interesting for this purpose. Two very close peaks, the oxygen isotope ^{18}O at 17.9992 amu/e and the water isotope $H_2{}^{16}O$ at 18.0106 amu/e, are contained in this range, which can be unambiguously resolved with up to 180 full-turns. The simulation initially includes the full air spectrum. The ion mirrors were switched in a time-dependent manner based on the methodology described above and the spectrum of the target mass range was recorded after a different number of full-turns on the detector. The results are shown in Figure 4.35.

In reality, ^{18}O would have a significantly lower relative intensity in the range of 0.005 % in this spectrum. Due to the extremely high computational effort required by the simulation for a statistically meaningful number of particles for this mass, the ^{18}O isotope was enriched for this evaluation. The high mass resolving power of more than 10000 obtained after 100 full-turns allows to reliable resolve the two isotopes as individual peaks. Higher mass resolving power obtained by performing even more

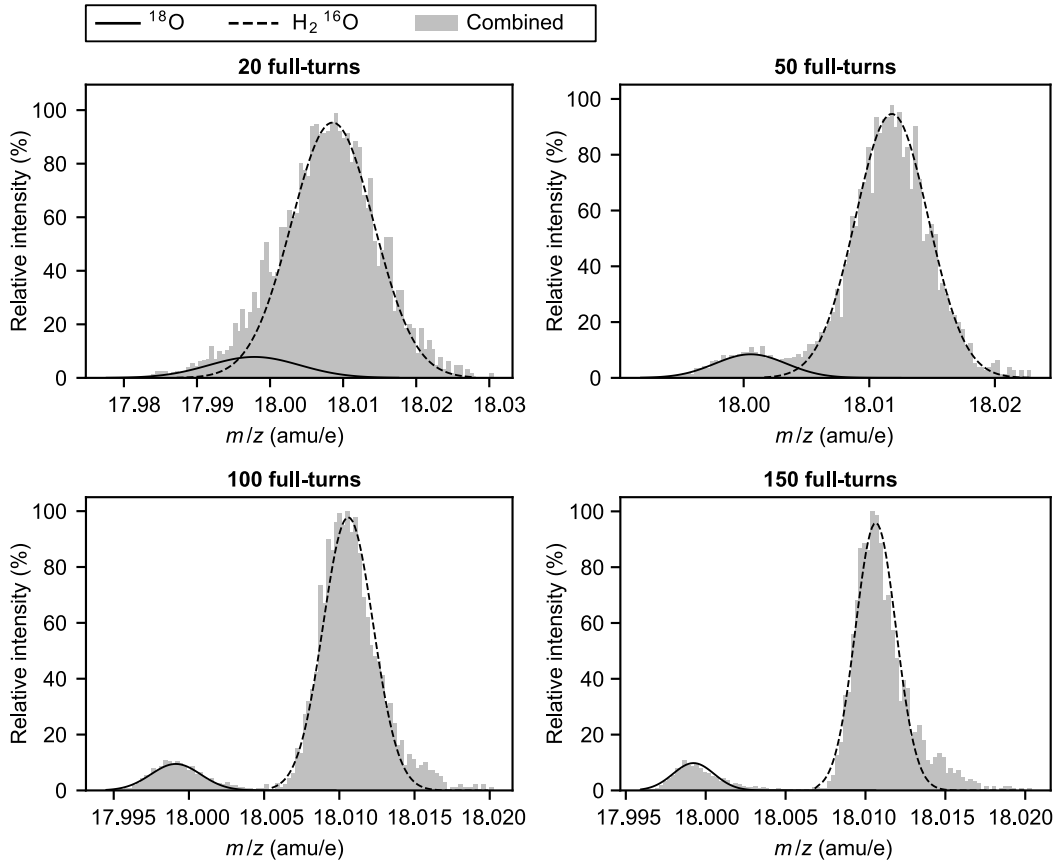

Figure 4.35: Mass spectra obtained for the target range around mass 18 amu/e to resolve the isobar peaks for enriched ^{18}O (17.9992 amu/e) and $H_2{}^{16}O$ (18.0106 amu/e) after different number of performed full-turns. While the low mass resolving power after few full-turns is not sufficient to resolve two individual peaks, the high mass resolving power after 100 full-turns allows to resolve the two isotopes as individual peaks.

full-turns in the mass analyzer further improves the separation. The mass accuracy is given by 27 ppm after 100 full-turns.

4.5 Summary and conclusions

A compact and powerful MRTOF mass spectrometer was developed using computer-aided methods for simulation and optimization. The main component of the instrument is an axially aligned and rotationally symmetric closed-path MRTOF mass analyzer. The design concept provides an energy-isochronous operation of the mass analyzer for each full-turn, which implies that the time focus is located in the center of the MR cell after each performed full-turn of the ions. This requires different voltage settings for the ion injection, multiple-reflection operation in the MR cell, and ion ejection to the detector, each of which adjusts the position of the time focus. An initial design for the mass analyzer was derived using analytical approaches and manual parameter tuning, focusing on the geometry and voltages of the electrodes. However, the output characteristics obtained did not meet the required specifications for mass resolving power and transmission. A modified approach for the spatial focusing of the ion beam was implemented, assisted by automated optimization using the developed optimization framework CPOpt. In this approach, the particle beam is not sharply focused in the MR cell center for each reflection, which inevitably causes strong divergence behind the focal plane. Instead, off-axis trajectories and angular divergent behavior of the ions are gradually reduced to approximate the ideal trajectory along the optical axis. Further design optimization, using MOGA optimization, focused on both the temporal and spatial domains and included tuning of electrode voltages and selected geometry parameters. The evaluation of the optimization results, combined with a sensitivity analysis, showed that the optimal solution space is very close to the initial geometric arrangement. Geometric design changes have a minimal effect on the output characteristics compared to voltage changes. Therefore, the optimized design of the mass analyzer retains the initial geometric shape and arrangement of the electrodes, but with an improved voltage setting. The MRTOF operation with up to 400 full-turns demonstrated an increase in the maximum achievable mass resolving power by a factor of 5, reaching 15000 for the initial particle distribution used, which meets the set requirements. The total transmission in the mass analyzer could be increased from 60 % in the initial design to 90 %. The modified focusing concept was thus able to improve the transmission characteristics.

The operation of TOF mass spectrometers require temporally pulsed initial ion bunches. The storage EI ion source is a promising method for generating such ion packets for MRTOF due to the increased sensitivity by accumulation of continuously

generated particles before the pulsed extraction. Simulations to determine suitability showed sufficiently good trapping properties. An initially high injected count of ions is decisive for the sensitivity of the obtained spectrum, especially for high-resolution MRTOF. However, the evaluations of the conventional operation principle for the pulsed ion extraction indicated, that a trade-off between different performance characteristics has to be made. Most importantly, continuous ionization during the extraction phase is problematic, as it generates significant background noise in the recorded spectrum. This results in weak peaks being lost in the noise and no longer reliably detected. Therefore, with the conventional method, the extraction phase must not last too long, which in turn has an impact on the choice of the extraction voltage.

A modified approach for the pulsed extraction of ions in the storage EI ion source was developed, which synchronizes ionization with the extraction process. To achieve this, the continuous electron beam is diverted during the extraction phase, preventing ionization in the ionization chamber. The design of an existing continuously emitting EI ion source was modified so that both the cap electrode, which separates the ionization chamber from the subsequent acceleration electrodes, and the shielding electrode around the filament can be pulsed with dedicated potentials. This modification allows for the prevention of continuous ionization during extraction, thereby eliminating the noise that would otherwise contaminate the spectrum and significantly improving the SNR. Additionally, the extraction process is simplified, as the duration of the extraction pulse can be chosen independently of noise behavior, and time-of-flight errors caused by varying ion start times during extraction are eliminated. As a result, long extraction pulses can be used to cover a wide mass range while maintaining a low voltage gradient at the cap electrode, which in turn narrows the distribution of particle energy. The test series with this new extraction method have shown that pulsed ion bunches can be generated for the selected parameter values. Very low energy spread of less than 15 eV (FW50) for a considered range for m/z from 2 amu/e to 500 amu/e was achieved. For this purpose, a voltage gradient of 60 V was applied to the cap electrode for extraction. The duration of the extraction pulse was increased to 1750 ns to extract a mass range of up to 500 amu/e even for this low voltage. With these settings, a time spread (FW50) of 25 ns could be achieved for $m/z = 50$ amu/e on the measurement plane. The novel extraction method was compared with the conventional method for recording the TOF spectrum of air. The novel method effectively reduced background noise, allowing even very weak peaks for m/z of 40 and 44 amu/e to remain detectable, while these peaks were lost in the

noise with the conventional method. With the new modified operating mode, the pulsed EI storage ion source thus provides significantly improved starting conditions for MRTOF mass spectrometers.

The developed ion source and MRTOF mass analyzer were ultimately tested and evaluated together in the simulation. The operation as linear TOF envisages the entire mass analyzer being used only in pass-through mode and thus as an extended drift tube. The unambiguous mass range is unrestricted in principle, but only a very low mass resolving power of 95 could be determined for 40 amu/e. On the other hand, operation with several reflections in the mass analyzer provides a significantly increased resolution depending on the number of full-turns performed. The optimization framework was used to determine voltage settings for the injection and ejection mode in order to shift the time focus accordingly. The iso-mass operation of the complete instrument demonstrated a mass resolving power of more than 20000 at the detector plane for 40 amu/e and 400 full-turns, with a total transmission of 30 % relative to the number of ions extracted from the source. To precisely set the considered unambiguous mass range during MRTOF operation, a methodology was developed that enables time-dependent control of the ion mirrors. The switching times are set based on boundary conditions and previously recorded calibration data for different m/z values, ensuring that ideally only particles of the desired mass range are ultimately detected. This methodology was validated in the simulation in combination with a high-resolution measurement of closely spaced isotope peaks for ^{18}O (17.9992 amu/e) and $H_2{}^{16}O$ (18.0106 amu/e). While a small number of full-turns does not provide the necessary resolution to separate these isotope peaks from each other, a clear separation of the two peaks in the mass spectrum was achieved from 100 full-turns. This demonstrated the fundamental suitability of the developed mass spectrometer for demanding analytical tasks in the field of nano-analytics and in space exploration.

5 Prototyping

The developed and optimized design for the MRTOF mass spectrometer was finally transferred into a prototype. This chapter describes the development and integration of the required electronic components and circuits and the data acquisition system. It also describes how the geometric design from the simulation was transferred into a concrete mechanical design and how the manufactured parts were assembled and integrated into a test bench. Finally, this chapter also contains an outlook on planned experimental tests with this prototype.

5.1 Electronic prototyping

Advanced electronic systems are required to operate the mass spectrometer in accordance with the simulated conditions. In particular, the fast and reliable switching of the electrode potentials in the range of several kV is challenging. The concept for the electronic components is shown in Figure 5.1 and is explained in more detail in the following section.

In contrast to the design of the optical components of the mass spectrometer, a compact design was not taken into account when designing and developing the electronic system for operating the mass spectrometer. This prototype was primarily intended as a demonstrator and development model to test the operating concept and the electronic circuitry. A high degree of flexibility with regard to the wiring of the electrodes and the available performance margins of the components used was favored for extensive testing of a compact design. For later versions of this instrument, which are attributed to a dedicated application, the electronic system can be designed according to the specifications and thus reduced.

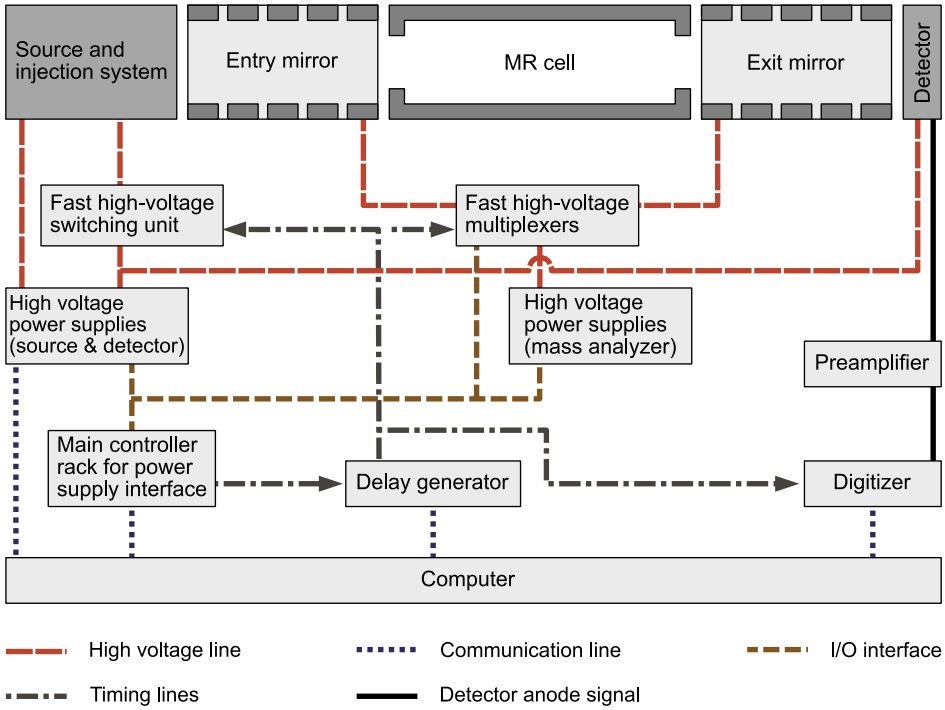

Figure 5.1: Block diagram of the electronic components for the system operation, control, and data acquisition.

Main controller rack

The main controller rack comprises several essential components for data acquisition and system control. At its core is a cDAQ-9178 (National Instruments, Austin, USA) data acquisition system, which serves as the central hub for various input and output modules. This system is connected to the main computer via USB and provides an array of 64 digital input/ output (DIO) channels, 48 analogue outputs, and 32 analogue inputs. A key feature of this setup is the inclusion of a fast DIO module, specifically designed to generate trigger signals for precise timing line synchronization. The analogue inputs and outputs are used for controlling and monitoring the high voltage power supply modules within the system. The digital outputs are utilized to activate high voltage lines, while digital inputs are employed to monitor the status of high voltage transistors in the fast multiplexers. To ensure safety and protect the system from potential damage, a dedicated safety circuit is integrated into the main controller rack. This circuit is designed to automatically open high voltage relays on each high voltage line in the event of a vacuum failure. Additionally the main

controller rack contains an AC/DC converter which provides low voltage supply for stable operation of the rest of the contained electronics in the setup.

Power supply and fast electrode switching for the source and detector

The high voltage power supply system for the source and injection system comprises several specialized components designed to allow the novel operation method, described in Section 4.3.2. At its core is a floating circuit that operates at the ionization chamber voltage U_{chamber}, providing biasing for the filament and the cap electrode, as shown in Figure 5.2 (a), and controlling the ion trapping and extraction.

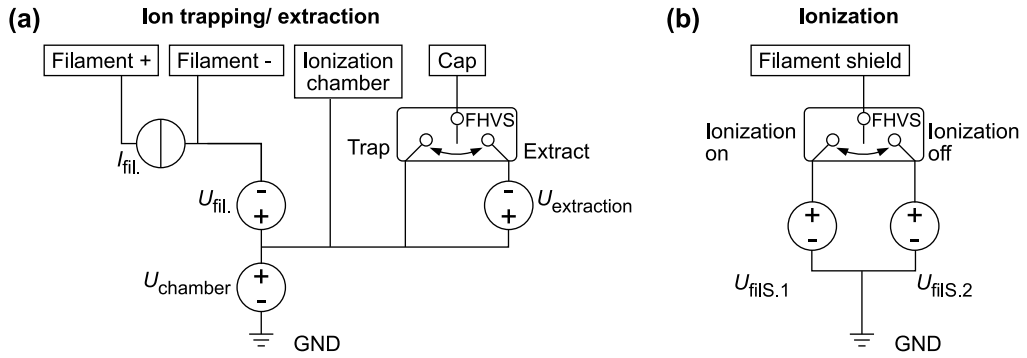

Figure 5.2: Circuitry for power supply and fast electrode switching for the source. A fast high voltage switch (FHVS) is applied for the cap electrode and the filament shield to allow fast switching between different potentials at high voltage.

Based on the chamber potential, the potential of the filament and the extraction potential for the cap electrode are set by additional power supplies given by the Ultravolt V series and US series modules (Advanced Energy, Denver, USA). For the filament, a FF015DAA079 power supply (Applied Kilovolts/ Adaptas Solutions, Worthing, United Kingdom) is utilized to provide the heating current. This unit is capable of delivering up to 5 A at 7.5 V and features an insulation voltage of ± 15 kV, making it suitable for high-voltage environments. To quickly switch the cap electrode from the trapping phase to the extraction phase and vice versa, the respective potentials are permanently given by the circuit and a FHVS is used to quickly connect the cap electrode to the respective potential. For this, a GHTS 60 (Behlke, Kronberg, Germany) switching unit is applied. The same circuit principle is used to control the ionization process by pulsed potential application to the filament shield, as shown in Figure 5.2 (b). The circuits employ serial communications over optical fiber to interface with the

control PC, ensuring electrical isolation and noise reduction. The detector's floating power supply is given by a MCP series (Spellman, Hauppauge, USA). This module is rated for up to 3 kV at 330 µA, also with an insulation voltage of ±15 kV, providing the necessary high voltage for detector operation while maintaining electrical isolation.

Power supply and fast electrode switching for the mass analyzer

The mass analyzer has an own set of power supplies, given by the Ultravolt D series Advanced Energy, Denver, USA). To allow three different operating modes for the mass analyzer (injection, MR, ejection), the potentials applied to the mirror electrodes have to be quickly switched to different values. This is done by providing for each operating mode the corresponding electrode voltages by distinct high voltage power supplies. Each of the in total 14 mirror electrodes is provided with three different potential settings, as shown in Table 5.1.

Table 5.1: Potential settings for the different operating modes of the mass analyzer.

Operating mode	Entry mirror	Exit mirror
Injection	Pass through	Time focus shift injection
MR	MR	MR
Ejection	Time focus shift ejection	Pass through

Thereby, the pass through setting is given by applying the ground potential to all electrodes of the mirror, the MR potential setting is equal for both ion mirrors, while the settings for the time focus shift for injection and ejection differ. Thus, there are three different high voltage settings in total to be applied to the ion mirrors. This requires 21 (3×7) high voltage power supplies to operate the mass analyzer. Given the optimized potential settings, 9 positive high voltage and 12 negative high voltage power supply modules are used for that.

To quickly switch an ion mirror to another potential setting, each mirror electrode is provided with a high voltage fast multiplexer between the electrode and the power supplies. The high voltage fast multiplexers consist of three rapid high voltage transistor switches. The reference model for these fast high voltage transistor switches is the HTS 61-03-C (Behlke, Kronberg, Germany). They can operate at a maximum voltage of ±6 kV, with typical turn-on and turn-off times of less than 10 ns.

Delay generator and timing lines

The delay generator contains two boards, DG-42 (TEO Technology, Oceanside, USA), which provide 8 programmed delay pulses from a trigger pulse coming from the main controller. It also includes a fast logic card to generate complementary pulses related to the pulses from the DG-42 board. For example, the entry electrodes have three possible configurations: Pass trough, MR, and time focus shift ejection. Only MR and time focus shift ejection pulses are generated directly, while the pass through signal is derived from both using multiple logic gates on the signal line. The transition time of the logic gates is used to allow enough time for the high voltage transistors to safely switch between configurations.

Detector signal acquisition

The detector signal acquisition system comprises two essential components. The preamplifier is the model TA2000B-1 (FAST ComTec, Oberhaching, Germany), featuring a selectable gain of 10 or 20 and a bandwidth of 2 GHz. Complementing this is the digitizer, which is the model M5i.3321 (Spectrum, Grosshansdorf, Germany). This digitizer offers a bandwidth of 1 GHz and a sampling rate of 3.2 GS/s on two channels with 12-bit resolution.

Computer

To control the instrument, a generic PC is used, which is connected with the delay generator, the main controller rack and the high voltage power supplies for the source and the detector. The digitizer is directly attached to the computer via a peripheral component interconnect express (PCIe) slot.

Control software

The software to control the instrument and to acquire and process the data is based on a LabVIEW user interface. The main functionalities of this software are the definition of the high voltage settings and presets and the adjustment of the timing settings for the operation of the mass spectrometer. Further, the signal acquisition from the digitizer is a major task of this software.

5.2 Mechanical prototyping

The ion-optical design of the mass spectrometer from the simulation was transferred to a CAD model. The necessary components and parts were manufactured and assembled in the prototype of the optical setup. For all subsystems, the electrodes were made out of stainless steel (AISI 316L). The following describes the approaches taken in the construction of the prototype and how it was ultimately realized and implemented.

5.2.1 Testbench and integration concept

The prototype was integrated into an existing vacuum testbench. For this purpose, the entire optical setup of the spectrometer was mounted in a stacked arrangement on a lateral support structure. The support structure consists of two stainless steel rods and aluminum (EN-AW 6061-T6) crossbars and is attached distally via the rods to the vacuum flange. The instrument mounted on the support structure is shown in Figure 5.3.

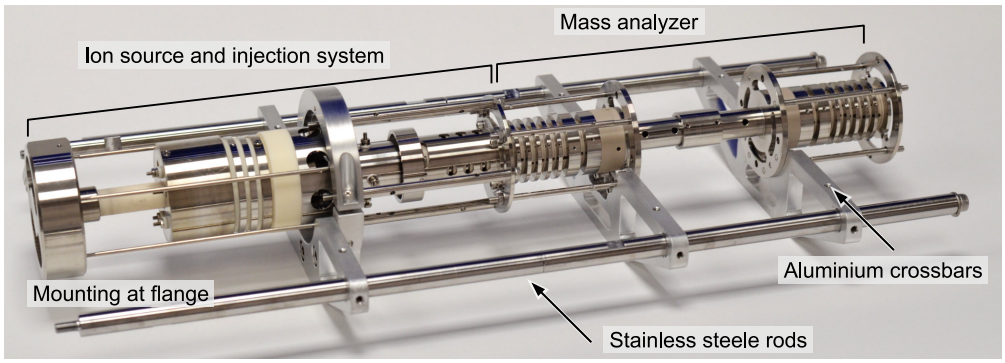

Figure 5.3: MRTOF instrument without the detector mounted on the support structure, which will later be attached to the vacuum flange.

Seven feedthroughs are incorporated into the vacuum flange, which serve as conduits for all electrical supply lines. Additionally, the gas supply line is integrated into the vacuum flange via a leak valve. This means that the entire mass spectrometer is only in contact with the vacuum test bench via the vacuum flange, as shown in Figure 5.4. The mounting of the full instrument to the vacuum flange allows a convenient integration into the vacuum chamber. The entire instrument can thus be moved out of the vacuum chamber via the sliding stage, which allows very easy access to all components during assembly and any necessary modifications or interventions.

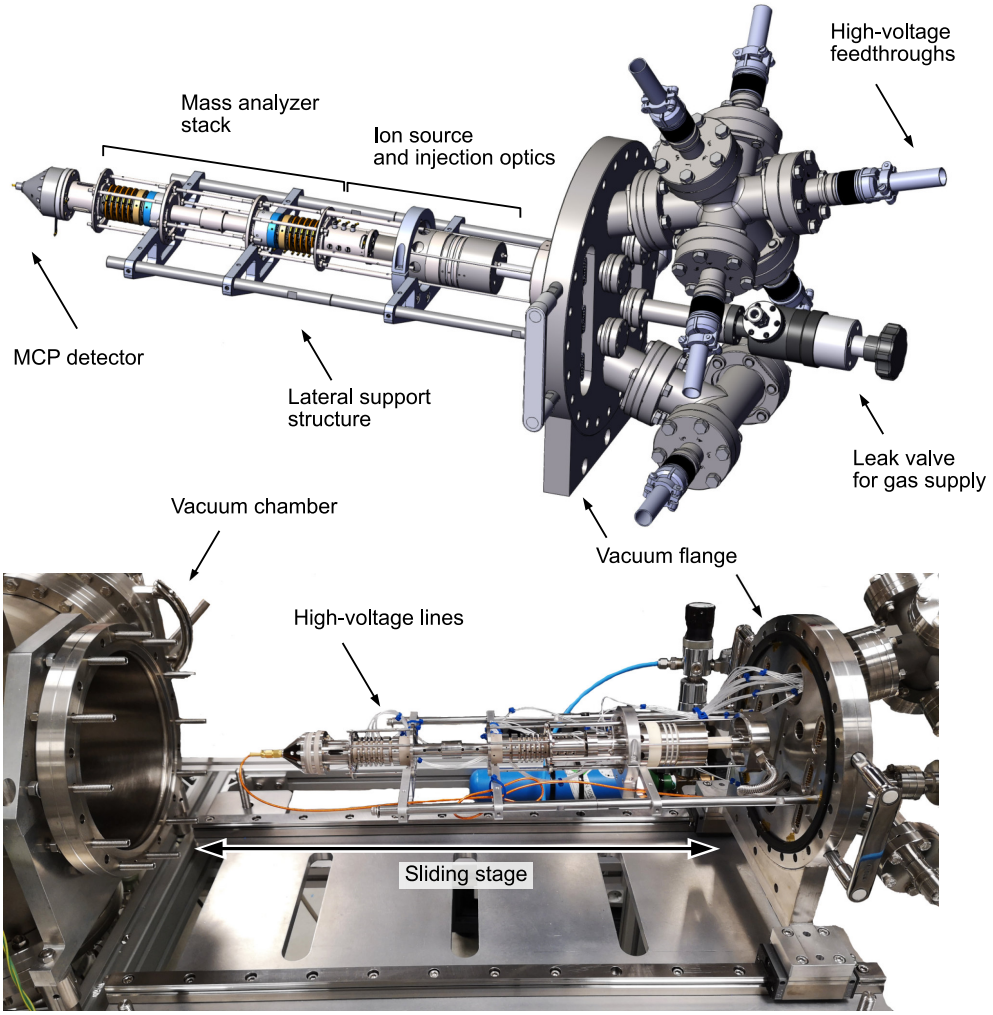

Figure 5.4: The axially aligned stack of the MRTOF optical components. All the components are mounted to the support structure, which is attached to the vacuum flange. A sliding stage allows rapid access to the full setup. Feedthroughs in the vaccum flange allow the connection of the electrical supply lines.

Vacuum system

The vacuum system for the testbench is composed as follows. An nXDS-20i scroll pump (Edwards Vacuum, Burgess Hill, United Kingdom) serves as the primary pump. A HiPace 300 P turbomolecular pump (Pfeiffer Vacuum, Asslar, Germany) allows a measured minimum pressure of 0.4×10^{-7} mbar to be reached in the chamber with the prototype inserted. An IONIVAC ITR 200 vacuum gauge (Leybold, Cologne,

Germany) is used to monitor the vacuum level. An Edwards nXDS-10i scroll pump is applied to pump the gas supply line.

5.2.2 Ion source and injection optics

The ion source is based on an existing continuously emitting EI source with integrated permanent magnet around the ionization chamber. The ion source was mechanically modified in such a way that certain electrodes and components were replaced or integrated differently. This was done based on the results of the simulations and the optimization, outlined in Section 4.3.2, in order to be able to use the new pulsed mode of operation. A cross-section of the ion source in the CAD model is shown in Figure 5.5 together with details on the arrangement of the respective electrodes and their electrical connection. All electrical insulators in the source were made out of ceramic (Al_2O_3) due to the high temperature requirements given by the filament heating.

The main modifications to the ion source were made in the area of the ionization chamber and the filament in order to implement the pulsed operation and the new extraction method developed for the EI storage ion source at hardware level. The mechanical modifications were based on the electrical circuitry of the ion source shown in Figure 5.5. To enable the application of individual electrical potentials to the ionization chamber, the cap electrode, the filament and the filament shielding, the cap electrode was modified and insulated from the filament shielding using a ceramic ring. The iridium filament with yttrium oxide coating IS/QMA 125 (Peiffer Vacuum, Asslar, Germany) was also electrically insulated from all surrounding components by the use of ceramic spacers. A further modification was made for the Accel. 3 electrode by attaching a cylinder directed towards the ionization chamber. As this electrode is always at ground potential, the cylinder serves to improve the potential transition between Accel. 2 and Accel. 3 so that the electric field cannot spread into the areas behind it.

The ion source was already equipped with a set of four orthogonally arranged deflector plates after Accel. 3. In normal operation, these deflector plates are not foreseen to be actuated, but electrical connection and electronics to use them if needed are provided. Subsequently, an aperture was installed to limit the beam diameter. For this purpose, a small exchangeable molybdenum aperture plate with different available hole diameters was used in a larger recess (diameter 2 mm). This allows a quick variation of the aperture size in the range of 0.4 to 2 mm by changing the inserted

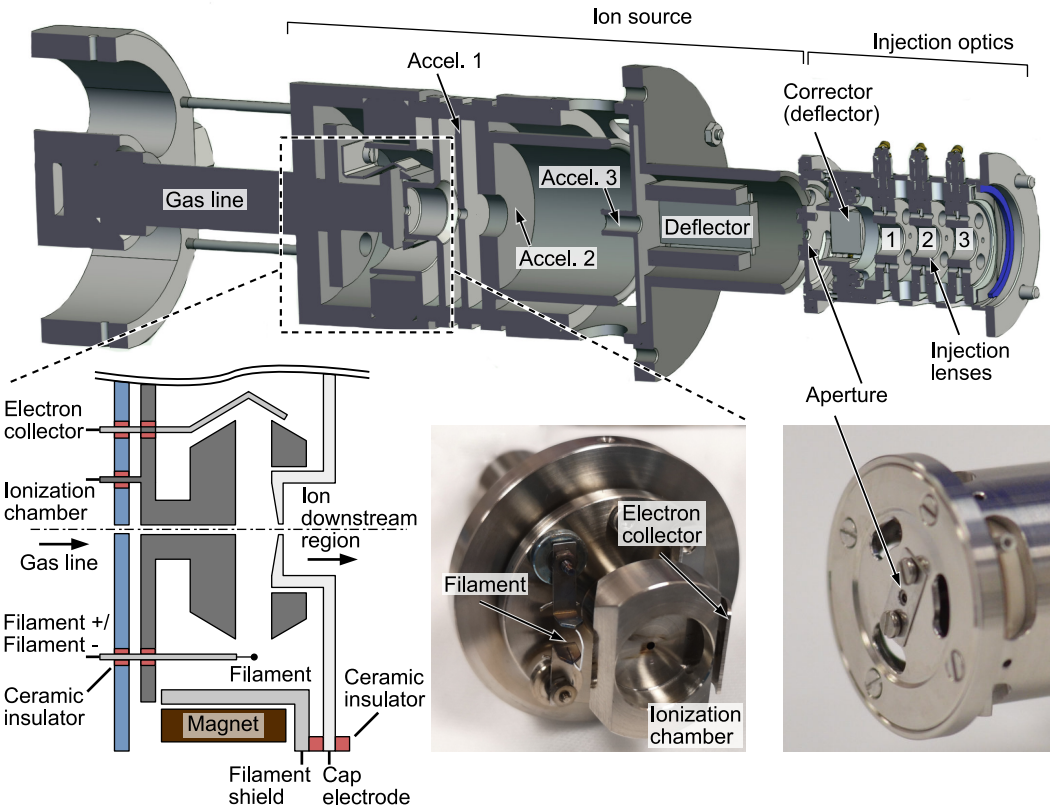

Figure 5.5: Cross-section view of the ion source and injection system. The ion source part is based on an existing continuously emitting EI source, which was modified to operate in pulsed mode. The rearrangements and modifications of the concerned electrodes are highlighted. Exchangeable aperture plates with different hole diameter are mounted to a larger recess. The injection optics comprise deflector plates for beam correction and an injection lens for spatial beam focusing.

plate. An aperture with a hole diameter of 1 mm was used in the prototype.
This aperture is followed by the injection optics, which consist of four orthogonally aligned deflector plates, referred to here as the corrector, that can adjust the beam alignment after the aperture if necessary. During normal operation, all corrector plates are set to ground potential. Following this, three injection lens electrodes focus the ion beam in the spatial domain.

5.2.3 Mass analyzer and detector

The mass analyzer consists of two symmetrical parts. For each part, an ion mirror is firmly connected to one half of the drift tube. The electrodes were placed on top of

each other in a stacked arrangement with a polyether ether ketone (PEEK) insert between the electrodes for electrical insulation. This arrangement is held together by screwing the first and last electrodes, which are both at ground potential, together using rods. This assembly for a single ion mirror and half of the drift tube is shown in Figure 5.6. The approach of separating the drift tube into two identical parts was chosen to maintain flexibility in the mechanical prototype for adjusting the exact length of the drift space. For this, the distance between the two drift tube parts can slightly be varied by moving the exit mirror and the detector laterally within the support structure.

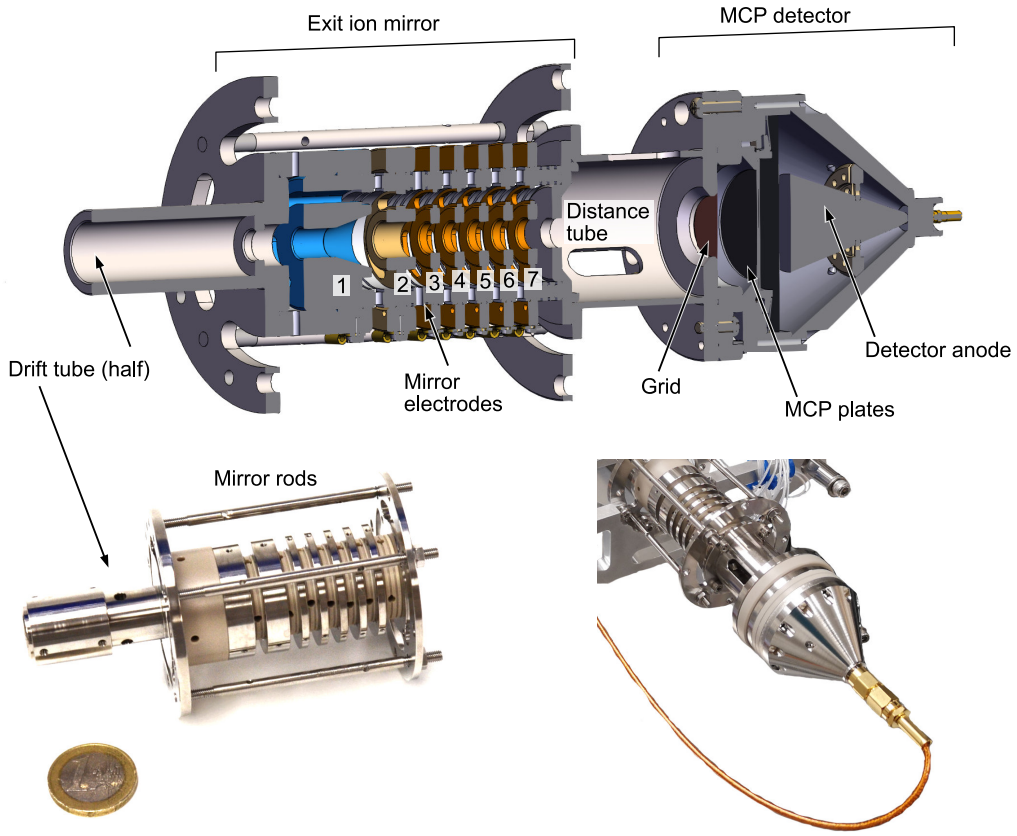

Figure 5.6: Setup of the ion mirror with connected half of drift tube and the detector. The mirror ring electrodes are stacked on each other and are fixed by the rods, attached to the first and last electrode. A grid before the MCP detector allows to apply high negative voltage to the MCP front.

The MCP-type APD 2 APTOF detector (Exosens/ Photonis, Merignac, France) was mounted behind the exit mirror with a 3 cm long distance tube placed in between. This tube could comprise further correction optics, if needed. A grid was placed

before the front of the MCP plates to allow the application of high negative voltage to the MCP front while not disturbing the field-free exit mirror during the ejection. The integration of the detector is also shown in Figure 5.6.

5.3 Outlook on future experimental testing

The future experimental work with the prototype will initially involve several series of tests to determine the function of the system and to incorporate the concept and the parameters from the simulations for operation in the different performance regimes. Some components of the prototype have already been commissioned as part of this work. On the one hand, the function of the ion source for generating a continuous ion current was tested and verified. Initial tests for pulsing the source electrodes (cap and filament shield) have been carried out and particles have been detected with the MCP detector. However, further tests for conditioning and verification of the electronic components are required to perform time-resolved measurements of the mass spectrum.

Once this conditioning has been completed, the overall system will initially be tested and evaluated for operation as a linear TOF mass spectrometer. This also includes the characterization of the ion source for trapping ions and for the novel pulsed extraction process. Thereby, the comparison with the conventional extraction method is of special interest. At the same time, the correctness of the tuned potential settings for the time focus shift onto the detector plane as well as the functionality of the detector and the data acquisition system are tested.

After the experimental verification of the operation as a linear TOF mass spectrometer, the tests and measurements will be extended to include the mass analyzer with the time-dependent fast switching of the mirror electrodes. This will involve the verification of the simulated potential settings for the different operation modes as well as extended tests for the timing of the mirror actuation to allow the switching between the operation modes. The effects of time delays due to the electronics must therefore be carefully evaluated to adjust the system for ultimately performing high-resolution mass measurements.

6 Conclusions and Outlook

6.1 Conclusions

In this thesis, a novel compact, yet high-performance MRTOF mass spectrometer for different use cases, primarily in nano-analytics and space exploration, was developed. The ion optical setup of the mass analyzer was realized by an axially aligned stack of ring electrodes forming a symmetric MR cell in a closed-path configuration. The MR cell, including two opposing identical ion mirrors and an intermediate drift tube, provides a length of 20 cm and an effective diameter of 5.5 cm. The design and potential setting of the analyzer were tuned and validated with dedicated computational methods, developed within the thesis to facilitate and enhance complex CPO design. This yielded improved focusing properties and performance of the analyzer. Further, a pulsed ion source and injection system with a novel extraction method for enhanced SNR and duty cycle and reduced ion energy spread was developed, which fulfills specifically the requirements for operation with MRTOF. Overall, the developed mass spectrometer provides a simulated mass resolving power exceeding 20000 (FWHM) at m/z of 40 amu/e. The simulation design was transferred to a mechanical prototype with fast electronics, integrated in a vacuum test bench. The full optical setup thereby provides a total length below 50 cm and a weight of 2.5 kg. The clear separation of two closely spaced isotope peaks (^{18}O at 17.9992 amu/e and $H_2{}^{16}O$ at 18.0106 amu/e) in the recorded mass spectrum of the simulation was achieved for the MRTOF operation with 100 full-turns performed, which confirms the suitability of the instrument for demanding analyses in the field of nano-analytics, such as in life science applications, and space exploration. The reliable high-resolution measurement is facilitated by an operational protocol for the mirror switching developed to precisely select the mass range to be analyzed. The obtained combination of compactness and performance

demonstrates a clear advancement compared to existing instruments and allows with the scalable design and flexible operation principle implementation in nano-analytics and space exploration.

6.1.1 MRTOF mass spectrometer

The design and operation principle of a closed-path MRTOF mass analyzer was selected to achieve the highest compactness in combination with a very high achievable mass resolving power. After injection, the ions perform a selectable number of revolutions in the MR cell before they get ejected towards a fast MCP detector. The number of full-turns is proportional to the mass resolving power and the analysis time and inversely proportional to the transmission and the unambiguous mass range. The performance regime can thus be balanced very precisely. The design and tuning of the potential set of the ion mirrors was a critical step in the development of the mass analyzer. Higher-order particle focusing in the time domain with respect to the initial spread of energy and off-axis position and angle was achieved by analytical and computational optimization approaches, allowing low aberrational time spread per full-turn and thus enhanced characteristics for the mass resolving power. Further, a new strategy for the confinement of the ions in the spatial domain was applied, demonstrating a gradual approximation of particles flying off-axis towards the ideal on-axis trajectory with each full-turn. This again contributed beneficially to the achievable mass resolving power and the transmission characteristics.

For the ion source and ion injection system, the focus of the work was put on the capability to form temporally dense ion packets with ideally high ion count. These pulsed ion bunches are required for the injection into the mass analyzer. A technique has been evaluated in the simulation, namely a pulsed EI storage ion source, which allows particle accumulation during the trapping phase. The pulsed particle release during the extraction phase enables the formation of short ion bunches with high particle count. However, with the conventional extraction method different trade-offs have to be made with respect to performance characteristics, such as the time spread, the energy spread, the extraction efficiency and the spectral background noise, induced by ions being continuously created during the extraction phase. Hence, a novel extraction method for this type of ion source was developed, which involves the synchronization of the ion creation and extraction. This method effectively avoids the particle-induced spectral background noise, which allows high-sensitivity measurements with high SNR. Further, cross-dependencies between different performance

metrics can be avoided with this method, such that the operation in a more balanced parameter range is possible, which ultimately allows the formation of temporally dense ion bunches with low energy spread and high extraction efficiency. Especially, the low energy spread is beneficial for high-performance MRTOF measurements, where the energy-induced aberrational time spread created with each mirror reflection becomes the main resolution limiting factor for a high number of performed full-turns.

6.1.2 CPO optimization framework

A novel computational framework for optimization in CPO was developed to combine advanced optimization strategies, involving multiple-objective and multiple-parameter optimization, with flexible modeling and profound data analysis techniques. The framework developed, referred to as CPOpt, combines a MOGA with FDM simulation in SIMION and data evaluation routines in Python. The focus was placed on the modular structure and the flexible integration of the individual components. A communication interface allows for the fully automated operation of the optimization and modeling process. The framework significantly contributed to the design and optimization tasks in the development of the MRTOF mass spectrometer.

The MOGA is based on the open-source Python library DEAP and integrates a NSGA-II as a Pareto technique for multiple-objective optimization. CPO-specific adjustments to the optimizer code were applied, such as grouping for different types of parameters and techniques to establish high parameter diversity while still satisfying global design constraints. Optimization upon existing solutions is possible and facilitates the improvement of existing designs and adaptation to fulfil new requirements. The optimization algorithm was successfully validated with a test case comprising the simultaneous tuning of voltages and radii of six electrodes for two objectives.

To model the parameter configurations delivered by the MOGA throughout the optimization process, the SIMION platform was utilized in the framework. The API was used to establish a communication interface based on ZeroMQ, enabling fully automated interaction between the MOGA and the simulation. The influence of various settings on simulation accuracy has been evaluated. Parallelizing the simulation reduces modeling time and allows distribution across multiple computers. The CPOpt was exclusively applied for systems with rotational symmetry in this thesis, however, 3D arrangements can be handled by the simulation with the cost of reduced

computational efficiency. As SIMION provides no possibility for the calculation of magnetic fields, the applicability for systems with such fields is limited.

The CPOpt framework enhances multiple-objective optimizations in CPO by filtering complex Pareto data and identifying optimal solutions through a series of analysis steps. It reduces the solution space while providing valuable insights for decision-making. Fitness data correlations reveal system input-output relationships, while clustering further narrows the solution space. Key parameter configurations are re-evaluated under statistically valid conditions to assess physical performance beyond abstract fitness values. A novel aspect is the integration of global sensitivity analysis and LHS, which refines the solution and reveals further optimizations. Although this method increases computational effort, it identifies high-performance, stable parameter configurations effectively.

6.2 Outlook

From a technological perspective, there is room for further improvements, modifications and extensions to both the MRTOF mass spectrometer and the optimization framework CPOpt, which are discussed in more detail below.

Further miniaturization

The MRTOF mass spectrometer developed provides very compact dimensions and high performance in terms of achievable mass resolving power, ion transmission and SNR and duty cycle. However, the overall length of 49 cm of the readily assembled ion optical setup of the prototype is large in relation to the length of 20 cm of the MR mass analyzer as the main component. This is due to the fact that the prototyped ion source is based on an existing bulky ion source, which was mechanically modified in parts and extended by some injection lens optics, ending up in a length of 21 cm, where alone the gas line claims a length of 6 cm. The objective of the ion source prototyping was to have full flexibility in terms of operation to prove the concept. For the implementation in a dedicated application, the customized ion source and injection system can be further developed and miniaturized while maintaining the operation principle. Some early simulations demonstrate that an overall length of the ion source from 3 to 5 cm can be feasible to ultimately facilitate a total instrument length about 30 cm, representing the lateral dimensions of a 3U CubeSat [143]. Integration into such a microsatellite can extend the use cases in space exploration.

Application scenarios such as analysis of planetary atmospheres [29] or monitoring space weather [144] thus become possible with cost efficiency. The mass analyzer itself is already very compact, however, the optimization and simulation have shown that for each of the two ion mirrors, the last electrode does not really contribute to the overall potential distribution in the mirror, hence a reduction of this element could save further space. Extended optimization work in terms of the geometrical shape and arrangement of the mirror electrodes has to be performed to evaluate further possibilities for miniaturization. The variation of the drift tube length while keeping the ion mirrors constant is a simple way to scale the design up to a certain degree, either in positive or negative direction. However, the performance of the spectrometer is heavily dependent on the ion drift length per full-turn and modification of this certainly requires optimization of the mirror potentials.

Extension to other measurement domains

As the MRTOF mass analyzer is an oscillator, the measurement can in principle be extended to the frequency domain. By measuring the image current of the oscillating particles [94] with induction coils or pick-up electrodes integrated into the drift tube, the time-dependent signal can be converted to the frequency domain by fast Fourier transformation (FFT). Each m/z ratio thereby corresponds to a different frequency. As the unambiguous mass range in closed-path MRTOF is decreasing with higher number of performed full-turns, information about the contained m/z over a broad mass range could already be acquired during the particle full-turns in the MR cell, while the TOF signal provides the high-resolution information for specific masses [94]. The fusion of this data could deliver mass spectra with both high unambiguous mass range and high resolution for at least selected m/z.

Another measurable parameter of interest is the ion charge. The integration of two Faraday charge collectors in the drift space could combine the m/z measurement based on MRTOF with the z measurement in a charge detection mass spectrometry (CDMS) instrument [145]. With that, the true masses of the contained ions can be detected. The CDMS is mainly applied to analyze high masses, such as protein complexes [146], and heterogeneous samples [147].

Integration to nano-analytic platforms

As described at the beginning, powerful and compact mass spectrometers are indispensable as add-on instruments for nano-analytic platforms. TOF mass spectrometers have a duty cycle due to pulsed operation, which is currently a major challenge for use in SIMS. The extracted ions cannot be used during the measurement. In addition, ions with very low concentrations cannot be reliably detected with the short injection pulses, even with multiple measurements. To counter this, the development of injection optics with ion trapping functionality is required for integration as an add-on instrument. The trapping and accumulation of particles, such as with quadrupole ion trap, prior to the pulsed injection into the mass analyzer thus allows a significant increase in the duty cycle and permits the detection of masses with very low concentrations. In combination with the MRTOF mass analyzer, the overall add-on system can offer high sensitivity, ultra-high mass resolving power, fast acquisition mass spectrometry with a very compact size for FIB instruments.

Optimization framework

To further increase the capabilities of the CPOpt optimization framework and its flexibility, future extensions are being considered with regard to the methods that can be used for optimization and modeling. The integration of FEM-based modeling programs such as Lorentz [59] can extend the usability, especially in the field of applications with magnetic fields such as the development of magnetic sector mass analyzers. The integration of surrogate models is also conceivable. These are particularly suitable for recurring optimization applications of existing systems, such as the frequent adaptation of potential settings for given optical setups for measurements with different requirements. In addition, the optimization framework will be extended and evaluated to interact with dedicated hardware instead of a computer-based model to allow fast and automated fine-tuning of the real instrument. In the control software of the MRTOF prototype, initial measures have already been taken to interact with CPOpt. In terms of optimization methods, other innovative methods such as particle swarm optimization [148], Pareto ant colony optimization [149] and artificial bee colony optimization [150] will be tested and compared with each other in terms of performance, applicability and computational efficiency. A GUI may be useful to make the framework more intuitive to use, especially for people with low coding experience.

Notation

Abbreviations

Abbreviation	Meaning
2D	two-dimensional
3D	three-dimensional
ADC	analog-to-digital converter
API	application programming interface
BEM	boundary element method
CAD	computer-aided design
CDMS	charge detection mass spectrometry
COSAC	Cometary Sampling and Composition
CPO	charged particle optics
CPOpt	charged particle optics optimization framework
CSV	comma-separated values
DFMS	Double Focusing Mass Spectrometer
DIO	digital input/ output
DMIM	Delta Moment-Independent Measure
EI	electron impact
EOD	Electron Optical Design
FDM	finite difference method
FEM	finite element method
FFT	fast Fourier transformation
FHVS	fast high voltage switch

Abbreviation	Meaning
FIB	focused ion beam
FW50	full width for 50 %
FWHM	full width at half maximum
GA	genetic algorithm
GCMS	Gas Chromatograph and Mass Spectrometer
GEM	geometry
GUI	graphical user interface
HIM	helium ion microscope
INMS	Ion and Neutral Mass Spectrometer
IOB	ion optics workbench
LHS	Latin hypercube sampling
LMAIS	Liquid Metal Alloy Ion Source
MALDI	matrix-assisted laser desorption/ ionization
MCP	microchannel plate
MOGA	multi-objective genetic algorithm
MR	multiple-reflection
MRTOF	multiple-reflection time-of-flight
NSGA-II	non-dominated sorting genetic algorithms II
PA	potential array
PCIe	peripheral component interconnect express
PCP	parallel coordinate plot
PEEK	polyether ether ketone
ROI	region of interest
ROSINA	Rosetta Orbiter Spectrometer for Ion and Neutral Analysis
SEM	scanning electron microscope
SIMS	secondary ion mass spectrometry
SNR	signal-to-noise ratio
STIM	scanning transmission ion microscope
STL	stereolithography
TDC	time-to-digital converter
TEM	transmission electron microscope
TFS	time focus shift
TOB	time-of-birth
TOF	time-of-flight

Bibliography

[1] J. H. Gross, *Mass Spectrometry - A Textbook*. Springer, 2011.

[2] R. Ekman, J. Silberring, A. M. Wenman-Brinkmalm, and A. Kraj, *Mass Spectrometry: Intrumentation, Interpretation, and Applications* (Whiley - Interscience Series in Mass Spectrometry). 2008.

[3] O. De Castro *et al.*, "npSCOPE: A New Multimodal Instrument for In Situ Correlative Analysis of Nanoparticles", *Analytical Chemistry*, vol. 93, pp. 14 417–14 424, 43 2021.

[4] J.-N. Audinot, P. Philipp, O. De Castro, A. Biesemeier, Q. H. Hoang, and T. Wirtz, "Highest resolution chemical imaging based on secondary ion mass spectrometry performed on the helium ion microscope", *Reports on Progress in Physics*, vol. 84, no. 10, p. 105 901, 2021.

[5] O. De Castro *et al.*, "Magnetic Sector Secondary Ion Mass Spectrometry on FIB-SEM Instruments for Nanoscale Chemical Imaging", *Analytical Chemistry*, vol. 94, pp. 10 754–10 763, 30 2022.

[6] R. Arevalo, Z. Ni, and R. M. Danell, "Mass spectrometry and planetary exploration: A brief review and future projection", *Journal of Mass Spectrometry*, vol. 55, no. 1, 2019.

[7] F. Goesmann *et al.*, "COSAC, The Cometary Sampling and Composition Experiment on Philae", *Space Science Reviews*, vol. 128, pp. 257–280, 2006.

[8] H. Balsiger *et al.*, "ROSINA - Rosetta Orbiter Spectrometer for Ion and Neutral Analysis", *Space Science Reviews*, vol. 128, no. 1-4, pp. 1527–1535, 2007.

[9] J. H. Waite *et al.*, "The cassini ion and neutral mass spectrometer (INMS) investigation", in *The Cassini-Huygens Mission*. Springer Netherlands, 2004, pp. 113–231.

[10] A. Benninghoven, F. G. Rudenauer, and H. W. Werner, *Secondary ion mass spectrometry: basic concepts, instrumental aspects, applications and trends*. Wiley-Interscience, 1987.

[11] B. G. Svensson, M. K. Linnarsson, B. Mohadjeri, M. Petravić, and J. Williams, "SIMS and depth profiling of semiconductor structures", *Nuclear Instruments and Methods in Physics Research B*, vol. 85, pp. 363–369, 1-4 1994.

[12] L. Cressa *et al.*, "Toward operando structural, chemical, and electrochemical analyses of solid-state batteries using correlative secondary ion mass spectrometry imaging", *Analytical Chemistry*, vol. 95, pp. 9932–9939, 26 2023.

[13] A. Biesemeier *et al.*, "Correlative Electron Microscopy, High Resolution Ion Imaging and Secondary Ion Mass Spectrometry for High Resolution Nanoanalytics on Biological Tissue", *Microscopy and Microanalysis*, vol. 26, pp. 818–820, 2020.

[14] G. Hlawacek, V. Veligura, R. van Gastel, and B. Poelsema, "Helium ion microscopy", *Journal of Vacuum Science and Technology B*, vol. 32, 2 2014.

[15] T. Wirtz, O. De Castro, J.-N. Audinot, and P. Philipp, "Imaging and analytics on the helium ion microscope", *Annual Review of Analytical Chemistry*, vol. 12, 2019.

[16] zeroK NanoTech. "SIMS:ZERO High-Resolution Cs+ Dynamic SIMS". [Online]. Available: `https://www.zerok.com/products.html#SIMSZERO_GOTO`.

[17] RAITH. "IONMASTER: SIMS nanoanalytics and ion imaging". [Online]. Available: `https://raith.com/products/ionmaster/`.

[18] L. Pillatsch, F. Östlund, and J. Michler, "FIBSIMS: A review of secondary ion mass spectrometry for analytical dual beam focussed ion beam instruments", *Progress in Crystal Growth and Characterization of Materials*, vol. 65, pp. 1–19, 1 2019.

[19] J. H. J. Dawson and M. Guilhaus, "Orthogonal-acceleration time-of-flight mass spectrometer", *Rapid Communications in Mass Spectrometry*, vol. 3, pp. 155–159, 5 1989.

[20] TOFWERK. "An Introduction to FIB-SIMS Using the fibTOF". [Online]. Available: `https://www.tofwerk.com/introduction-fib-sims-using-fibtof/`.

[21] J. A. Whitby *et al.*, "High Spatial Resolution Time-of-Flight Secondary Ion Mass Spectrometry for the Masses: A Novel Orthogonal ToF FIB-SIMS Instrument with In Situ AFM", *Advances in Materials Science and Engineering*, vol. 2012, 1 2011.

[22] K. Li, J. Liu, C. R. M. Grovenor, and K. L. Moore, "NanoSIMS Imaging and Analysis in Materials Science", *Annual Review of Analytical Chemistry*, vol. 13, pp. 273–292, 2020.

[23] J. Nuñez, R. Renslow, J. B. Cliff, and C. R. Anderton, "NanoSIMS for Biological Applications: Current Practices and Analyses", *Biointerphases*, vol. 13, 3 2017.

[24] J.-L. Guerquin-Kern, T.-D. Wu, C. Quintana, and A. Croisy, "Progress in analytical imaging of the cell by dynamic secondary ion mass spectrometry (SIMS microscopy)", *Biochimica et Biophysica Acta (BBA) - General Subjects*, vol. 1724, 3 2005.

[25] J.-N. Audinot, Guignard, H.-N. Migeon, and L. Hoffmann, "Study of the mechanism of diatom cell division by means of 29Si isotope tracing", *Applied Surface Science*, vol. 252, 19 2006.

[26] T. G. Freya and C. A. Mannella, "The internal structure of mitochondria", *Trends in Biochemical Sciences*, vol. 25, pp. 319–324, 7 2000.

[27] R. Sheldon, "Space Applications", in *Mass Spectrometry: Intrumentation, Interpretation, and Applications*. 2008.

[28] H. B. Niemann *et al.*, "The gas chromatograph mass spectrometer for the huygens probe", in *The Cassini-Huygens Mission*. Springer Netherlands, 2003, pp. 553–591.

[29] R. Fausch, P. Wurz, M. Tulej, and U. Rohner, "CubeSatTOF: Planetary Atmospheres Analyzed with a 1U High-Performance Time-Of-Flight Mass Spectrometer", *34th Annual Small Satellite Conference. Proceedings. Virtual Conference*, 2020.

[30] P. D. Spudis *et al.*, "Evidence for water ice on the Moon: Results for anomalous polar craters from the LRO Mini-RF imaging radar", *JGR Planets*, vol. 118, 10 2013.

[31] S. Li *et al.*, "Direct evidence of surface exposed water ice in the lunar polar regions", *Proceedings of the National Academy of Sciences*, vol. 115, 36 2018.

[32] C. I. Honniball *et al.*, "Molecular water detected on the sunlit Moon by SOFIA", *Nature Astronomy*, vol. 5, pp. 121–127, 2021.

[33] I. A. Crawford *et al.*, "Lunar Resources", *Reviews in Mineralogy and Geochemistry*, vol. 89, no. 1, pp. 829–868, 2023.

[34] L. Pfister *et al.*, "Bedrock geology controls on catchment storage, mixing, andrelease: A comparative analysis of 16 nested catchments", *Hydrological Processes*, vol. 31, 10 2017.

[35] J. P. Greenwood, S. Itoh, N. Sakamoto, P. Warren, L. Taylor, and H. Yurimoto, "Hydrogen isotope ratios in lunar rocks indicate delivery of cometary water to the Moon", *Nature Geoscience*, vol. 4, pp. 79–82, 2011.

[36] F. M. McCubbin and J. J. Barnes, "Origin and abundances of H2O in the terrestrial planets, Moon, and asteroids", *Earth and Planetary Science Letters*, vol. 526, no. 115771, 2019.

[37] H. F. Levison, A. Morbidelli, C. V. Laerhoven, R. Gomes, and K. Tsiganis, "Origin of the structure of the Kuiper belt during a dynamical instability in the orbits of Uranus and Neptune", *Icarus*, vol. 196, 1 2008.

[38] J. Oró, "Comets and the Formation of Biochemical Compounds on the Primitive Earth", *Nature*, vol. 190, pp. 389–390, 1961.

[39] J.-P. Lebreton, A. Coustenis, J. Lunine, F. Raulin, T. Owen, and D. Strobel, "Results from the Huygens probe on Titan", *The Astronomy and Astrophysics Review*, vol. 17, pp. 149–179, 2009.

[40] J. Mattauch and R. Herzog, "Über einen neuen Massenspektrographen", *Zeitschrift für Physik*, vol. 89, no. 447, 1934.

[41] E. R. Badman and R. G. Cooks, "Miniature mass analyzers", *Journal of Mass Spectrometry*, vol. 35, no. 6, pp. 659–671, 2000.

[42] A. J. Dempster, "A new method of positive ray analysis", *Physical Review*, vol. 11, 4 1918.

[43] R. Pureti, T. Wirtz, and H. Q. Hoang, "Scanning-assisted focal plane-detection system for a sector-field mass spectrometer - Part-I: Simulation and data processing", *Nuclear Instruments and Methods in Physics Research A*, vol. 1065, no. 169535, 2024.

[44] D. T. Snyder, C. J. Pulliam, Z. Ouyang, and R. G. Cooks, "Miniature and fieldable mass spectrometers: Recent advances", *Analytical Chemistry*, vol. 88, no. 1, pp. 2–29, 2015.

[45] A. Makarov, "Electrostatic axially harmonic orbital trapping: A high-performance technique of mass analysis", *Analytical Chemistry*, vol. 72, no. 6, pp. 1156–1162, 2000.

[46] S. Eliuk and A. Makarov, "Evolution of Orbitrap mass spectrometry instrumenation", *Annual Review of Analytical Chemistry*, vol. 8, pp. 61–80, 2015.

[47] R. A. Scheltema *et al.*, "The q exactive hf, a benchtop mass spectrometer with a pre-filter, high-performance quadrupole and an ultra-high-field orbitrap analyzer", *Molecular and Cellular Proteomics*, vol. 13, no. 12, pp. 3698–3708, 2014.

[48] F. Meier *et al.*, "Parallel Accumulation-Serial Fragmentation (PASEF): Multiplying Sequencing Speed and Sensitivity by Synchronized Scans in a Trapped Ion Mobility Device", *Journal of Proteome Research*, vol. 14, no. 12, pp. 5378–5387, 2015.

[49] R. A. Zubarev and A. Makarov, "Orbitrap mass spectrometry", *Analytical Chemistry*, vol. 85, no. 11, pp. 5288–5296, 2013.

[50] W. Stephens, "A pulsed mass spectrometer with time dispersion", *Physical Reviews*, vol. 69, p. 691, 1946.

[51] A. E. Cameron and D. F. Eggers, "An ion "velocitron"", *Review of Scientific Instruments*, vol. 19, no. 9, 1948.

[52] W. C. Wiley and I. H. McLaren, "Time-of-flight mass spectrometer with improved resolution", *Review of Scientific Instruments*, vol. 26, no. 12, pp. 1150–1157, 1955.

[53] B. A. Mamyrin, V. I. Karataev, D. V. Shmikk, and V. A. Zagulin, "The mass-reflectron, a new nonmagnetic time-of-flight mass spectrometer with high resolution", *Zh. Eksp. Teor. Fiz*, vol. 64, no. 1, pp. 82–89, 1973.

[54] R. Grix, R. Kutscher, G. Li, U. Grüner, H. Wollnik, and H. Matsuda, "A time-of-flight mass analyzer with high resolving power", *Rapid Communications in Mass Spectrometry*, vol. 2, no. 5, pp. 83–85, 1988.

[55] W. R. Plaß, T. Dickel, and C. Scheidenberger, "Multiple-reflection time-of-flight mass spectrometry", *International Journal of Mass Spectrometry*, vol. 349-350, pp. 134–144, 2013.

[56] W. R. Plaß *et al.*, "Isobar separation by time-of-flight mass spectrometry for low-energy radioactive ion beam facilities", *Nuclear Instruments and Methods in Physics Research B*, vol. 266, pp. 4560–4564, 19-20 2008.

[57] M. Rosenbusch *et al.*, "The new MRTOF mass spectrograph following the ZeroDegree spectrometer at RIKEN's RIBF facility", *Nuclear Instruments and Methods in Physics Research A*, vol. 1047, no. 167824, 2023.

[58] COMSOL AB, *COMSOL Multiphysics v. 6.2*, 2023.

[59] Integrated Engineering Software, *LORENTZ 3EM*, 2017.

[60] D. A. Dahl, "SIMION for the personal computer in reflection", *International Journal of Mass Spectrometry*, vol. 200, no. 1-3, pp. 3–25, 2000.

[61] J. Zlámal and B. Lencová, "Development of the program EOD for design in electron and ion microscopy", *Nuclear Instruments and MEthods in Physics Research B*, vol. 645, pp. 278–282, 1 2011.

[62] Los Alamos National Laboratory, *Poisson Superfish v.7.19.2*, 2019.

[63] Lawrence Berkeley National Laboratory, *WARP*, 2000.

[64] J. A. Nelder and R. Mead, "A simplex method for function minimization", *The Computer Journal*, vol. 7, no. 4, pp. 308–313, 1965.

[65] K. Murray *et al.*, "Design of a multiple-reflection time-of-flight mass spectrometer for barium-tagging", *Hyperfine Interactions*, vol. 240, no. 97, pp. 1–9, 2019.

[66] D. M. Olsson and L. S. Nelson, "The nelder-mead simplex procedure for function minimization", *Technometrics*, vol. 17, no. 1, pp. 45–51, 1975.

[67] L. T. Neustock, P. C. Hansen, Z. E. Russell, and L. Hesselink, "Inverse design tool for ion optical devices using the adjoint variable method", *Scientific Reports*, vol. 9, no. 1, 2019.

[68] R. M. Errico, "What is an adjoint model?", *Bulletin of the American Meteorological Society*, vol. 78, no. 11, pp. 2577–2592, 1997.

[69] J. H. Holland, "Genetic algorithms", *Scientific American*, vol. 267, no. 1, pp. 66–73, 1992.

[70] T. Murata and H. Ishibuchi, "Moga: Multi-objective genetic algorithms", in *IEEE International Conference On Evolutionary Computation*, IEEE Piscataway, vol. 1, 1995, pp. 289–294.

[71] J. Wan, P. Chu, Y. Jiao, and Y. Li, "Improvement of machine learning enhanced genetic algorithm for nonlinear beam dynamics optimization", *Nuclear Instruments and Methods in Physics Research A*, vol. 946, p. 162 683, 2019.

[72] D. Dowsett, "Advanced SIMION techniques: Boundary matching and genetic optimization", *Microscopy and Microanalysis*, vol. 21, no. S4, pp. 218–223, 2015.

[73] A. V. Karpov, A. A. Sysoev, S. S. Poteshin, D. M. Chernyshev, and A. A. Sysoev, "Genetic algorithm for voltage optimization of gridless ion mirror", *Physics Procedia*, vol. 72, pp. 236–240, 2015.

[74] N. H. M. Nezhad, M. G. Niasar, A. M. Gheidari, C. W. Hagen, and P. Kruit, "Multi-electrode lens optimization using genetic algorithms", *International Journal of Modern Physics A*, vol. 34, no. 36, p. 1 942 020, 2019.

[75] T. Dickel *et al.*, "A high-performance multiple-reflection time-of-flight mass spectrometer and isobar separator for the research with exotic nuclei", *Nuclear Instruments and Methods in Physics Research A*, vol. 777, pp. 172–188, 2015.

[76] F. Karami and A. B. Dariane, "A review and evaluation of multi and many-objective optimization: Methods and algorithms", *Global Journal of Ecology*, vol. 7, no. 2, pp. 104–119, 2022.

[77] S. B. Selçuklu, "Multi-objective Genetic Algorithms", in *Handbook of Formal Optimization*. Springer, 2023.

[78] N. H. M. Nezhad, M. G. Niasar, A. M. Gheidari, P. Kruit, and C. W. Hagen, "Multiple criteria optimization of electrostatic electron lenses using multiobjective genetic algorithms", *Journal of Vacuum Science & Technology B*, vol. 39, no. 6, p. 062 605, 2021.

[79] F. Xian, C. L. Hendrickson, and A. G. Marshall, "High resolution mass spectrometry", *Analytical Chemistry*, vol. 84, no. 2, pp. 708–719, 2012.

[80] A. G. Brenton and A. R. Godfrey, "Accurate mass measurement: Terminology and treatment of data", *Journal of the American Society for Mass Spectrometry*, vol. 21, pp. 1821–1835, 2010.

[81] M. Guilhaus, "Principles and instrumentation in time-of-flight mass spectrometry", *Journal of Mass Spectrometry*, vol. 30, pp. 1519–1532, 1995.

[82] A. Radionova, I. Filippov, and P. J. Derrick, "In pursuit of resolution in time-of-flight mass spectrometry: A historical perspective", *Mass Spectrometry Reviews*, vol. 35, pp. 738–757, 2016.

[83] B. A. Mamyrin, "Time-of-flight mass spectrometry (concepts, achievements, and prospects)", *International Journal of Mass Spectrometry*, vol. 206, no. 3, pp. 251–266, 2001.

[84] C. Hornung, "High-Resolution Experiments with the Multiple-Reflection Time-of-Flight Mass Spectrometer at the Fragment Separator FRS", Ph.D. dissertation, Justus-Liebig-Universität Gießen, 2018.

[85] U. Boesl, "Time-of-flight mass spectrometry: Introduction to the basics", *Mass Spectrometry Reviews*, vol. 36, pp. 86–109, 2017.

[86] M. Yavor, *Optics of Charged Particle Analyzers* (Advances in Imaging and Electron Physics). Elsevier, 2009, vol. 157, pp. 1–381.

[87] H. Wollnik, *Optics of Charged Particles*, 2nd ed. Academic Press, 2021.

[88] C. Jesch, "The Multiple-Reflection Time-of-Flight Isobar Separator for TITAN and Direct Mass Measurements at the FRS Ion Catcher", Ph.D. dissertation, Justus-Liebig-Universität Gießen, 2016.

[89] R. J. Cotter, "The new time-of-flight mass spectrometry", *Analytical Chemistry News and Features*, vol. 71, no. 13, 445A–451A, 1999.

[90] S. G. Alikanov, "A new impulse technique for ion mass", *Soviet Physics JETP*, vol. 4, p. 452, 1957.

[91] H. Wollnik, "History of mass measurements in time-of-flight mass analyzers", *International Journal of Mass Spectrometry*, vol. 349-350, pp. 38–46, 2013.

[92] W. Poschenrieder, "Multiple-focusing time-of-flight mass spectrometers Part II. TOFMS with equal energy acceleration", *International Journal of Mass Spectrometry and Ion Physics*, vol. 9, pp. 357–373, 4 1972.

[93] D. Okumura, M. Toyoda, M. Ishihara, and I. Katakuse, "A simple multi-turn time-of-flight mass spectrometer 'multum ii'", *Journal of the Mass Spectrometry Society of Japan*, vol. 51, no. 2, pp. 349–353, 2003.

[94] E. T. Dziekonski, J. T. Johnson, K. W. Lee, and S. A. McLuckey, "Fourier-Transform MS and Closed-Path Multireflection Time-of-Flight MS Using an Electrostatic Linear Ion Trap", *Analytical Chemistry*, vol. 89, pp. 10 965–10 972, 20 2017.

[95] R. Frey and E. W. Schlag, "Time of Flight Mass Spectrometer Using an Ion Reflector", Patent US4731532, 1988.

[96] R. Kutscher, R. Grix, G. Li, and H. Wollnik, "A Transversally and Longitudinally Focusing Time-of-Flight Mass Spectrometer", *International Journal of Mass Spectrometry and Ion Processes*, vol. 103, pp. 117–128, 2-3 1991.

[97] H. Wollnik, "Flight Time Mass Spectrometer Has Significantly Greater Ion Energy on Substantially Rotation Symmetrical Electrostatic Accelerating Lens Axis Near Central Electrodes than for Rest of Flight Path", Patent DE10116536, 2002.

[98] A. Casares, A. Kholomeev, and H. Wollnik, "Multipass Time-of-Flight Mass Spectrometers with High Resolving Powers", *International Journal of Mass Spectrometry*, vol. 206, pp. 267–273, 3 2001.

[99] H. Wollnik and A. Casares, "An energy-isochronous multi-pass time-of-flight mass spectrometer consisting of two coaxial electrostatic mirrors", *International Journal of Mass Spectrometry*, vol. 227, no. 2, pp. 217–222, 2003.

[100] M. Karas and F. Hillenkamp, "Laser desorption ionization of proteins with molecular masses exceeding 10000 daltons", *Analytical Chemistry*, vol. 60, no. 2299, 1988.

[101] A. X. Chen, A. J. Antolak, K. N. Leung, D. H. Morse, and T. N. Raber, "Fast Mechanical Shutter for Pulsed Ion Beam Generation", *Nuclear Instruments and Methods in Physics Research A*, vol. 670, pp. 45–48, 2012.

[102] G. E. Yefchak, G. A. Schultz, J. Allison, C. G. Enke, and J. F. Holland, "Beam deflection for temporal encoding in time-of-flight mass spectrometry", *Journal of the American Society for Mass Spectrometry*, vol. 1, no. 6, pp. 440–447, 1990.

[103] R. J. Bosca and D. L. Weathers, "Modeling and optimization of a deflection slit for fast-pulsing a low energy ion beam", *Nuclear instruments and Methods in Physics Research B*, vol. 261, pp. 430–434, 2007.

[104] M. Guilhaus, V. Mlynski, and D. Selby, "Perfect timing: Time-of-flight mass spectrometry", *Rapid Communications in Mass Spectrometry*, vol. 11, pp. 951–962, 1997.

[105] Y. Ito *et al.*, "A novel ion cooling trap for multi-reflection time-of-flight mass spectrograph", *Nuclear Instruments and Methods in Physics Research B*, vol. 317, pp. 544–549, 2013.

[106] R. Grix, U. Grüner, G. Li, H. Stroh, and H. Wollnik, "An electron impact storage ion source for time-of-flight mass spectrometers", *International Journal of Mass Spectrometry and Ion Processes*, vol. 93, no. 3, pp. 323–330, 1989.

[107] J. L. Wiza, "Microchannel plate detectors", *Nuclear Instruments and Methods*, vol. 162, pp. 587–601, 1-3 1979.

[108] Hamamatsu Photonics K. K., *MCP (Microchannel Plate) Assembly*, 2021.

[109] Photonis, *Advanced Performance Detector APD2 APTOF GEN2*, 2017.

[110] Spectrum, *Mass Spectrometry and the Modern Digitizer*, 2023.

[111] X.-S. Yang and S. Koziel, "Computational Optimization: An Overview", in *Computational Optimization, Methods and Algorithms*. Springer, 2011.

[112] G. B. Dantzig, *Linear Programming and Extension*. Princeton University Press, 1963.

[113] S. Kirkpatrick, C. D. Gelatt, and M. P. Vecchi, "Optimization by simulated annealing", *Science*, vol. 220, no. 4598, pp. 671–680, 1983.

[114] A. E. Eiben and J. E. Smith, "Evolutionary Computing: The Origins", in *Introduction to Evolutionary Computing*. Springer, 2015.

[115] S. Koziel, D. E. Ciaurri, and L. Leifsson, "Surrogate-Based Methods", in *Computational Optimization, Methods and Algorithms*. Springer, 2011.

[116] K. Huber, T. Wirtz, and H. Q. Hoang, "CPOpt: A modular framework for genetic algorithm optimization and post-optimization analysis in complex charged particle optical design", *Nuclear Instruments and Methods in Physics Research A*, vol. 1067, no. 169702, 2024.

[117] S. Katoch, S. S. Chauhan, and V. Kumar, "A review on genetic algorithm: past, present, and future", *Multimedia Tools and Applications*, vol. 80, pp. 8091–8126, 2020.

[118] K. Deb, "Multi-objective Optimisation Using Evolutionary Algorithms: An Introduction", in *Multi-objective Evolutionary Optimisation for Product Design and Manufacturing*. Springer, 2011.

[119] E. Wirsansky, *Hands-On Genetic Algorithms with Python*. Packt Publishing, 2020.

[120] A. Shukla, H. M. Pandey, and D. Mehrotra, "Comparative Review of Selection Techniques in Genetic Algorithm", in *2015 International Conference on Futuristic Trends on Computational Analysis and Knowledge Management*, 2015.

[121] K. Deb, A. Pratap, S. Agarwal, and T. Meyarivan, "A Fast and Elitist Multiobjective Genetic Algorithm: NSGA-II", *IEEE Transactions on Evolutionary Computation*, vol. 6, pp. 182–197, 2002.

[122] A. E. Eiben and J. E. Smith, "Representation, Mutation, and Recombination", in *Introduction to Evolutionary Computing*. Springer, 2015.

[123] K. Deb and R. B. Agrawal, "Simulated binary crossover for continuous search space", *Complex Systems*, vol. 9, no. 2, pp. 115–148, 1995.

[124] D. Manura and D. Dahl, *SIMION (R) 8.x User Manual*, Adaptas Solutions LLC, Palmer, MA, 2008.

[125] D. Cubric, B. Lencova, F. H. Read, and J. Zlamal, "Comparison of FDM, FEM and BEM for electrostatic charged particle optics", *Nuclear Instruments and Methods in Physics Research A*, vol. 427, pp. 357–362, 1-2 1999.

[126] S. Smith, M. Southerby, S. Setiniyaz, R. Apsimon, and G. Burt, "Multiobjective optimization and pareto front visualization techniques applied to normal conducting rf accelerating structures", *Physical Review Accelerators and Beams*, vol. 25, no. 6, 2022.

[127] F.-A. Fortin, F.-M. D. Rainville, M.-A. Gardner, M. Parizeau, and C. Gagné, "DEAP: Evolutionary algorithms made easy, A python framework for evolutionary algorithms", *Journal of Machine Learning Research*, vol. 13, pp. 2171–2175, 2012.

[128] P. Hintjens, *ZeroMQ: Messaging for Many Applications*. O'Reilly, 2013.

[129] A. Saltelli *et al.*, *Global Sensitivity Analysis. The Primer*. John Wiley & Sons, 2008.

[130] E. Borgonova, "A new uncertainty importance measure", *Reliability Engineering & System Safety*, 2006.

[131] E. Plischke, E. Borgonova, and C. L. Smith, "Global sensitivity measures from given data", *European Journal of Operational Research*, vol. 226, no. 3, pp. 536–550, 2013.

[132] F. A. C. Viana, "A tutorial on latin hypercube design of experiments", *Quality and Reliability Engineering International*, vol. 32, no. 5, pp. 1975–1985, 2015.

[133] F. Pedregosa *et al.*, "Scikit-learn: Machine learning in python", *Journal of Machine Learning Research*, vol. 12, pp. 2825–2830, 2011.

[134] P. M. Reed *et al.*, *Addressing Uncertainty in Multisector Dynamics Research*. Zenodo, 2022.

[135] J. Herman and W. Usher, "Salib: An open-source python library for sensitivity analysis", *The Journal of Open Source Software*, vol. 2, no. 9, p. 97, 2017.

[136] T. Dickel *et al.*, "Dynamical time focus shift in multiple-reflection time-of-flight mass spectrometers", *International Journal of Mass Spectrometry*, vol. 412, pp. 1–7, 2017.

[137] M. I. Yavor, T. V. Pomozov, S. N. Kirillov, Y. I. Khasin, and A. N. Verenchikov, "High performance gridless ion mirrors for multi-reflection time-of-flight and electrostatic trap mass analyzers", *International Journal of Mass Spectrometry*, vol. 426, pp. 1–11, 2018.

[138] D. Abplanalp, P. Wurz, L. Huber, and I. Leya, "An optimised compact electron impact ion storage source for a time-of-flight mass spectrometer", *International Journal of Mass Spectrometry*, vol. 294, pp. 33–39, 2010.

[139] J. Ximen, Z. Xu, Z. Liu, and H. Wollnik, "Design and calculation of an electron impact storage ion source for time-of-flight mass spectrometers", *International Journal of Mass Spectrometry and Ion Processes*, vol. 161, pp. 91–96, 1997.

[140] A. O. Nier, "A mass spectrometer for isotope and gas analysis", *The Review of Scientific Instruments*, vol. 18, no. 6, pp. 398–411, 1947.

[141] C. J. Park and J. R. Ahn, "Effect of magnetic field in electron-impact ion sources and simulation of electron trajectories", *Review of Scientific Instruments*, vol. 77, no. 8, p. 085 107, 2006.

[142] Y. Toker *et al.*, "The kick-out mass selection technique for ions stored in an electrostatic ion beam trap", *Journal of Instrumentation*, vol. 4, no. 9, 2009.

[143] C. P. S. U. The CubeSat Program, *CubeSat Design Specification REV 14.1*, 2022.

[144] R. G. Fausch *et al.*, "Monitoring Space Weather with a Sensitive 1U CubeSat Mass Spectrometer", in *IEEE Aerospace Conference*, 2023.

[145] J. Hoyes and G. Wray, "Teaching an old geometry new tricks: Poschenrieder for Charge Detection Mass Spectrometry (CDMS)", in *69th ASMS Conference on Mass Spectrometry and Allied Topics*, 2021.

[146] N. C. Contino, E. E. Pierson, D. Z. Keifer, and M. F. Jarrold, "Charge Detection Mass Spectrometry with ResolvedCharge States", *Journal of the American Society for Mass Spectrometry*, vol. 24, pp. 101–108, 2012.

[147] D. Z. Keifer, E. E. Pierson, and M. F. Jarrold, "Charge Detection Mass Spectrometry: Weighing Heavier Things", *Analyst*, vol. 142, no. 1654, 2017.

[148] R. Eberhart and J. Kennedy, "A new optimizer using particle swarm theory", in *Proceeding of the Sixth International Symposium on Micro Machine and Human Science*, 1995.

[149] K. Doerner, W. J. Gutjahr, R. F. Hartl, C. Strauss, and C. Stummer, "Pareto Ant Colony Optimization: A Metaheuristic Approach to Multiobjective Portfolio Selection", *Annals of Operations Research*, vol. 131, pp. 79–99, 2004.

[150] D. Karaboga and B. Basturk, "A powerful and efficient algorithm for numerical function optimization: Artificial bee colony (abc) algorithm", *Journal of Global Optimization*, vol. 39, pp. 459–471, 2007.

Acknowledgments

I would like to express my deep gratitude to a number of people who supported me during my doctorate and who made a significant contribution to this project.

First of all, I would like to sincerely thank my supervisors Dr. Tom Wirtz and Dr. Hung Quang Hoang, who accompanied me from the beginning to the end of my doctorate. You have not only given me the opportunity to conduct research in a very exciting project, but have also always supported me in looking left and right and exploring new directions. I highly value your professional and personal advice.

I would also like to thank the co-examiners of this thesis Prof. Dr. Jorge Iñiguez, Prof. Dr. Pieter Kruit and Prof. Dr. Anjam Khursheed for their commitment.

My thanks also go to Dr. Jan Thoemel, who has accompanied this project with great commitment as a member of the doctoral supervision committee and kindly introduced me to the space ecosystem in Luxembourg.

This work would undoubtedly be very theoretical without the time and expertise of two colleagues, Olivier Bouton and Rachid Barrahma, who contributed significantly to the development and assembly of the prototype. I would like to thank you warmly for your dedication and for your input.

I would like to thank all my colleagues from the Avanced Instrumentation for Nano-Analytics (AINA) group for the always pleasant and collegial atmosphere in my daily working life and some very valuable discussions. Special thanks goes to Olivier De Castro, Luca Cressa, Rathaiah Pureti, Dustin Andersen and Tatjana Taubitz.

Finally, I would like to thank all my good friends and my family who have always stood behind me outside of work. In particular, I would like to thank my parents, who have supported me relentlessly over the years. My biggest thanks ultimately go to my wife and my son, who have supported, understood and built me up on a daily basis. Without both of you, none of this would have been possible.

List of Publications

Journal publications

[1] R. Albers et al., "Magnetospheric Venus Space Explorers (MVSE) mission: A proposal for understanding the dynamics of induced magnetospheres", *Acta Astronautica*, vol. 221, pp. 194-205, 2024.

[2] K. Huber, T. Wirtz, H. Q. Hoang, "CPOpt: A modular framework for genetic algorithm optimization and post-optimization analysis in complex charged particle optical design", *Nuclear Instruments and Methods in Physics Research Section A*, vol. 1067, no. 169702, 2024.

[3] K. Huber, T. Wirtz, H. Q. Hoang, "An optimized pulsed ion extraction method for the electron impact storage ion source in multiple-reflection time-of-flight mass spectrometry", to be submitted.

Conference publications

[1] K. Huber, "Development of a multiple-reflection time-of-flight mass spectrometer for space applications", *DPPM PhD Day and General Assembly*, 2022. (Poster presentation)

[2] K. Huber, T. Wirtz, H. Q. Hoang, "Optimization framework for charged particle optics modeling using genetic algorithms and incorporated sensitivity analysis", *20th International Microscopy Congress*, 2023. (Oral presentation)

[3] K. Huber, T. Wirtz, H. Q. Hoang, "Towards automated development of charged particle optical instrumentation using a novel optimization framework", *72nd*

ASMS Conference on Mass Spectrometry and Allied Topics, 2024. (Poster presentation)

[4] K. Huber, "Genetic algorithm optimization and post-optimization data analysis for charged particle optics simulation with SIMION", *Fit4Nano Workshop on Focused Ion Beam Charged Particle Optics and Instrumentation*, 2024. (Invited oral presentation)

Patent

[1] K. Huber, H. Q. Hoang, "Electron impact ion source", Patent (requested) EP24206400, 2024.